44

Robotic Retinal Surgery

Emmanuel Vander Poorten[1], Cameron N. Riviere[2], Jake J. Abbott[3], Christos Bergeles[4], M. Ali Nasseri[5], Jin U. Kang[6], Raphael Sznitman[7], Koorosh Faridpooya[8], and Iulian Iordachita[9]

[1]*Department of Mechanical Engineering, KU Leuven, Heverlee, Vlaams-Brabant, Belgium,* [2]*Robotics Institute, Carnegie Mellon University, Pittsburgh, PA, United States,* [3]*Department of Mechanical Engineering, University of Utah, Salt Lake City, UT, United States,* [4]*School of Biomedical Engineering and Imaging Sciences, King's College London, London, Greater London Area, United Kingdom,* [5]*Department of Ophthalmology, Technische Universität München, München, Bayern, Germany,* [6]*Department of Electrical and Computer Engineering, Johns Hopkins University, Baltimore, MD, United States,* [7]*ARTORG Center for Biomedical Engineering Research, University of Bern, Bern, Canton of Bern, Switzerland,* [8]*Vitreoretinal Department, Eye Hospital Rotterdam, Rotterdam, Zuid-Holland, The Netherlands,* [9]*Department of Mechanical Engineering, Johns Hopkins University, Baltimore, MD, United States*

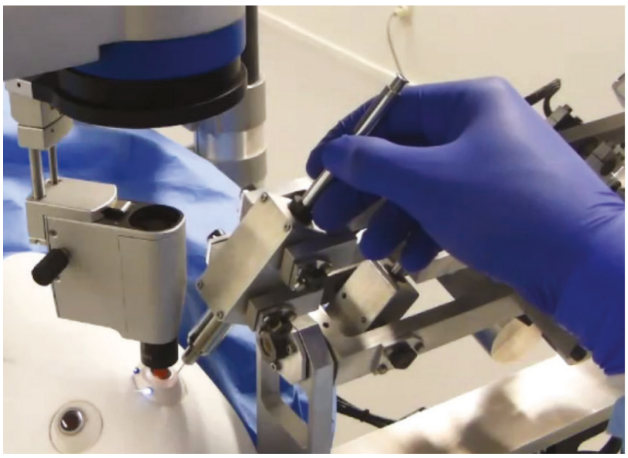

CHAPTER FOCUS
ENGINEERING & CLINICAL

TECHNOLOGY
ROBOTIC & IMAGE-GUIDED

LINK TO VIDEO

ABSTRACT

Retinal surgery has long drawn the attention of engineers and clinicians who recognized a clear use case for robotics and assistive technology in this discipline where precision is paramount. Skilled practitioners operate on the boundaries of human capability, dealing with minuscule anatomic structures that are both fragile and hard to discern. Surgical operations on the retina, a hair-thick multilayered structure that is an integral part of the central nervous system and that is responsible for our vision, spurred the development of robotic system that enhance perception, precision, and dexterity. This book chapter provides an encompassing overview of the progress that has been made during the last three decades in terms of sensing, modeling, visualization, stabilization, and control in the field of robotic retinal surgery. The chapter reports on recent breakthroughs with first-in-human experiences, as well as on new venues that hold the potential to expand retinal surgery to techniques that would be infeasible or very challenging without robotics.

Handbook of Robotic and Image-Guided Surgery. DOI: https://doi.org/10.1016/B978-0-443-13912-3.00011-7

44.1 The clinical need

The retina is a "layer of nervous tissue that covers the inside of the back two-thirds of the eyeball, in which stimulation by light occurs, initiating the sensation of vision" and "is actually an extension of the brain, formed embryonically from neural tissue and connected to the brain proper by the optic nerve" [1]. Any damage to the retina may cause irreversible and permanent visual field defect or even blindness. Key structures that are the subject of different surgical interventions are depicted in Fig. 44.1. They include the sclera, retinal vessels, scar tissue or epiretinal membranes and, recently, the retinal layers. A list of parameters and dimensions that characterize these structures is provided in Table 44.1. Relevant structures range from several hundred microns down to 0.5 μm. In comparison, we note that the diameter of the average human hair is 50 μm, which highlights the micromanipulation challenges that are present in retinal surgery.

Open surgery is a less-than-desirable option when treating critically fragile structures within the eye, such as the retina. Surgeons approach the retina through a "keyhole" setup, inserting slender instruments through small incisions in the sclera to operate at a micrometer scale on structures whose complexity rivals or exceeds that of the brain. Visualization traditionally occurs through a stereo-operating microscope. The incision forms a fulcrum point. This fulcrum complicates hand–eye coordination due to the inverted relationship between hand and instrument motion (Fig. 44.2). If the instrument is not pivoted exactly about the fulcrum point, a net force will be applied to the sclera which could damage the sclera or could potentially cause the eye to rotate in its socket. When the eye rotates, it becomes more difficult to reach a location on the retina precisely as the target location changes dynamically. The surgeon uses the support of an armrest and the patient's head to stabilize the hands. Lightweight instruments are maneuvered within the confined space between the patient's head and the microscope. A wide-angle lens is often placed between the eye and microscope offering a larger view of the retina. It does limit the work volume that is available.

In recent years, digital microscopes have made their entrance in the operating room. Thanks to digital camera's integration in the stereo-microscope and recent improvements in 3D display technology, micro-surgeons are no longer obliged to observe the eye's internals through the stereo-microscope's binoculars. Instead, the stereo-images are being rendered on a stereo-display that is positioned at the level of the patient's feet. Fig. 44.3 provides an overview of this more recent layout. With hybrid systems, surgeons can choose and switch between imaging modalities depending on their preference or anatomic structure that is targeted.

44.1.1 Human factors and technical challenges

Retinal microsurgery demands advanced surgical skills. The requirements for vision, depth perception, and fine motor control are high (Table 44.2), exceeding the fundamental physiological capability of many individuals [27–29].

A primary cause of tool positioning error is physiological tremor [30]. Even when microsurgical procedures are successfully performed, in the presence of tremor they require greater concentration and effort and are attended by greater risk. Patient movement is another important confounding factor. Among patients who snore under monitored anesthesia (≈16%), half have sudden head movements during surgery, leading to a higher risk of complications [31]. The challenges of retinal microsurgery are

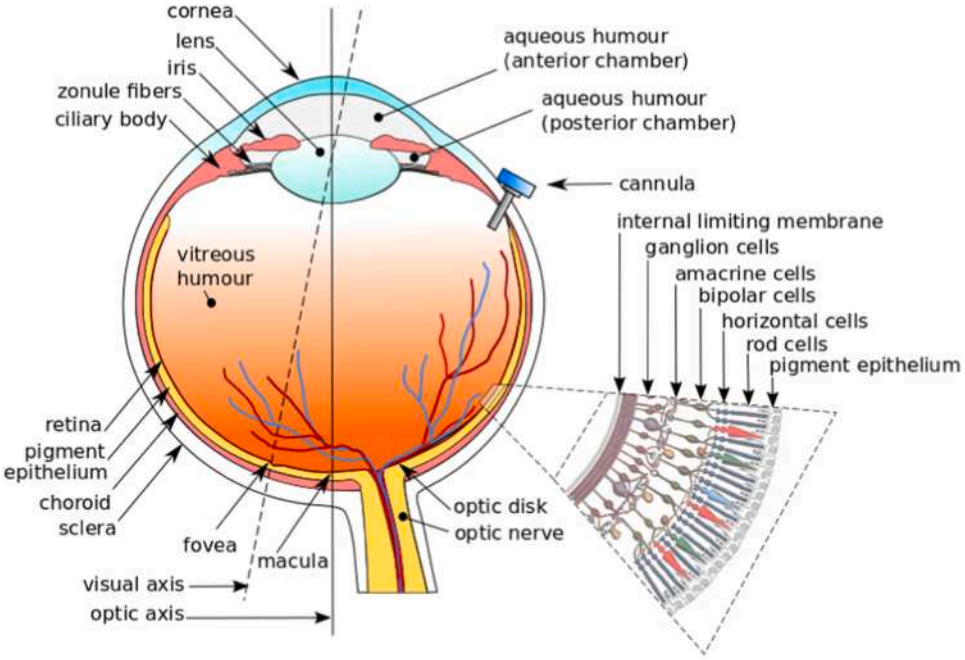

FIGURE 44.1 **A cross-section of a human eye.** A cannula is placed at 4 mm from the cornea limbus (the border of the cornea and the sclera), providing access to the intraocular space.

TABLE 44.1 Governing dimensions in retinal surgery.

Structure	Dimension	Comment/sources
Human eye	24.6 mm avg	Axial length [2]
Internal limiting membrane	0.5–2.5 μm, 1–3 μm	Maximal at macula [3,4]
Epiretinal membrane	60 μm	Cellular preretinal layer [5]
Retinal vessel	40–350 μm, 40–120 μm	Branch to central [6,7]
Human retina (11 layers)	100–300 μm	Thickness [7]
Retina layer 1	26±12 μm	Nerve fiber layer [8]
Retina layer 2	32±14 μm	Ganglion cell layer [8]
Retina layer 3	45±12 μm	Inner plexiform layer [8]
Retina layer 4	28±15 μm	Inner nuclear layer [8]
Retina layer 5	28±13 μm	Outer plexiform layer [8]
Retina layer 6	64±24 μm	Outer nuclear layer and outer limiting membrane [8]
Retina layer 7	24±14 μm	Inner segment layer [8]
Retina layer 8	16±9 μm	Connecting cilia [8]
Retina layer 9	10±3 μm	Outer segment layer [8]
Retina layer 10	11±4 μm	Verhoeff's membrane [8]
Retina layer 11	21±10 μm	Retinal pigment epithelium [8]
Vessel puncture force	20 mN avg, 181 mN max	Cadaver pig eye [9]
	63% <5 mN	Cadaver pig eye [10]
	0.6–17.5 mN; 80% <7 mN	Cadaver pig eye [11]
	2 mN avg, 1 mN std	Fertilized chicken egg [12]
	80% <5 mN	Fertilized chicken egg [13]
Vessel dissection force	67 mN avg, 82 mN max	Cadaver pig eye [9]
Peeling force	8–12 mN, 15–45 mN	Inner shell membrane (ISM) of chicken egg [12,14]
Damage during peeling	From 5.1 mN	Fertilized chicken egg [15]
	From 6.4 mN	Rabbit [15]
Retina damage	1788 Pa	17.2 mN on 3.5 mm diameter [16]
Breathing frequency	3 Hz; 0.2 Hz	Rat [17]; pig [18]
Breathing amplitude	50 μm; 300 μm	Rat [17]; pig [18]
Vascular pulsation frequency	0.84 Hz; 2 Hz	Rat [17]; pig [18]
Vascular pulsation amplitude	15 μm; 100 μm	Rat [17]; pig [18]
Required positioning accuracy	10 μm	General [19,20]
Required positioning accuracy	25 μm	Subretinal injection [21]

further exacerbated by the fact that in the majority of contact events, the forces encountered are below the tactile perception threshold of the surgeon [10]. Inability to detect surgically relevant forces leads to a lack of control over potentially injurious factors that result in complications.

Aside from the poor ergonomics of operating through a surgical microscope, leading to an elevated risk for back and neck injuries, with incidence of 30%–70% for neck pain and 40%–80% for back pain [32], this approach is associated with difficult hand–eye coordination. Without haptic feedback, the surgeon can only rely on visual feedback. However, the quality of the visual

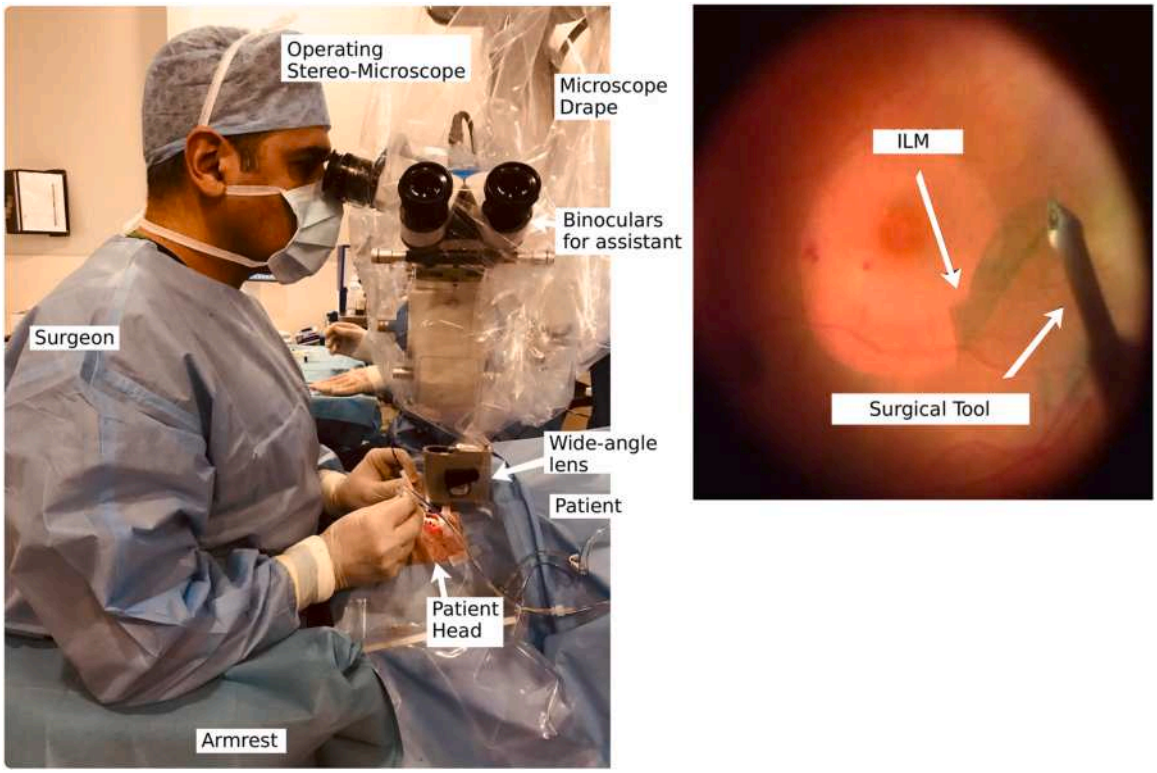

FIGURE 44.2 **Overall layout and view during retinal surgery.** (Left) Retinal surgical scene using surgical microscope. Surgeon holding vitrectome in right hand and light pipe in the left; (right) typical view during an internal limiting layer (ILM) peeling.

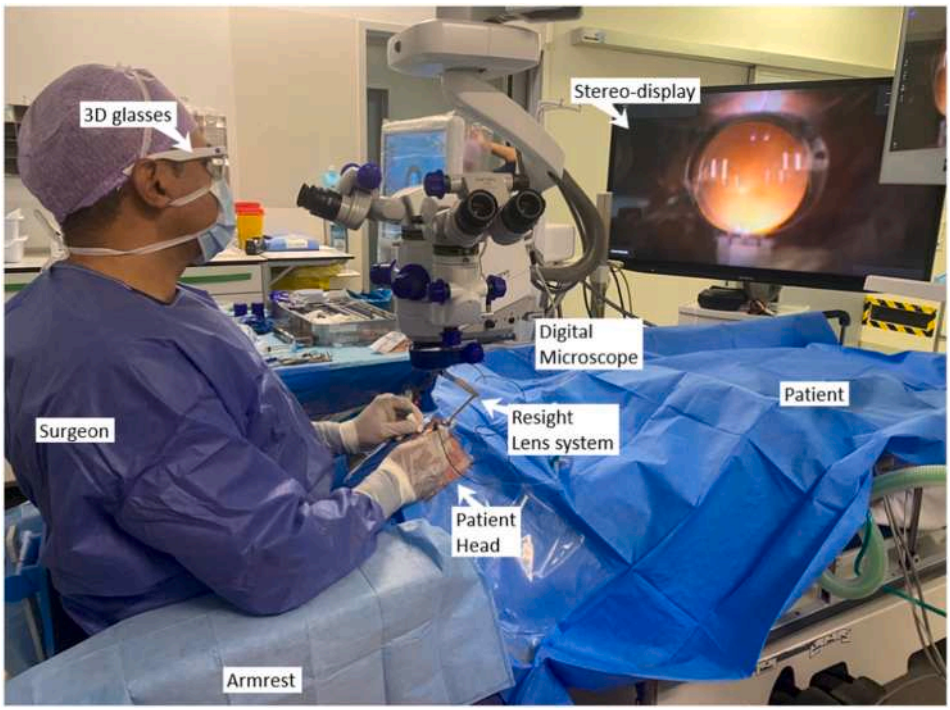

FIGURE 44.3 **Overall layout when using digital microscope and 3D display.** The surgeon observes the vitreoretinal space through dedicated 3D glasses looking beyond the microscope.

TABLE 44.2 Human factors and technical limitations in retinal surgery.

Parameter	Value	Comment/sources
Physiologic tremor	182 μm, 100 μm rms	Epiretinal membrane removal [22,23]
	156 μm rms	Artificial eye model [24]
	8–12 Hz area	Neurogenic tremor component [19]
Fulcrum motion	Up to 12.6 mm^2	During, e.g., manual vitrectomy [25]
Maximum velocity	0.7 m/s	Epiretinal membrane removal [22]
Typical velocity maximum acceleration	0.1–0.5 mm/s 30.1 m/s^2	Epiretinal membrane peeling [26], epiretinal membrane removal [22]
Manipulation forces	<7.5 mN in 75%	Ex vivo pig eye membrane [10]

feedback is still not good enough. Surgeons spend considerable effort adjusting the optics and illumination to obtain the appropriate level of clarity, detail, and overview of the target scene. Depth perception is suboptimal. Even with modern stereo microscopes, such as depicted in Fig. 44.3 that address already some of the ergonomic concerns, surgeons are still sometimes unsure exactly when contact with the retina is established. Poor visualization due to factors such as corneal scars or intense vitreous hemorrhage can affect the outcome of retinal surgeries and increase the chance of complications.

44.1.2 Motivation for robotic technology

Given the size and fragile nature of the structures involved, complication rates are not negligible [33–35]. Surgical steps that are considered too risky or even impossible may be facilitated through robotics. There is also an interest in automating repetitive tasks to reduce cognitive load and allow experts to focus on critical steps of a procedure. Ergonomy represents another area of potential innovation. One can reconsider the operating layout and optimize usability to reduce physical burdens.

Some appealing characteristics of robotic technology for treating the retina include improved positioning accuracy through some combination of motion scaling and tremor reduction, the ability to keep an instrument steady and immobilized for a prolonged period of time, and the ability to save coordinates for future use. The retina is neural tissue; even a small mistake can cause irreversible damage, including blindness. Through robotics, procedures that cannot be performed safely using conventional manual techniques due to limitations in precision, such as microcannulation [6,36,37], procedures that could benefit from additional safety such as membrane peeling [38,39] or where improper placement could significantly impact procedural effectiveness, such as in subretinal injection, could be considered [40–42]. Also, in current manual practice, surgeons can only use two instruments simultaneously, although three or more instruments would be helpful in complicated cases, such as delaminations. Robotics further facilitates integration with advanced tooling. Dedicated interfaces could help manage instruments with articulating end-effectors. User interfaces can be tailored to provide feedback from a broad range of sensors embedded in a new line of "intelligent" instruments. Robotic surgery may enable operation with narrower instruments, which would decrease the size of scleral incisions and reduce damage to the sclera.

Taken in combination, the above characteristics could create a highly effective therapeutic system for performing advanced microsurgical procedures. Not only could the added functionality decrease complication rates, it could also speed up healing and shorten the duration of admission in clinic. For robotics to be successful, the above arguments would need to outweigh the disadvantages of elevated operational cost and increased operation time that seem inevitable, based on today's technology.

44.1.3 Main targeted interventions

The following retinal procedures have received considerable attention from researchers who identified opportunities for improvement by use of robotic technology.

44.1.3.1 Epiretinal membrane peeling

An epiretinal membrane (ERM) is an avascular, fibrocellular membrane, such as a scar tissue, that may form on the inner surface of the retina and cause blurred and distorted central vision. Risk for ERM increases with age, primarily affecting people over age 50. ERM is mostly idiopathic and related to an abnormality of the vitreoretinal interface in conjunction with a posterior vitreous detachment. ERM can also be triggered by certain eye diseases such as a retinal tear, retinal detachment, and inflammation of the eye (uveitis). The prevalence of ERM is 2% in individuals under age 60 and 12% in those over age 70 [43]. Although asymptomatic, ERM often leads to reduced visual acuity and metamorphopsia, where straight lines can appear wavy due to contraction forces acting over the macular region [44]. Treatment is surgical and only when the patient suffers from binocular metamorphopsia and progressive

visual decrease less than 50%. The procedure involves pars plana vitrectomy, followed by removal (peeling) of the ERM, with or without peeling of the native internal limiting membrane (ILM) in order to decrease the recurrence of ERM afterwards [45].

44.1.3.2 Retinal vein cannulation

Retinal vein occlusion is the secondmost prevalent vasculature-related eye disease [46]. A blood clot clogs the vein, which leads to a sudden halt in retinal perfusion. Since arterial inflow continues, hemorrhages develop and the retina may become ischemic, leading to retinal neural cell apoptosis. Depending on the thrombus location, one distinguishes between central retinal vein occlusion (CRVO) and branch retinal vein occlusion (BRVO), that is, when the thrombus resides in a smaller branch vein. BRVO can be assymptomatic but may lead up to sudden painless legal blindness. Secondary macular edema can develop and cause metamorphopsia. Later on, neovascularization can occur because of ischemic retina and cause secondary glaucoma, retinal detachment, and vitreous hemorrhage [47]. There is no etiologic curative treatment at present. One of the few symptomatic treatments that are offered are injections to prevent neovascularization, delivered directly into the eye. The injected medicine can help reduce the swelling of the macula. Steroids may also be injected to help treat the swelling and limit the damage to the occluded tissue. If CRVO is severe, ophthalmologists may apply panretinal photocoagulation wherein a laser is used to make tiny burns in areas of the retina. This lowers the chance of intraocular bleedings and can prevent eye pressure from rising to sight-threatening levels.

44.1.3.3 Subretinal injection

In procedures such as antivascularization treatment, drugs are commonly administered in the vitreous humor to slow down neovascularization. Although intravitreal injections are fairly simple, when targeting cells in subretinal spaces the dose that actually reaches those cells could be very small. Subretinal injection is an alternative where drugs are directly injected in the closed subretinal space. Subretinal injection is regarded as the most effective delivery method for cell and gene therapy—including stem-cell therapy for degenerative vitreoretinal diseases such as retinitis pigmentosa, age-related macular degeneration, and Leber's congenital amaurosis [48]—despite it potentially leading more often to adverse events and possible complications [49].

44.1.4 Models used for replicating the anatomy

To support technology development for the above-mentioned procedures, a variety of synthetic, in vitro, and in vivo models have been proposed over the past decade. Table 44.3 provides an overview of the most commonly used models and some indicative references to works are described or deployed. Due to the complexity of the human eye, different models are suited for each surgical intervention, with no single model satisfying all requirements. Despite the abundance of available models, research is still ongoing to further improve the existing models. For example, for membrane peeling, Gupta et al. have been searching for representative in silico models [51]. For vein cannulation, the Rotterdam Eye Hospital has been developing an ex vivo perfused pig eye model that

TABLE 44.3 Models used for simulating and testing retinal surgeries, including membrane peeling, vein cannulation, and injections.

Model	Peeling	Cannulation	Inj.	Comment
Synthetic membranes	[26,50–52]			Peeling of membrane
Gelatin phantom			[53]	10% mimics tissue
Soft cheese			[21]	Similar OCT response
Rubber band	[54]			Simulates scleral contact
Agar	[55]	[56]	[57]	Vitreous humor
Raw chicken egg	[14,50,58]			Peeling ISM
Fertilized chicken egg	[7,12,14]	[7,12,59]		Peeling ISM
Cadaver bovine eye	[60]		[53]	W/o cornea, lens, vitreous
Cadaver pig eye		[6,9,61]	[57]	Open-sky; 40–60 μm
Perfused pig eye	[62]			Closure of vessels
In vivo pig eye	[63,64]			W/ lasering to form clots
In vivo rabbit eye	[9,65]	[9,66]		Preretinal 60 μm vessels
In vivo cat eye		[66]		Intraretinal vessels

can be used to evaluate retinal motion or vessel coagulation [62]. A modified rose bengal method has been developed to create clotted vessels in live pigs for validating cannulation performance [63,64]. A hybrid in vitro/in vivo model was proposed in Ref. [67], in which a device that enables an artificial or enucleated eye to be mounted on goggles worn by a healthy volunteer provides a means to account for patient movement during system characterization prior to in vivo studies.

44.2 Visualization in retinal surgery

As force levels remain predominantly below human perceptual thresholds, haptic feedback is of no avail in current surgical practice. This section explains the basic technology that is available for visualization. Over the years, various medical imaging technologies have played crucial roles in imaging the retina preoperatively and during interventions. In the following, we describe some of the most important modalities related to robotic microsurgery, with an emphasis on the stereo microscope (Section 44.2.1), as it plays a central role in the link between the patient and the operating physician. Section 44.2.2 introduces optical coherence tomography (OCT) as an imaging modality with rapidly increasing importance in retinal surgery.

44.2.1 Basic visualization through operative stereo microscope

Operative microscopes are the primary tool to image the surgical site during retinal microsurgery and are fully integrated into the standard of care worldwide. With several commercial vendors offering stereo microscopes (Zeiss, Leica Microsystems, Haag-Streit Surgical, TopCon Medical Systems, and bausch and lomb), most provide high-quality magnified and illuminated viewing of the surgical area. The obtained image quality results from several components are briefly summarized in the following.

44.2.1.1 Stereo microscope

At its core, a stereo microscope comprises a binocular head mount that allows the operating clinician to view the surgical site via an optical system. Typically, the optical system consists of a set of lenses and prisms that connect to an objective lens that dictates the working distance to the viewing site. Critically, the stereo microscope relies on two optical feeds that allow the operating clinician to view the retina with depth perception. Different inbuilt lenses can be selected during the procedure by means of a control knob or pedal that comes with the system to modulate imaging magnification. Most recent systems feature focal lengths of 150–200 mm, allowing crisp visualization of the eye posterior. Fig. 44.4 provides a retina view for different zoom factors. In addition, a secondary set of binoculars is often available by means of a beam splitter so that additional personnel can view the surgical procedure simultaneously. When working with digital microscopes and 3D displays, such as depicted in Fig. 44.3, anyone with dedicated 3D glasses can follow the intervention in 3D. This new layout is, hence, particularly appealing for training purposes.

Physically, stereo microscopes are mounted on the ceiling or suspended via a floor stand arm. They come with a dedicated foot pedal to control specific functionalities—including precise placement of the stereo microscope, and changing of focus or zoom—with the benefit of providing the operating clinician maximal freedom with their hands.

44.2.1.2 Additional lenses

In addition to the optical system in the stereo microscope, it is common to use an additional lens during procedures to provide a wider field of view (FOV) or improve visualization at dedicated locations of the retina. In practice, the choice of this additional lens is based on the surgical task in question. We briefly discuss some of the choices common to retinal microsurgery.

In practice, two types of additional lenses are used: noncontact and contact lenses. As the name indicates, the difference lies in whether the lens is touching the cornea. In the case of noncontact lenses, these are typically attached to the microscope by means of

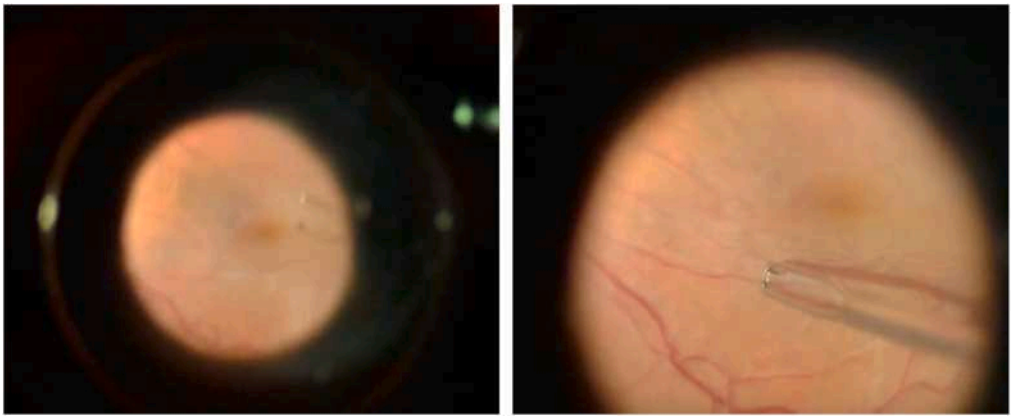

FIGURE 44.4 **Field of view from microscope.** Retina visualization with a stereo microscope and two different zoom factors. Surgical tweezers are used to delicately interact with the retina.

an adapter that can be moved manually in and out of the viewing path. In contrast, contact lenses are placed in physical contact with the eye during dedicated portions of the procedures. These are typically hand-held by an assistant or directly sutured to the eye while in use. Both types have their advantages: noncontact lenses are convenient as they do not require additional personnel or cause trauma to the eye, but they are not always properly aligned with the viewing region under consideration; conversely, hand-held or sutured lenses provide improved viewing comfort but require an additional hand.

In terms of visualization, additional lenses serve two important purposes. The first is to provide a wider FOV that can range up to 130 degrees of view (e.g., BIOM or Eibos). Such wide-angle lenses are common during vitrectomy procedures. In contrast, for procedures related to the macula such as ILM or ERM peeling, lenses that provide smaller fields of view with greater resolution are often preferred. Perhaps the most popular of this kind is the Machemer lens that provides a highly magnified 30 degrees FOV. Fundus imaging systems such as the Resight (Carl Zeiss, Fig. 44.3) contain a foldable lens support and lens turret where both types of lenses can be fitted depending on the need.

44.2.1.3 Light sources

To see the surgical site, light from the exterior must be directed onto the retina. Various options now exist to do so, and using multiple illumination types during a single procedure is common. However, induced retinal phototoxicity is an important risk factor and consequence of using illumination systems. First reported in 1966 in patients having undergone cataract surgery, phototoxicity can be either thermal or photochemical from excessive ultraviolet (UV) or blue light toxicity. Reports indicate that roughly 7% of macular hole repair patients have experienced significant phototoxicity. As such, the operating clinician must always compromise illumination with patient safety.

An integrated light source is already available with the surgical system as a primary illumination system. This light source is coaxial with the microscope's optical system, allowing the light source to travel the same path as the viewing path, which reduces shadowing effects.

Alternatively, endoilluminators are fiber-optic light pipes inserted through one of the trocars in the sclera. Most common in surgical practice are two types of light sources for such light pipes: xenon and halogen. Although both have the potential to induce phototoxicity, both are considered safe. Light pipes come in 20, 23, and 25 gauge sizes, providing a spectrum of pipe stiffness useful for eye manipulations during procedures. Today, such illumination pipes provide cone-like illuminations of up to 40- to 80-degree angles, depending on the system.

Naturally, a consequence of the light pipe endoilluminator is that the operator physician is forced to use one hand to manipulate this light source during the procedure. While this can effectively augment depth perception (via an instrument project shadow on the retina) or improve illumination of specific retinal regions, chandelier illuminations offer an alternative and give the clinician freedom in both hands. Chandelier endoilluminators provide excellent wide-angle illumination when bimanual surgical maneuvers are necessary.

44.2.1.4 Additional imaging

Before the surgical intervention, an important aspect is to visualize what areas of the retina should be manipulated during an envisioned procedure. To do this, various imaging devices and modalities are typically used in routine clinical care. These include but are not limited to:

- Color fundus imaging: It relies on a digital camera, with an electronic control of focus and aperture to image a 30- to 50-degree FOV of the retina. The technology dates back to the 1880s and can capture over 140 degrees for peripheral imaging using additional lenses. Nowadays, acquiring color fundus images is an easy and relatively inexpensive method to diagnose, document, and monitor diseases affecting the retina. Variants to color fundus photography, such as redfree imaging, which enhances the visibility of retinal vessels by removing red wavelengths, are also common.
- Fluorescein angiography: It is similar to color fundus photography except that it takes advantage of different filters and fluorescein intravenous injections to produce high-contrast images at the early stages of an angiogram. By using the camera light flashes, which are excited using a filter and then absorbed by the fluorescein, blood flow regions of the vasculature are strongly highlighted. This can then be recorded via the camera and help depict the complete vasculature of the retina. Such imaging is extremely effective in identifying retina regions with venous occlusions and other related pathologies.
- Optical coherence tomography: It is a fast and noninvasive imaging modality that can acquire micrometer-resolution three-dimensional scans of the anterior and posterior segments of the eye. Since its introduction in 1991, it has become one of the most widely used diagnostic techniques in ophthalmology. Today, OCT is used to diagnose and manage various chronic eye conditions, as it provides high-resolution imaging and visualization of relevant biomarkers such as interor subretinal fluid buildup, retinal detachments, or pigment epithelium detachments. In addition, it enables careful measurement of retinal thickness, which can be important during retinal detachment or macular hole repair procedures. Optical coherence tomography angiography (OCT-A) can also be used to yield 2D volumes of the vasculature, bypassing fluorescein injections. Similarly, Doppler OCT can be used to quantify blood perfusion. Given its strong clinical relevance and its pertinent role in the future of robotic retinal surgery, the following sections will describe OCT in detail.

44.2.2 Real-time optical coherence tomography for retinal surgery

Retinal surgery requires visualization and physical access to limited space to perform surgical tasks on delicate tissue with a micrometer scale. When it comes to viewing critical parts of the surgical region and working with micrometer accuracy, excellent

visibility and precise instrument manipulation are essential. Conventionally, visualization during microsurgery is realized by surgical microscopes, as shown in Fig. 44.2, which limits the surgeon's FOV and prevents perception of microstructures and tissue planes beneath the retinal surface. The left image in Fig. 44.2 and both sides of Fig. 44.4 show a typical microscope view of the retina surface during ILM peeling. The entire thickness of the human retina, which consists of 12 layers, is only about 350 μm, and the ILM is as thin as 1–3 μm [4]. Therefore even with advanced surgical microscope systems, such operation is extremely challenging and requires rigorous and long-term training for retinal surgeons.

So far, several well-developed imaging modalities such as magnetic resonance imaging (MRI), X-ray computed tomography (CT), and ultrasound sonogram (US) have been utilized in image-guided intervention for various kinds of surgeries [68]. However, these conventional imaging modalities are not suitable for retinal surgery because their resolution is too low, which prevents resolving the retinal microstructures. The slow imaging speed is problematic here as well. In recent years, OCT (Fig. 44.5) emerged as a popular intraoperative imaging modality for retinal surgery. OCT systems are now capable of achieving high-speed imaging over 100 cross-sectional images per second, large imaging depths of a few millimeters, and micrometer-level transverse and longitudinal resolution [69,70].

OCT systems have evolved rapidly over the past 30 years, and currently, there are many different types of commercial systems in the market. Following is a short description of each type.

- TD OCT: Time-domain OCT is the first variant of OCT that achieves depth scanning (i.e., A-scan imaging) by physically translating the position of a reference plane in function of the depth of the imaging layer that one wants to visualize. To detect the signal, a simple photodetector directly captures the intensity of the interference signal. Because the reference plane can be translated over a long distance using mechanical stages, a very long imaging depth can be achieved, typically on the order of several centimeters to tens of centimeters. However, the typical A-scan speed is less than 1 kHz. Therefore the major drawbacks of TD OCT systems are slower scanning speed and low signal-to-noise ratio (SNR).
- FD OCT: Unlike TD OCT, frequency-domain OCT (FD OCT) systems perform spectral measurements, and the depth information is deduced from Fourier transforming the OCT spectral data. Since FD OCT does not need the physical movement of the reference plane, it can be made at high speed. Furthermore, using spectral measurements significantly improves the SNR compared to TD OCT [71,72]. FD OCT system characteristics are described in detail in the next section.
- SD OCT: Spectral-domain OCT is the original variant of FD OCT that uses a spectrometer and a broadband light source to measure the OCT spectral interference signal. Most commercial OCT systems are SD-OCT type and generally operate with A-scan speeds

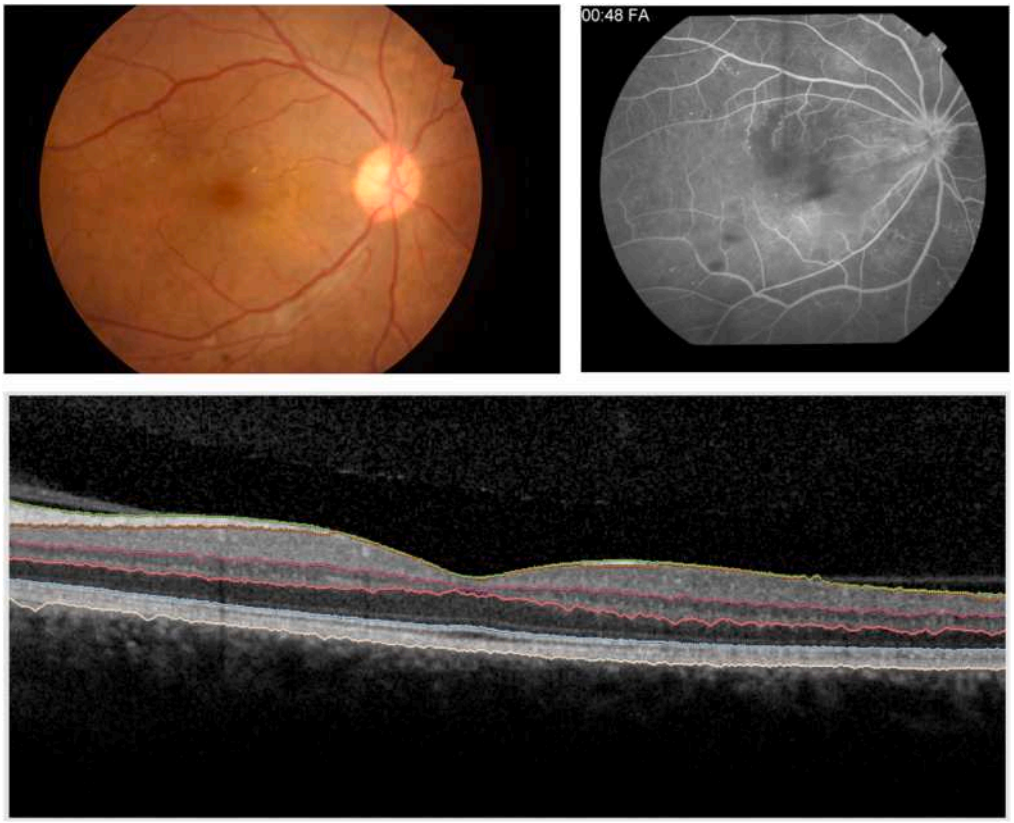

FIGURE 44.5 **Diagnostic imaging modalities.** Fundus color photography (upper left), fluorescein angiography (upper right), and optical coherence tomography (lower) are preoperative imaging modalities commonly used before retinal interventions.

of 70 Hz to 20 kHz. SD-OCT systems exhibit significant improvements in SNR compared to TD OCT and allow high-speed OCT imaging, where the imaging speed depends on the speed of a line-scan camera used in the spectrometer.

- SS OCT: Swept-source OCT is the latest development in OCT technology. It uses a wavelength-swept laser and a high-speed single photodetector to measure the OCT spectral interference signal. Typical commercial versions exhibit A-scan speeds in the range of 50–200 kHz. Typically, SS-OCT systems are faster, exhibit larger imaging depth, and offer higher SNR than SD-OCT. However, they are more expensive than SD-OCT. For example, a typical swept-source OCT engine operating at 100 kHz would cost approximately 30,000 dollars, whereas a 70 kHz OCT spectrometer engine would be in the 10,000 dollar range.
- iOCT: Intraoperative OCT generally refers to an FD OCT system integrated into a surgical microscope that allows OCT visualization during surgical procedures. Typical commercial iOCT systems provide real-time B-mode (i.e., cross-sectional) images. A postprocessed C-mode (i.e., volumetric) image can be typically generated in a few seconds. Several companies provide iOCT as an option for their high-end surgical microscope systems.
- CP OCT: Common-path OCT, unlike the standard OCT systems that use Michelson interferometer setup, does not have a separate reference arm [73,74]. Instead, it uses the signal arm as the reference arm, and the reference signal is produced from the distal end of the signal arm. Therefore the signal and the reference beam mostly share the same beam path. This allows a much simpler system design, lower associated costs, the ability to use interchangeable probes, and the freedom to use any arbitrary probe arm length. CP OCT is also immune to polarization, dispersion effects, and fiber bending. This makes CP OCT systems ideal for endoscopic applications [73].
- FD CP OCT: The Fourier domain common-path OCT is the Fourier domain variant of CP OCT.

44.2.3 Principle of Fourier domain OCT

FD OCT was first described by Fercher et al. in 1995 [75]. Over the past two decades [71,72,76–78], it has been developed rapidly and most of the commercial OCT systems are of this type. Compared to TD OCT, FD OCT has more than two orders of magnitude higher sensitivity and significantly faster imaging speed [71] with the typical A-scan imaging speed in the order of a few hundred kHz. There are two different types of FD OCT, as mentioned above: spectral-domain OCT (SD OCT), which uses a broadband light source and a dispersive spectrometer with a line-scan array detector, and swept-source OCT (SS OCT), which uses a narrow single-wavelength swept laser with a high-speed PIN detector.

Fig. 44.6 shows the schematic layout and signal processing steps of a typical spectrometer-based FD OCT (i.e., SD OCT). The spectrometer in SD-OCT uses a diffraction grating that disperses the broad-band light, several collimating lenses, and a high-speed line-scan CCD or CMOS camera to detect the spectrum of the OCT signal. The signal arriving at the line-scan camera is the

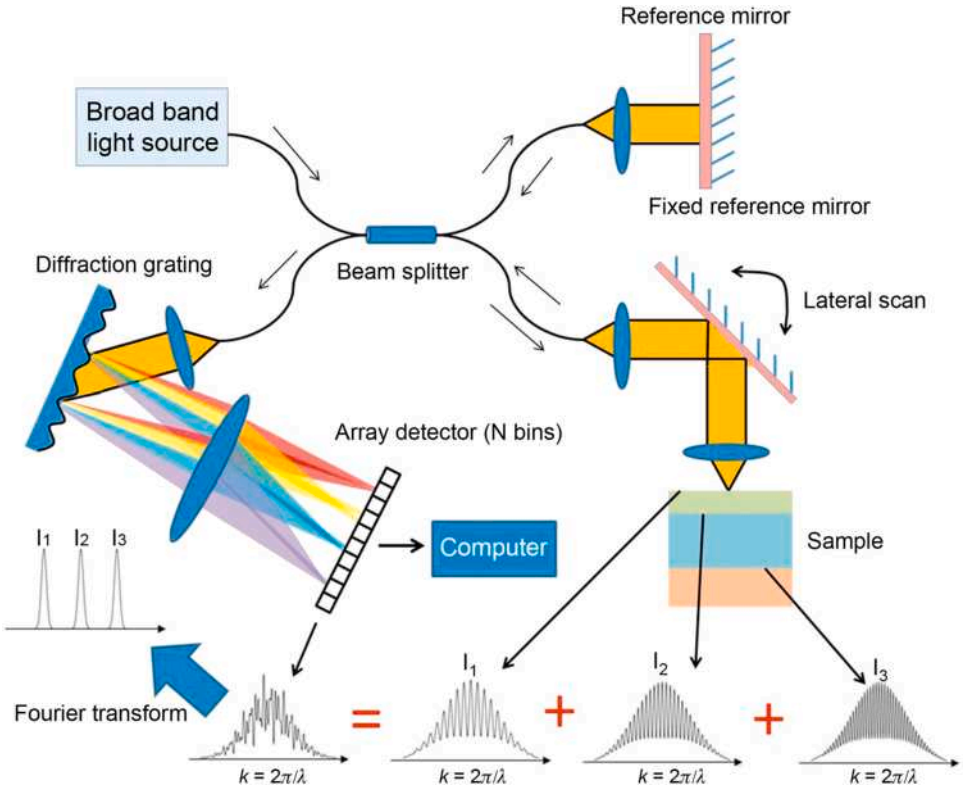

FIGURE 44.6 **A schematic of SD OCT.** A typical layout of Fourier domain OCT system based on a spectrometer (i.e., SD-OCT) is shown schematically with simplified signal processing steps.

combined interferogram of the light waves from different depths within the sample. The resultant signal spectrum $I_D(k)$ can be written as [79]:

$$\begin{aligned} I_D(k) = &\frac{\rho}{4}\left[S(k)\left(R_R + \sum_{n=1}^{N} R_{S_n}\right)\right] \\ &+ \frac{\rho}{8}\left[S(k)\sum_{n=1}^{N}\sqrt{R_R R_{S_n}}\cos(2k(z_R - z_{S_n}))\right] \\ &+ \frac{\rho}{8}\left[S(k)\sum_{m\neq n=1}^{N}\sqrt{R_{S_m} R_{S_n}}\cos(2k(z_{S_m} - z_{S_n}))\right] \end{aligned} \tag{44.1}$$

where k is the wavenumber, $S(k)$ is the power spectrum of the light source, R_R is the power reflectivity of the reference mirror, R_{Si} is the power reflectivity of the i-th layer of the sample. The depth profile or A-scan image of the sample can be obtained by taking the Fourier transform of the spectrum in Eq. (44.1). This results is a spatial domain A-scan image, which can be expressed as:

$$\begin{aligned} i_D(z) = &\frac{\rho}{8}\left[\gamma(z)\left(R_R + \sum_{n=1}^{N} R_{S_n}\right)\right] \quad \text{DC terms} \\ &+ \frac{\rho}{8}\left[\gamma(z) \otimes \sum_{n=1}^{N}\sqrt{R_R R_{S_n}}\,\delta(z \pm 2(z_R - z_{S_n}))\right] \quad \text{cross-correlation terms} \\ &+ \frac{\rho}{8}\left[\gamma(z) \otimes \sum_{m\neq n=1}^{N}\sqrt{R_{S_m} R_{S_n}}\,\delta(z \pm 2(z_{S_m} - z_{S_n}))\right] \quad \text{auto-correlation terms} \end{aligned}$$

where $\gamma(z)$ is the Fourier transform of $S(k)$. The "DC terms" correspond to the spectrum of the light source. Usually, this is the largest component of the detector signal, which needs to be subtracted before A-scan images can be displayed. The "cross-correlation terms" are the terms that form the desired OCT A-scan image. It contains several peaks whose locations are determined by the distance offset from the reference mirror position z_R and the target positions z_S. The amplitude of these peaks changes according to the light source power, the reflectivity of the reference, and the target positions within the sample. The last component, the "auto-correlation terms," comes from the interference of the light between different reflectors within the target. This results in a ghost image artifact. However, this component is usually located away from the desired signal since the distances between the different reflectors within the sample are small.

The OCT signal can be visualized as a depth-resolved 1-D image (A-Mode), a cross-sectional 2-D image (B-Mode), or a volumetric 3-D image (C-Mode); schematically shown in Fig. 44.7. In most SD-OCT systems, the signal is detected as a spectral modulation using a spectrometer which samples them uniformly in wavelength, which can be described as in Eq. (44.1). This implies that they are nonlinear in wavenumber domain. Thus applying the discrete Fourier transform or fast Fourier transform to such a signal will seriously degrade the imaging quality. A specific procedure, both in hardware and software, has been developed to reconstruct the image from the nonlinear wavenumber domain spectrum. Compared to the hardware solutions that usually complicate the design of the spectrometer and increase the cost, the software solutions are usually much more flexible and cost-efficient. There are two widely used software methods: the first one is based on numerical interpolation that includes various linear interpolations and cubic interpolation; the other one uses the nonuniform discrete Fourier transform or the nonuniform fast Fourier transformation.

44.2.3.1 Axial resolution of SD OCT

The OCT light source having a Gaussian spectral shape with a bandwidth $\Delta\lambda$ for wave- length and Δk for wavenumber, can be described mathematically as:

$$S(k) = \frac{1}{\Delta k\sqrt{\pi}} e^{-\left[\frac{k-k_0}{\Delta k}\right]^2} \tag{44.2}$$

Here, k_0 is the center wavenumber. It can be shown that its Fourier transform $\gamma(z)$ is

$$\gamma(z) = e^{-z^2\Delta k^2} \tag{44.3}$$

From Eq. (44.2), the A-scan signal is the convolution of $\gamma(z)$ and the samples structure function $\delta(z\pm2(zR-zS))$. Thus the resolution l_{axial} of the SD-OCT in the axial direction can be defined as the full width at half maximum (FWHM) of $\gamma(z)$:

$$l_{\text{axial}} = \frac{2\sqrt{\ln(2)}}{\Delta k} = \frac{2\ln(2)}{\pi}\frac{\lambda_0^2}{\Delta\lambda} \tag{44.4}$$

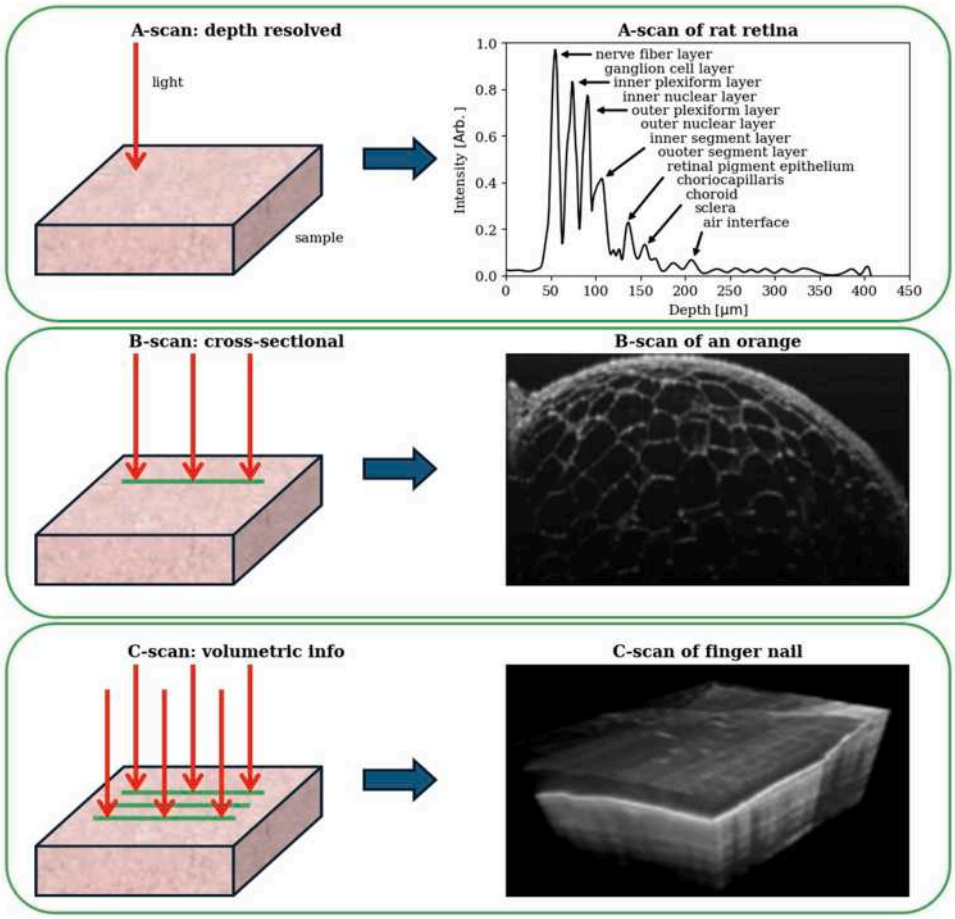

FIGURE 44.7 **OCT imaging modes.** Three different scanning/imaging modes of OCT are schematically described: A-scan (1-D), B-scan (2-D), and C-scan (3D).

Here, λ_0 is the central wavelength of the light source. As you can see the axial resolution of the OCT is determined by the bandwidth of the light source. Thus a broad-band light source is usually used in SD OCT systems to achieve high-resolution imaging.

44.2.3.2 Lateral resolution of SD OCT

In SD-OCT, the lateral resolution is defined as the full-width-half-max (FWHM) of the point spread function of the probe beam at the beam waist. Assume the numerical aperture of the objective lens before the sample is denoted as *NA*. Then the lateral resolution of SD-OCT can be expressed as:

$$l_{\text{lateral}} = \frac{2\sqrt{\ln(2)}}{\pi} = \frac{\lambda_0}{NA} \tag{44.5}$$

44.2.3.3 Imaging depth of SD OCT

In SD-OCT, the imaging depth is influenced by two factors. The first is the sample's scattering and absorption. This causes the light intensity to decrease exponentially with depth. Another factor is the spectrometer's spectral resolution. It is determined by the light bandwidth, Δk, and the number of pixels in the line-scan camera, which is denoted as N. Based on the Shannon/Nyquist theory, the maximum imaging depth of SD OCT system limited by the resolution of the spectrometer is given by:

$$z_{\max} = \frac{N\pi}{2\Delta k} \tag{44.6}$$

Eq. (44.4) shows that the axial resolution of SD OCT is inversely proportional to the bandwidth of the light source. Thus both high-resolution and large bandwidth spectral measurements are needed for SD OCT imaging that requires both large imaging depth and high axial resolution. This requires a large linear array camera which can be quite expensive. In addition, a slow sampling rate

will increase the imaging time, which makes the imaging susceptible to motion artifacts. It also produces a large amount of data that becomes a heavy burden on image storage and transfer.

44.2.3.4 Sensitivity of SD OCT

The sensitivity of an SD OCT system can be expressed as [80]:

$$\sum_{\text{SD OCT}} = \frac{\frac{1}{N}\left(\frac{\rho\eta T}{h\nu_0}P_0\right)^2\gamma_r\gamma_r R_r}{\frac{\rho\eta T}{h\nu_0}\frac{P_0}{N}\gamma_r R_r\left[1+\frac{1+\Pi^2}{2}\frac{\rho\eta}{h\nu_0}\frac{P_0}{N}\gamma_r R_r\frac{N}{\Delta\nu_{\text{eff}}}\right]+\sigma_{\text{rec}}^2} \tag{44.7}$$

Here, N is the number of pixels obtained at the detector, ρ is the efficiency of the spectrometer, η denotes the quantum efficiency of the detector, T is the CCD/CMOS detector integration time, h is Planck's constant, ν_0 is the center frequency, P_0 is the output of the source power, and γR and γS are the parts of the input power that enter the spectrometer from the reference and sample arms, respectively. R_r is the power reflectivity of the reference mirror, Π is the polarization state of the source, $\Delta\nu_{\text{eff}}$ is the effective spectral line width of the light source, and σ_{rec} is the RMS of the receiver noise. The three terms in the denominator of Eq. (44.7) have different meanings: the first is the shot noise, the second is the excess noise, and the third is the receiver noise.

44.2.4 High-speed OCT using GPU processing

Due to their fast working speed, OCT systems are suitable for use as clinical interventional imaging systems. To provide accurate and timely visualization, real-time image acquisition, reconstruction, and visualization are essential. However, in current ultrahigh-speed OCT technology, the reconstruction and visualization speeds (especially 3D volume rendering) are generally far behind the data acquisition speed. Therefore most high-speed 3D OCT systems usually work in either low-resolution modes or in a postprocessing mode, which limits their intraoperative surgical applications. To overcome this issue, several parallel processing methods have been implemented to improve the A-scan data of FD OCT images. The technique that was adopted by most commercial systems is based on multicore CPU parallel processing. Such systems have been shown to achieve an 80,000 line/s processing rate on nonlinear-k polarization-sensitive OCT systems and 207,000 line/s on linear-k systems, both with 1024-point/A-scan [81,82]. Nevertheless, the CPU-based processing is inadequate for real-time 3D video imaging even a single 3D image display can take multiple seconds. To achieve ultrahigh speed processing, GPGPU (an acronym for general purpose computing on graphics processing units) based on technology accelerate both the reconstruction and visualization of ultrahigh speed OCT imaging [78,83,84].

The signal processing flowchart of the dual-GPUs architecture is illustrated in Fig. 44.8, where three major threads are used for the FD OCT system raw data acquisition (Thread 1), the GPU accelerated FD OCT data processing (Thread 2), and the GPU-based volume rendering (Thread 3). The three threads synchronize in the pipeline mode, where Thread 1 triggers Thread 2 for every B-scan, and Thread 2 triggers Thread 3 for every complete C-scan, as indicated by the dashed arrows. The solid arrows describe the main data stream, and the hollow arrows indicate the internal data flow of the GPU. Since the CUDA technology currently does not support direct data transfer between GPU memories, a C-scan buffer is placed in the host memory for the data relay [84]. Such dual-GPU architecture separates the computing task of the signal processing and the visualization into different GPUs, which has the following advantages: (1) Assigning different computing tasks to different GPUs makes the entire system more stable and consistent. For the real-time 4D imaging mode, the volume rendering is only conducted when a complete C-scan is ready, while B-scan frame processing is running continuously. Therefore if the signal processing and the visualization are performed on the same GPU, competition for GPU resources will happen when the volume rendering starts while the B-scan processing is still going on, which could result in instability for both tasks. (2) It will be more convenient to enhance the system performance from the software engineering perspective. For example, the A-scan processing could be further accelerated, and the point spread function (PSF) could be refined by improving the algorithm with GPU-1, while more complex 3D image processing tasks such as segmentation or target tracking can be added to GPU-2.

Fig. 44.9 provides an overview of a stereo-microscope with iOCT as well as a pair of digital cameras allowing simultaneous capturing of both the pair of stereo-images as well as intraoperative OCT-images. The iOCT and digital cameras share a large part of the optical path. This is convenient as zoom adjustments will be equally reflected in the stereo camera as on the iOCT scanner. While such and similar layouts offer powerful measurement tools for capturing the retina, the quality still depends on the state and alignment of all intervening media. Advanced instruments described next (Section 44.3) bypass these problems by directly measuring inside the patient's eye.

44.2.5 3D motion-compensation in optical coherence tomography

One of the main issues with 3D iOCT imaging is that 3D image acquisition is time- consuming and often suffers from motion artifacts due to involuntary and physiologic movements of the target tissue. This is because, even during so-called steady fixation on a target, there are involuntary fixational eye movements (e.g., tremors, drifts, and microsaccades). In addition to these lateral ocular motions, another major source of involuntary eye movement is vascular pulsation or respiration, manifesting itself in motion [85]. Various methods have been developed and explored to compensate for ocular motion during OCT imaging, which may be grouped into two categories: hardware-based versus software-based solutions. The hardware approach employs additional sensing/imaging

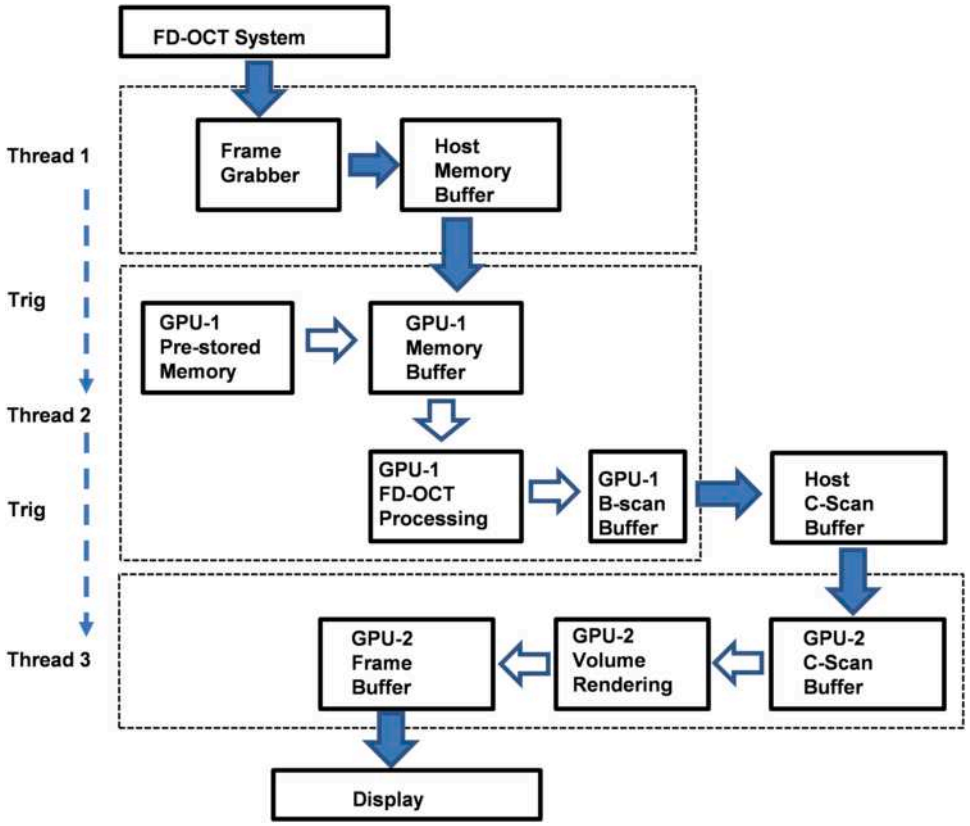

FIGURE 44.8 **Signal processing flowchart of ultrahigh-speed OCT based on dual-GPUs architecture.** Dashed arrows, thread triggering; solid arrows, main data stream; hollow arrows, internal data flow of the GPU. Here the graphics memory refers to global memory.

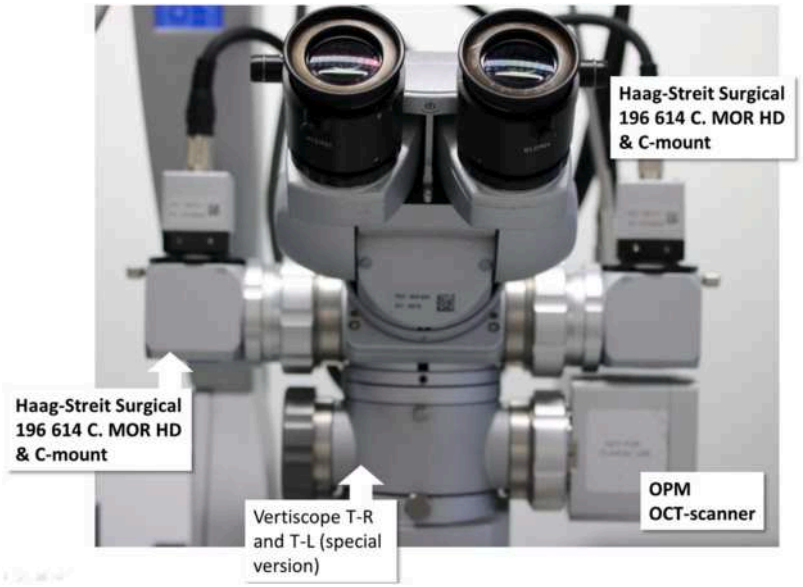

FIGURE 44.9 **Layout of a stereo-microscope with iOCT and digital cameras.** Frontal view upon a commercial stereo-microscope with mounts for digital cameras and iOCT.

devices during image acquisition to detect motion. For example, scanning laser ophthalmoscopy (SLO) data have been used as a reference to correct OCT data [86]. In general, the hardware-based methods are more complex and limited to specific applications. The software approach usually optimizes a cost function generated from a movement model [87,88]. In these approach, the motion is usually detected by obtaining prior reference scans and compare it with a 3D scan to detect the motion and perform the

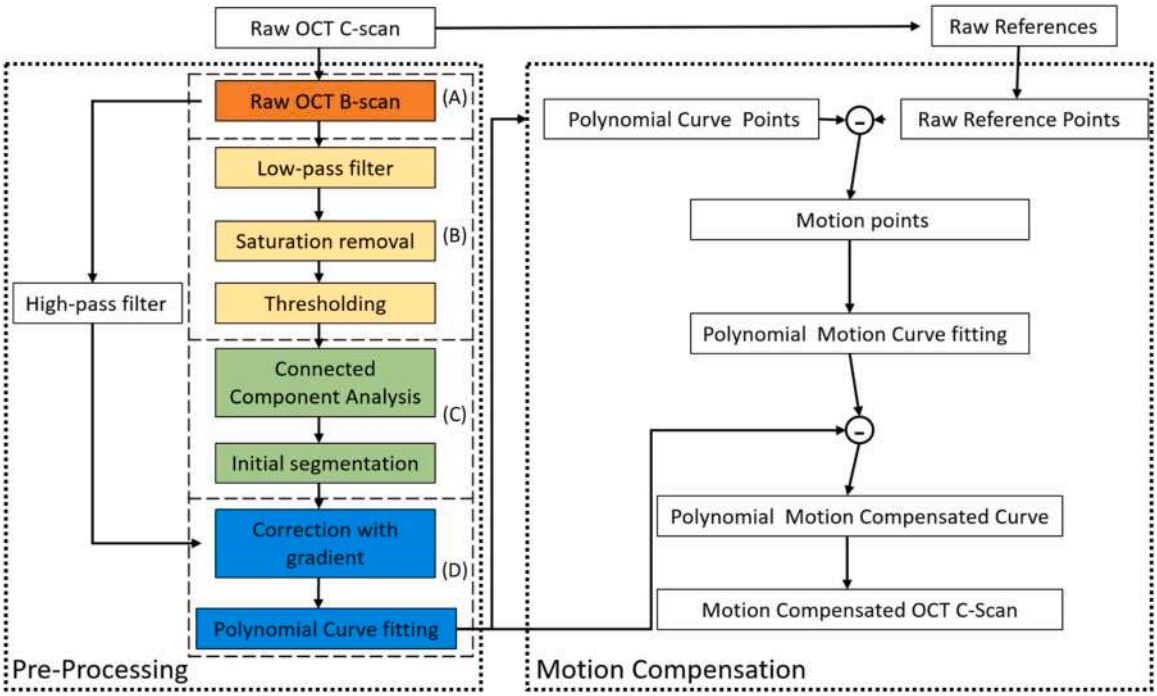

FIGURE 44.10 **Flowchart of the motion-compensated OCT system algorithm.** (Left) Preprocessing and (right) motion-compensation steps. The preprocessing procedure (left, A–D) is employed to segment the samples surface boundary and fit to a higher-order polynomial. The motion-compensation procedure is based on this preprocessing result to deduce the sample motion by comparing it with the reference images and then generates a motion-free C-scan by shifting every preprocessed B-scan accordingly.

compensation steps to correct the image. Fig. 44.10 shows a flowchart of a recent motion-compensated OCT system with (left) preprocessing and (right) motion-compensation steps [89].

The preprocessing steps are designed to accurately identify and segment tissue boundaries in both reference and subsequent B-scan images. Once that has been obtained, the lateral and axial motion compensations are performed by moving B-scan images horizontally and axially to minimize cost function and align with the reference surfaces. The result of such motion-compensated OCT imaging is shown in Fig. 44.11 using a phantom cornea model. Images (A), (D), (G), (J) are the static reference images of the phantom. The reference planes are indicated in red in panel (A). Images (B), (E), (H), (K) correspond to the sample motion around 0.4, 2.1, 3.6, and 5.2 Hz, respectively. Images (C), (F), (I), (L) are reconstructed images after using a motion compensation method. Implementing such motion compensation into clinical OCT systems has the potential to improve the reliability of 3D imaging and help improve surgical outcomes.

44.3 Advanced instrumentation

Over the last decades, advances in instrumentation have significantly altered retinal surgery practice. The development of pars plana vitrectomy in the 1970s by Machemer formed a key milestone [90]. Kasner had discovered in 1962 that the vitreous humor, the clear gel-like structure that occupies the intraocular space between the lens and retina (Fig. 44.1), could be removed a.o. providing unrestricted access to the retina [91,92]. Machemer developed pars plana vitrectomy, a minimally invasive technique to remove the vitreous humor. In this technique, a so-called vitrectome is introduced at a distance of 3–4 mm from the limbus, the place where the cornea and sclera meet. This region, the so-called pars plana, is free from major vascular structures. The retina typically starts at 6–8 mm posterior to the limbus. There is thus little risk for retinal detachment when making an incision in the pars plana to create access to the intraocular space [91]. A vitrectome, a suction cutter, is then used to remove the vitreous humor, which can be replaced by a balanced salt solution. Often a three-port approach is adopted where, aside from the vitrectome, a second incision is made to connect a supply line to provide at constant pressure the salt solution. A third incision is used to pass a light guide to provide local illumination. Vitrectomy clears the path for other instruments to operate on the retina. Modern retinal instruments include retinal picks, forceps, diamond-dusted membrane scrapers, soft tip aspiration cannulas, cauterization tools, coagulating laser fibers, chandeliers (illuminating fibers), and injection needles. There is a trend to miniaturize these instruments, with a particular focus on the diameter. In retinal surgery, the instrument diameter is expressed in the Birmingham Wire Gauge (BWG) system, often simply termed Gauge and abbreviated as G; Table 44.4 shows the corresponding dimensions in millimeter. When the diameter drops to 25 G (0.5 mm), the required incisions become self-sealing so that there is no need to suture the incisions, and the risk for inflammation is reduced. However, the 25 G instruments are more compliant and may bend (e.g., when trying to reposition the eye). Some retinal surgeons therefore prefer larger and stiffer 23 G (0.65 mm) instruments. Next to the more “traditional” instruments,

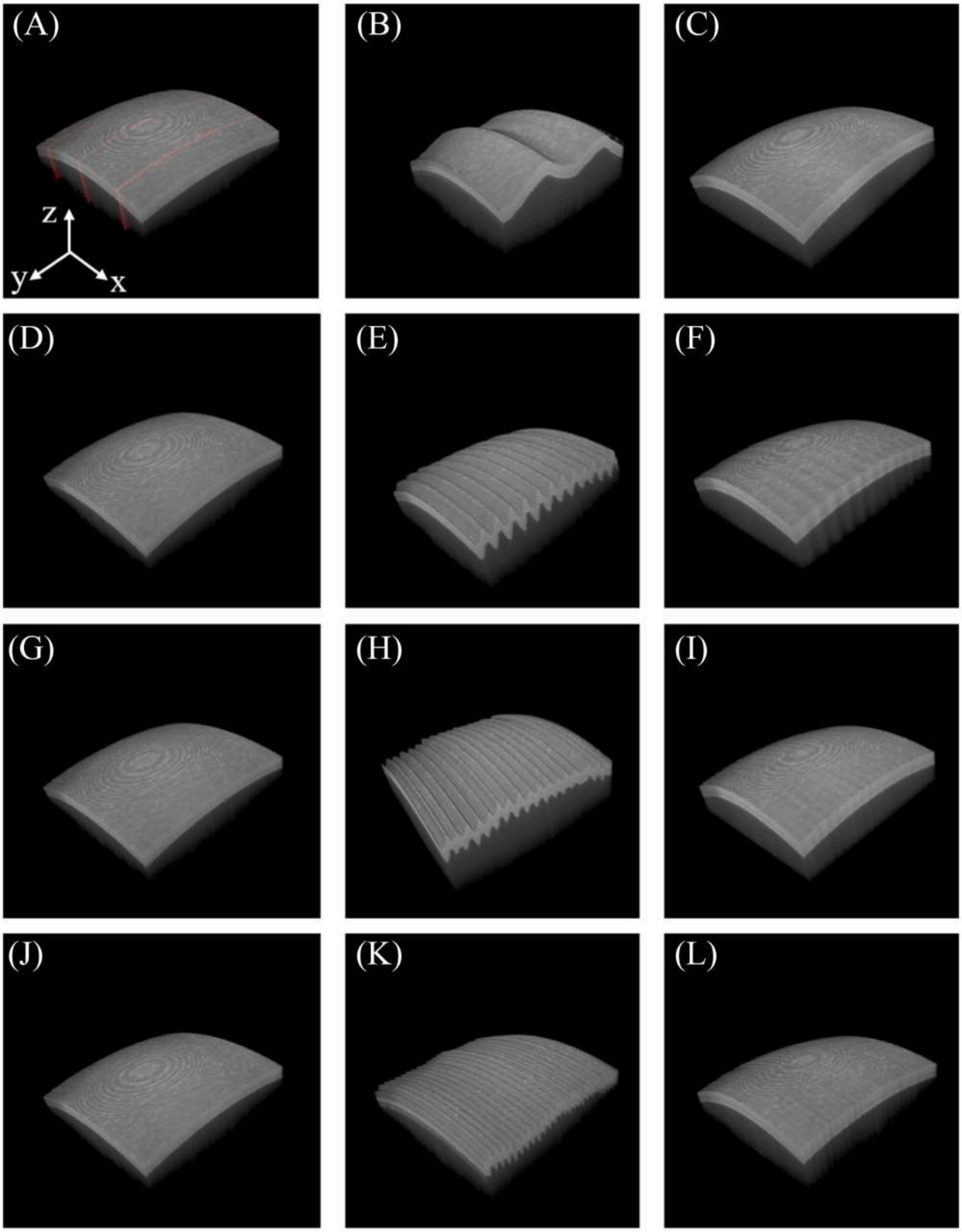

FIGURE 44.11 **3D motion-compensation result of cornea phantom.** Panels (A, D, G, J) are the static reference images of the phantom. Panels (B, E, H, K) correspond to the sample motion around 0.4, 2.1, 3.6, and 5.2 Hz, respectively. Panels (C, F, I, L) are reconstructed after using the proposed motion compensation method. Three reference planes are indicated as red lines in panel (A).

TABLE 44.4 Lookup table—instrument dimensions from Birmingham Wire Gauge system.

Gauge	20	21	22	23	24	25	26	27	28	29
mm	0.889	0.813	0.711	0.635	0.559	0.508	0.457	0.406	0.356	0.330

TABLE 44.5 Overview of sensor-integrated vitreoretinal instruments.

Measurand	Technology [references]
Retinal interaction force	Strain gauge [10,93,94]; Fabry–Perot [95,96]; FBG [14,15,18,50,97–101]
Scleral interaction force	FBG [54,102,103]
Proximity, depth	OCT [18,53,101,104,105]
Puncture	Impedance [106]
Oxygen	Photoluminescence [107]

various sophisticated instruments, featuring integrated sensing capability (Sections 44.3.1 and 44.3.2), as listed in Table 44.5, or enhanced dexterity (discused in Section 44.3.4) have been reported. In contrast to methods relying on external measurement (Section 44.2) or actuation (Section 44.5), these instruments directly measure and act in the intraocular space, bypassing the complex optical path formed by the plurality of lenses and intervening media, and avoiding the effect of the scleral interface. Therefore they potentially allow a more precise acquisition, understanding, and control over the interaction with the retinal tissue. In the following, these instruments are discussed per technology.

44.3.1 Force sensing

Fragile structures at the retina may get damaged when undergoing excessive forces. As these excessive forces often lie below human perceptual thresholds [10], this is not an imaginary problem. Gonenc et al. describe iatrogenic retinal breaks, vitreous hemorrhage as well as subretinal hemorrhages following peeling procedures [50]. When too large forces are applied on a cannulated vessel, it may tear or get pierced. This may lead to serious bleedings or unintentional injection of a thrombolytic agent in subretinal layers which would cause severe trauma. Over the years, researchers presented several sensors for measuring the force applied on retinal structures. Fig. 44.12 shows a time-line with some developments in this regard.

44.3.1.1 Retinal interaction forces

Gupta and Berkelman employed strain gauges glued upon or integrated in the instrument handle [10,93,94]. These early works provided a first insight in the governing interaction forces with the retina. Gupta showed that for 75% of the time, interaction forces stayed with 7.5 mN below human perceptional thresholds. Berkelman developed a 3-degree-of-freedom (DoF) sensor based on a double cross flexure beam design [93,94]. Aside from submillinewton precision, Berkelman's sensor behaves isotropic in 3 DoFs. With a 12.5 mm outer diameter, this sensor can only be integrated in the instrument handle. The sensor, therefore, does not only pick up the interaction forces at the retina but also forces that develop at the incision in the sclera. Since the latter are typically an order of magnitude larger [9], it is difficult to estimate the interaction forces at the retina. Therefore researchers searched for embedding sensors in the shaft of the surgical instruments to measure directly in the intraocular space.

The first intraocular force sensor by Sun et al. employed FBG (fiber Bragg grating) optical fibers [12]. Fiber optical sensors are attractive as they can be made very small, immune to electrical noise, and are sterilizable [96]. Sun started with a single 160 μm FBG strain sensor. The sensor was glued in a square channel manufactured along the longitudinal axis of a 0.5 mm diameter titanium wire, mimicking 25 G ophthalmic instruments [12]. The sensitive part of the optical fiber, that is, a 1-cm long portion where the Bragg grating resides, was positioned nearby the distal instrument tip such that interaction forces at the sclera would not be picked up. A measurement resolution of 0.25 mN was reported. During experiments on fertilized chicken eggs, forces between 8 and 12 mN were found when peeling the ISM. Forces in the range of 1–3 mN were measured during vessel cannulation experiments. In follow-up work, a 2-DoF version was developed by routing three fibers along the longitudinal axis of a 0.5-mm diameter instrument [14]. This sensor measures transverse force components perpendicular to the instrument axis. Through differential measurement, the effect of temperature could be canceled out. Experiments were conducted on respectively a raw egg

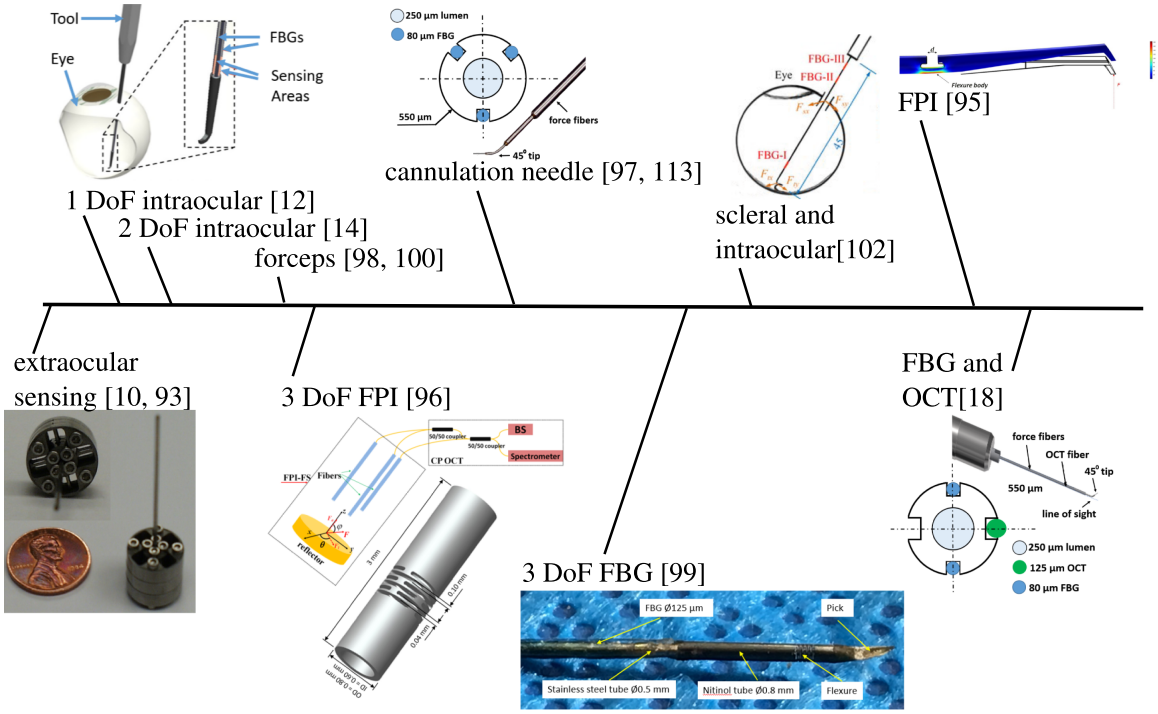

FIGURE 44.12 **Force sensing for retinal surgery.** Evolution of force sensing over the last years and integration of force sensing technology in instruments for retinal surgery.

membrane, a chorioallantoic membrane (CAM), which is an extraembryonic membrane of a fertilized chicken egg [7], and on a rabbit [15]. Peeling forces varied between 0.2–1.5 mN, 1.3–4.1 mN, for the rabbit an average minimum force to delaminate the hyaloid was 6.7 mN. Damage appeared in the CAM model when forces exceeded 5.1 mN, whereas retinal tears occurred in the rabbit from forces beyond 6.4 mN. Gonenc et al. used a similar design on a hook with the Micron, a handheld robotic instrument, to measure forces while peeling different membrane models [50]. Recently, Xu and Ko [108] proposed a novel slot-based force sensing module to be used in a submillinewton force sensing concentric tube-based eye surgery robot with a diameter of 0.43 mm and with 0.25 mN of force resolution. He et al. introduced a 3-DoF force sensing pick which is also sensitive to axial forces. A superelastic Nitinol flexure is foreseen to make the tool sensitive in axial direction [99]. RMS error was below 1 mN in all directions [99]. Furthermore, in Ref. [109], a new 3-DoF force-sensing microneedle employing a novel configuration of the FBG sensors was implemented to achieve high resolution and decoupled detection of force and to provide a hollow channel that can be used to pass through an injection catheter. A simplified structure of the FBG sensors was demonstrated in a 3-DOF force sensor with a hollow tube, which can be used as a force sensor for microneedles or forceps in retinal surgery [110].

Several works introduced microforceps with integrated force sensing [98,99,111]. Gonenc et al. foresee a method to ensure that grasping does not affect the force reading [111]. Kuru et al. developed a modular setup allowing exchange of the forceps within a nondisposable force-sensing tube [100]. Gijbels et al. developed a stainless steel cannulation needle with 2-DoF FBG sensing and a 80-µm needle tip [11,97]. The sensor resolution was 0.2 mN. Repeatable force patterns were measured when cannulating synthetic vessels in a PDMS retina [112] and cadaver pig eyes [11]. Whereas the force sensor is only sensitive to transverse forces, typical cannulation needles, including those from Gijbels [97] and Gonenc et al. [113], have a distal tip that is bent under an angle close to 45% to ease cannulation [13]. This angulation renders the sensor also sensitive to puncture forces which are hypothesized to mainly occur in the direction of the needle tip. Gonenc et al. mounted a force-sensing microneedle on the Micron handheld robotic system and cannulated vessels on a CAM surface. They reported cannulation forces rising from an average 8.8 mN up to 9.33 mN for increasing speed of respectively 0.3 to 0.5 mm/s [113]. In Gijbels' work, cannulation forces ranged between 0.6 and 17.5 mN, but in 80% of the cases they were below 7 mN [11].

Whereas the majority of works involve sensors based on FBGs, a number of instruments have been presented that employed the Fabri-Pe´rot interferometry (FPI) measurement principle [95,96]. With FPI light exiting, an optical fiber scatters back between reflective surfaces at both sides of a flexure body. Depending on the load, the flexure deforms affecting the back-scattered light. FPI is in general more affordable than FBG, but manufacturing precise flexures is challenging. A further challenge exists in making sure the instrument operates robust despite the flexure. Liu et al. used a common-path Fourier domain optical coherence tomography to interrogate the change of cavity length of an FP cavity. By multiplexing three signals, they constructed a three-dimensional force sensor with diameter below 1 mm on a retinal pick [96]. Fifanski et al. built also a retinal pick with force sensing based on FPI. This instrument has only 1 DoF but is with 0.6 mm outer diameter (OD) close to current practice [95].

44.3.1.2 Scleral interaction forces

An underappreciated limitation of current robotic systems is the lost perception of forces at the scleral interface where the tool enters the eye. During freehand manipulation, surgeons use these forces to orient the eye or to pivot about the incision such as to limit stress and/or keep the eye steady. In robot-assisted retinal surgery, the stiffness of the robotic system attenuates the users perception of the scleral forces [102]. This may induce undesired large scleral forces with the potential for eye injury. For example, Bourla et al. reported excessive forces applied to the sclera due to misalignment of the RCM of the Da Vinci [114]. He et al. developed multifunction force sensing ophthalmic tools [54,102] that simultaneously measure and analyze tool-tissue forces at the tooltip and at the tool-sclera contact point. A robot control framework based on variable admittance uses this sensory information to reduce the interaction force. He et al. reported large scleral forces exceeding 50 mN and tool deflection complicating positioning accuracy if no care was paid to the scleral interaction forces, where forces dropped to 3.4 mN otherwise [102]. Following the same control framework, a force-sensitive light guide was developed by Horise et al. that can accommodate to the patient's eye motion. Such smart light-guide could support bimanual surgery as the microsurgeon can use his/her second hand to manipulate other instruments instead of the light-guide [103]. Furthermore, Urias et al. used a similar multifunction force sensing tool to map force interaction between the instrument and sclera of in vivo rabbits during retinal procedures [115]. They showed that the mean forces using manual manipulations were 115±51 mN while, with robotic assistance, the mean forces were 118±49 mN. Using an active force control method, overall mean forces were reduced to 69±15 mN.

44.3.1.3 Force gradients

Instead of measuring the absolute interaction force for some applications such as the detection of puncture or contact state, it is more robust to look at relative chances rather than absolute forces. For example, Gijbels et al. and Gonenc et al. look at the force transient to detect the puncture of a retinal vein [11,112,113]. A threshold of −3 mN/s was found to be able to detect punctures with 98% success rate [11]. In 12% of the cases, a false-positive detection was made, for example, when upon retraction the threshold was hit. Double-punctures, that is, where the vein is pierced through, were also successfully detected as such would lead to two rapidly succeeding force transients. Puncture detection during retinal vein cannulation was further investigated by Alamdar et al. [36] in in vivo trials on rabbit eyes using sensorized metal needles. They utilized a total of four indices including two previously demonstrated ones [113] and two new indices, based on the velocity and force of the needle tip and the correlation between the needle-tissue and tool-sclera interaction forces. The new indices, when used in conjunction with the previous algorithm, improved the detection rate from 75% to 92%, but slightly increased the number of false detections from 37 to 43. Increasing the detection window improved the detection performance at the cost of adding to the delay.

44.3.2 Optical coherence tomography

Force or force gradients can help improve understanding of the current state, but offer little help to anticipate upon a pending contact or state transition, neither do they provide a lot of insight in what is present below the surface. SD OCT systems (Section 44.2.3) achieve <5 μm axial resolution in tissue [116] and have imaging windows larger than 2–3 mm. As such, they are considered very useful to enhance depth perception in retinal applications. Several researchers have developed surgical instruments with integrated optical fibers to make this imaging technology available at the instrument tip. The fibers may be directly connected to an OCT-engine or when using iOCT systems they may be routed via an optical switch to the OCT-engine, whereby the switch allows re-routing of the OCT signal to the fiber and alternatively to the intraoperative scanner [117]. The single fiber is typically introduced in a slot along the longitudinal direction of the surgical instrument and inserted alongside the instrument into the eye. The single fiber can then be used to generate an axial OCT-scan or A-scan (Fig. 44.7) that provides information of the tissue and tissue layers in front of the OCT-beam that radiates within a narrow cone from the OCT fiber. By making lateral scanning motions, the axial OCT-scan can be used to create B-scans or C-scans.

Han et al. [105] integrated a fiber optic probe with Fourier Domain Common Path OCT (FD CP OCT) [118] into a modified 25 G hypodermic needle shaped as a retinal pick. They showed how the multiple layers of the neurosensory retina can be visualized through an A-scan and further reconstructed B- and C-scans from a rat cornea. The fiber of Liu et al. [118] was also used by Yang et al. to generate B- and C-scans out of A-scans with the Micron, a handheld micromanipulator [119]. Balicki et al. embedded a fiber in a 0.5-mm retinal pick for peeling the ERM [104]. The instrument was designed so that also the tool tip itself was visible in the A-scan. Through some basic filtering, both the tool tip and the target surface could be extracted. In this layout, registration is highly simplified as the distance to the target is simply the distance between the observed tip and the observed anatomical structure, hence omitting the need to calibrate the absolute tip location. Song et al. integrated an OCT-fiber in a motorized microforceps. It assesses the relative motion of the forceps relative to the target. The fiber is glued along the outside, fixed to one "finger" of the forceps, such as to avoid artifacts when tissue is grasped [58]. Kang [53] developed a CP OCT-guided microinjector based on a similar piezo-actuation stage to conduct subretinal injections at specific depths.

Given the multilayer structure of the retina, simple peak detection algorithms may mistakenly provide the distance to a layer that differs from the retinal surface. More sophisticated algorithms were developed to take the multilayer structure into account a.o. by Cheon et al. who proposed a shifted cross-correlation method in combination with a Kalman filter [60] or Borghesan et al. who compared algorithms based on an Unscented Kalman Filter to an algorithm based on the Particle Filter [120]. Recently, within EurEyeCase, a EU-funded project on robotic retinal surgery [121], the first human experiments (five subjects) with robot-assisted

fiber-based OCT were conducted. A needle with integrated OCT-fiber was moved toward the retina. The feasibility of installing a virtual bound at a safe distance from the retina was confirmed [122]. In the same project, cannulation needles featuring combined force and OCT-sensing were developed [101] and tested in vivo on pig eyes [18]. In one of the configurations that were explored, four grooves were made along the longitudinal axis of the instrument. In two grooves, a pair of FBG optical fibers were inserted and glued. In one of the remaining grooves, an OCT fiber was glued. This latter was used to estimate the distance from the tip of the cannulation needle to the surface. The OCT-fiber was retracted with respect to the cannulation needle such that even during cannulation the OCT-fiber tip was at a certain distance from the surface allowing estimation of the depth of the cannulation relative to the retinal surface. Similarly, an OCT-based distance sensor was developed and clinically validated by Preceyes B.V. at the Eye Hospital Rotterdam [39].

44.3.3 Impedance sensing

Several works have looked at electrical impedance sensing to measure different variables. In an early work, Saito et al. used electrical conductivity for venipuncture detection in a rabbit [123]. A similar approach was followed by Schoevaerdts et al. [106,124] for eye surgery. The goal was to estimate the contact with a retinal vessel and a shift in impedance when puncturing a retinal vessel. Similar to force sensing a change in impedance was expected to occur when the sensor passed from a pure vitreous-like environment, toward a contact with a vessel wall and subsequently the contact with blood in a cannulated vessel. Experiments on ex vivo pig eyes showed a detection rate of 80%. The feasibility of detecting double punctures was also confirmed by Schoevaerdts. A side-product of the impedance sensing was found in the possibility to detect air bubbles in the supply line through which the medicine is to be injected [125]. Given the small size and fragile nature of the targeted vessels, the presence of air in a supply line forms an important problem. The air may pass through the tiny lumen of a cannulation needle and end up in the targeted vessel. Due to the lower pressure in the vessel (compared to the high pressure to push the drugs through the needle tip), the air could rapidly expand inside as it could potentially damage the targeted vessel itself. Furthermore, bio-impedance was employed to estimate the proximity between an insulated electrode and a retinal vessel [126]. Experiments on five ex vivo pig eyes with a dedicated algorithm showed 98% sensitivity and 100% specificity at a distance of 775 ± 275 μm away from the retinal vessels. Knowledge of the proximity can help the surgeon prevent damaging fragile retinal structures during retinal surgeries such as cannulation and scar tissue peeling.

44.3.4 Dexterous instruments

Where conventional retinal tools are generally straight, several instruments featuring distal dexterity have been designed up to now [16,56,127–133]. These instruments, embodiments of which are summarized in Fig. 44.13, enter the intraocular space in a straight fashion but can then be reconfigured, taking on a curved or a bent shape inside the eye. Thanks to the distal dexterity a larger part of the targeted region can be reached with reduced risk for colliding with the lens. Anatomic targets may also be reached under different angles. This in its turn can help reduce the force that is applied at the sclera.

Ikuta et al. developed a microactive forceps 1.4 mm in diameter, with built-in fiber-scope [130,134]. In Ikuta's design, a sophisticated interface allows bending the 5 mm distal segment over a range of 45 degrees while still allowing normal operation of the gripper. Wei et al. introduced a 550-μm preshaped superelastic NiTi tube. Restrained by a cannula 0.91 mm in diameter, the tube enters the eye in a straight fashion. However, the part that protrudes out of the cannula takes on its preshaped form once again. By regulating the relative displacement between NiTi tube and cannula, the bending angle is adjusted [133]. Hubschman et al. developed a microhand of which each finger is 4 mm long and 800 μm wide and consists of six pneumatically actuated phalanxes that can bend 180 degrees and each lift up to 5 mN force [129]. A stent deployment unit (SDU) was a new development from Wei

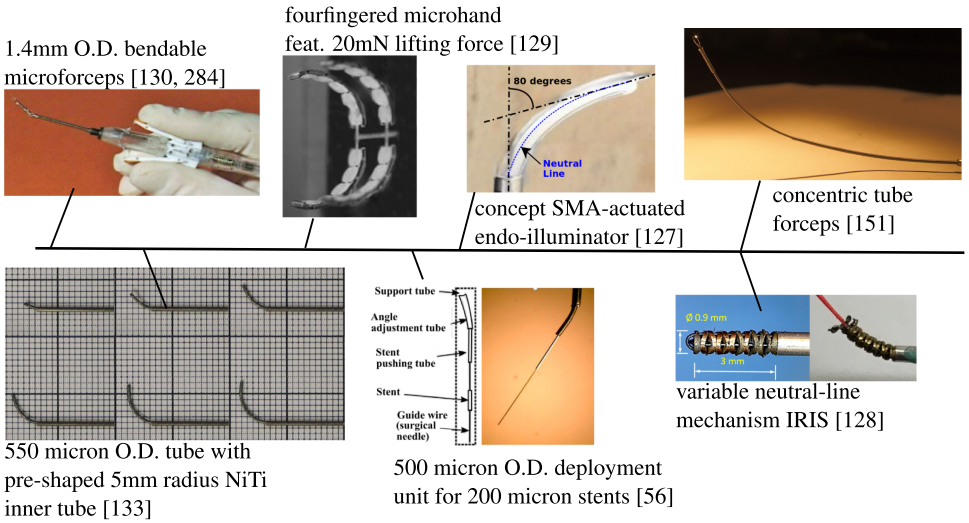

FIGURE 44.13 **Dexterous vitreoretinal instruments.** Overview of dedicated instruments featuring distal actuation capability.

et al. [56]. The SDU consists of three concentric NiTi elements: a preshaped outer tube with preshaped radius of 5 mm that bends at a specified angle when extended outside a stainless steel support tube; a stent pushing element to deliver the stent, and a guidewire to puncture and create access to the vessel. With an outer tool diameter of 550 µm, the instrument is compatible with modern dimensions. The 70 µm guidewire was used to successfully cannulate vessels in agar and in a CAM model. The authors recommended smaller stents than the 200 µm that was employed to be able to target smaller structures.

Another example of an instrument with distal DoFs is found in the IRIS system. The IRIS has an outer diameter of 0.9 mm but features 2 distal DoFs, each with ±90 degrees bending angle for only a 3-mm long section [128]. IRIS has been further improved by integrating a new drive mechanism [135] and a microgripper [136]. Cao et al. developed an endo-illuminator with 2 bending DoFs. Shape memory alloy (SMA) is used as driving method. Despite good miniaturization potential, the reported endo-illuminator was only a 10× scaled version of the targeted 25 G design. More recently, Lin et al. introduced a miniature forceps mounted on a concentric tube compatible with 23 G vitreoretinal surgery [131]. The gripper was actuated by a NiTi pull wire which is said not to interfere with the shape of the concentric tubes when actuated. The development of flexible instruments for retinal surgery is advocated a.o. by Bergeles et al. who computed a reduction of retinal forces in the order of 30% when moving flexible instruments through a model of the vitreous humor compared to steering rigid instruments through such environment [16]. The importance of Bergeles' work is to be seen in light of the growing interest toward vitrectomy-less interventions [137]. Recently, new intraocular dexterous instruments with 3 distal DoFs and force-sensing capabilities with submillinewtons resolution have been developed and evaluated in artificial [138] and animal [139] eye models, demonstrating their potential clinical value for retinal microsurgery.

44.4 Augmented reality

During an intervention, surgeons immerse themselves mentally into the intraocular space, favoring visual above nonvisual sensory channels. Under the assumption that visual feedback would minimally distract the natural flow of the operation, augmented reality has been explored extensively to convey additional contextual information. However, the augmentation of information has several specific challenges: firstly, the processing and rendering of the data has to be performed efficiently to provide timely feedback to the user. This is especially important for situations where the additional data directly provides surgical guidance, as in these cases, any delay introduced by the visualization and augmentation would create lag and negatively affect the surgical performance. Assuming the needle movement is 1 mm/s, each 10 ms of delay in one control loop will bring 10 µm position errors. Secondly, the identification of the required information to be augmented in each surgical step, as well as the registration of multimodal images, are not straightforward. As a third challenge, the visualization and rendering methods for 3D volumetric data are highly demanding regarding computational performance, especially when high visual fidelity is to be achieved.

Advanced rendering methods that apply realistic illumination simulation produce high-quality results, such as the OCT volume in Fig. 44.14 rendered with Monte-Carlo volume raycasting. These have been shown to improve the perception of important structures; however, it currently takes several seconds to generate these images and thus is not directly applicable to real-time imaging. Therefore optimizing approaches for fast rendering and high-quality augmentation is an important research task.

This section explains mosaicing, subsurface imaging, depth visualization, and pre- and intraoperatively acquired data overlaying. Furthermore, a novel approach will be discussed using auditory feedback as a form of augmentation.

44.4.1 Mosaicing

Acquiring high-resolution retinal images with a large FOV is challenging due to technological, physiological, and economic reasons. Most imaging devices used in retinal applications are slit lamp biomicroscopes; OCT machines and ophthalmic microscopes visualize only a small portion of the retina, complicating the task of localizing and identifying surgical targets, increasing treatment duration and patient discomfort. To optimize ophthalmic procedures, image processing, and advanced visualization methods can assist in creating intraoperative retina maps for view expansion (Fig. 44.15). An example of such mosaicing methods, described in Ref. [140], is a combination of direct and feature-based methods suitable for the textured nature of the human retina. The researchers in this work described three major enhancements to the original formulation. The first is a

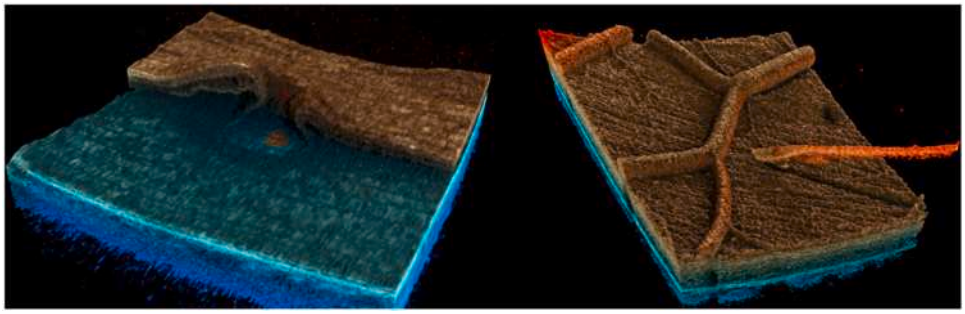

FIGURE 44.14 **OCT volume.** High-quality volume rendering of an intraoperative OCT cube from a patient with macular foramen (left); and with surgical instrument (right).

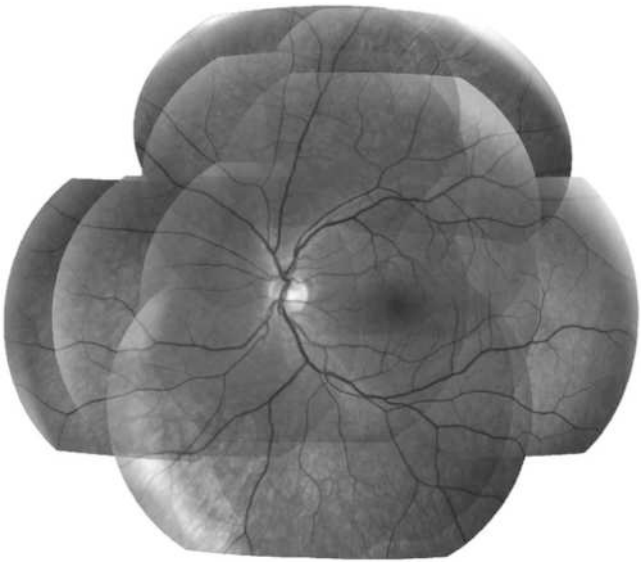

FIGURE 44.15 **Mosaicing.** Mosaicing result obtained from a set of nine images [285].

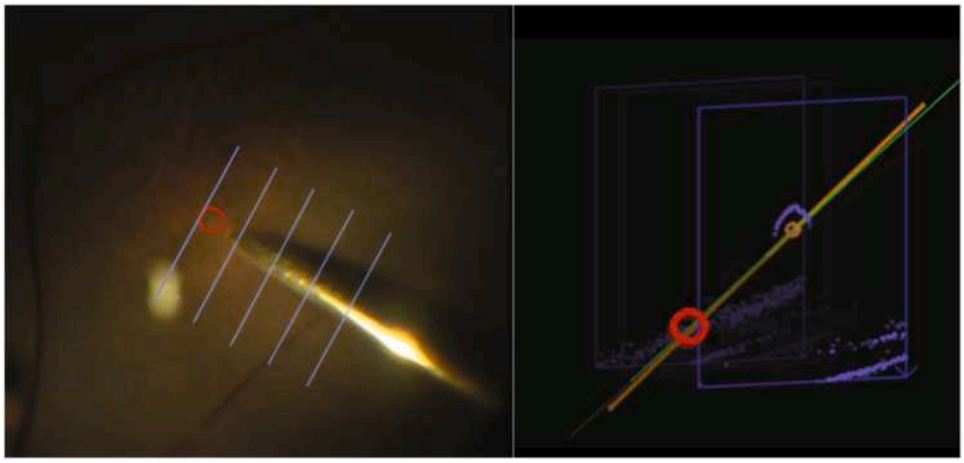

FIGURE 44.16 **Screenshot of injection guidance application.** Left: Augmented view of the surgical scene, showing the camera view with the overlaid OCT scanning locations and the projected intersection point with the RPE layer. The current and last B-scan are marked with white and blue bars for illustrative purposes. Right: Schematic view of the 3D relationships between B-scans (blue), current needle estimate (green), and intersection point with the target surface (red). These relationships cannot easily be inferred from a simple 2D microscope image.

visual tracking method using local illumination compensation to cope with the challenging visualization conditions. The second is an efficient pixel selection scheme for increased computational efficiency. The third is an entropy-based mosaic update method to improve the retina map during exploration dynamically. To evaluate the performance of the proposed method, they conducted several experiments on human subjects with a computer-assisted slit-lamp prototype. They also demonstrated the practical value of the system for photo documentation, diagnosis, and intraoperative navigation.

44.4.2 Subsurface imaging

Recent ophthalmic imaging modalities such as microscope-integrated OCT enable intraoperative visualization of microstructural anatomies in subtissue domains. Therefore conventional microscopic images are subject to modification to integrate visualization of these new modalities. Augmentation of iOCT data on en face images to the surgeon has challenges, including instrument localization and OCT-optical image registration (see Fig. 44.16). Studies describe robust segmentation methods to obtain the needlepoint cloud within the OCT volume and use retinal vessel structures for online registration of OCT and optical images of the retina [21]. Due to the infrared light source of the OCT and the geometrical features of the surgical instruments, segmentation results are robust to illumination variation and speck reflection.

44.4.3 Depth visualization

In conventional vitreoretinal surgeries, one of the important weaknesses is the lack of intraocular depth. Currently, surgeons rely on their prior experience to estimate the depth from the shadow of their instrument on the retina. Recent studies show that modern intraoperative imaging modalities such as iOCT can provide accurate depth information. Therefore augmented reality can play an important role in intuitively visualizing the depth information. As iOCT's performance currently lags behind that of the desktop counterparts, partially due to the requirements for real-time intraoperative B-scan acquisition rate, research is investigating software-based iOCT image quality enhancement on the fly. For example, in Ref. [141] iOCT quality was improved using iOCT 3D cubes as the high resolution domain, while in Ref. [142] superresolution achieved through surgical biomicroscopy guidance.

44.4.4 Vessel enhancement

The morphology of blood vessels is an important indicator for most retinal diseases. The accuracy of blood vessel segmentation in retinal fundus images affects the quality of retinal image analysis and diagnosis. Contrast enhancement is one of the crucial steps in any retinal blood vessel segmentation approach. The reliability of the segmentation depends on the consistency of the contrast over the image. Bandara and Giragama [143] presented an assessment of the suitability of a recently invented spatially adaptive contrast enhancement technique for enhancing retinal fundus images for blood vessel segmentation. The enhancement technique was integrated with a variant of the Tyler Coye algorithm, which has been improved with a Hough line transformation-based vessel reconstruction method. The proposed approach was evaluated on two public datasets, STARE [144,145] and DRIVE [146]. The assessment compared the segmentation performance with five widely used contrast enhancement techniques based on wavelet transforms, contrast limited histogram equalization, local normalization, linear unsharp masking, and contourlet transforms. The results revealed that the assessed enhancement technique is well suited for the application and outperforms all compared techniques.

In addition to retinal fundus images, OCT and OCTA are other imaging modalities that offer retinal vessel visualization. As discussed, OCT is a noninvasive, high-resolution medical imaging modality that can resolve morphological features, including blood vessel structures, in biological tissue as small as individual cells at imaging depths 1 mm below the tissue surface. An OCT extension, OCT angiography (OCTA), can image noninvasively the vasculature of biological tissue by removing the imaging data corresponding to static tissue and emphasizing the regions that exhibit tissue motion. OCTA has demonstrated great potential for characterizing vascular-related ocular diseases such as glaucoma, age-related macular degeneration, and diabetic retinopathy. Quantitative analysis of OCT and OCTA images, such as segmentation and thickness measurement of tissue layers, pattern analysis to identify regions of tissue where the morphology has been affected by a pathology from regions of healthy tissue, segmentation and sizing of blood and lymph vasculature, has a significant clinical value as it can assist physicians with the diagnosis and treatment of various diseases. However, morphological features of interest in OCT and OCTA are masked or compromised by speckle noise, motion artifacts, and shadow artifacts generated by superficial blood vessels over deeper tissue layers due to the blood cells' scattering and absorption of light. Tan et al. [147] introduced a novel image processing algorithm based on a modified Bayesian residual transform (MBRT). Tan's algorithm was developed to enhance morphological and vascular features in OCT and OCTA images.

44.4.5 Tool tracking

To integrate robotic manipulators in retinal microsurgery and to augment the clinician's perceptual ability, a critical component is the capacity to accurately and reliably estimate the location of an instrument when in the FOV. As microscopes have video recording capabilities, many methods have thus focused on real-time visual tracking of instruments from image data.

A major challenge to do so from an algorithmic point of view is that the instrument's appearance is difficult to model over time. Initially, methods relied on knowing the instrument geometry to track the instrument [148,149]. Alliteratively, visual survoing has been the basis of some methods to overcome the need to know the instrument structure before hand [150,151]. Unfortunately, such methods have difficulty dealing with prolonged tracking time and require failure-checking systems. More recent methods have leveraged machine learning methods to provide fast and robust solutions to the instrument tracking problem. This has ranged from using boosting methods [152,153] to random forests [154], as well as a variety of methods that update learned models dynamically to improve robustness [155]. Unsurprisingly, however, the recent use of deep learning methods has been shown to work extremely well in terms of 2D instrument pose localization, speed, and robustness [156–158].

Perhaps even more promising is the use of high-resolution OCT information at the 3D location of the instrument tip. Given new integrated iOCT capabilities, some preliminary results for tracking instruments with iOCT image data are possible (see Fig. 44.17) and are promising [159,160]. Such combined multimodal instrument tracking approaches may be the key to precise intraocular tracking of surgical instruments. Without a doubt, this will have considerable importance in robotic-assisted retinal microsurgery, as the intraoperative OCT has an axial resolution of 510 μm, which allows for precise depth information to be estimated and appears far better than pure stereo-based estimation [151].

When instruments are tracked, information can be displayed within an augmented–reality interface by means such as those in Fig. 44.16, or the Micron user interface, in which the relative sizes of two circles surrounding the instrument tip show the elevation of the tip in the workspace, and the distance between centers indicates when the tip is getting far from the null position (thus risking actuator saturation) [161].

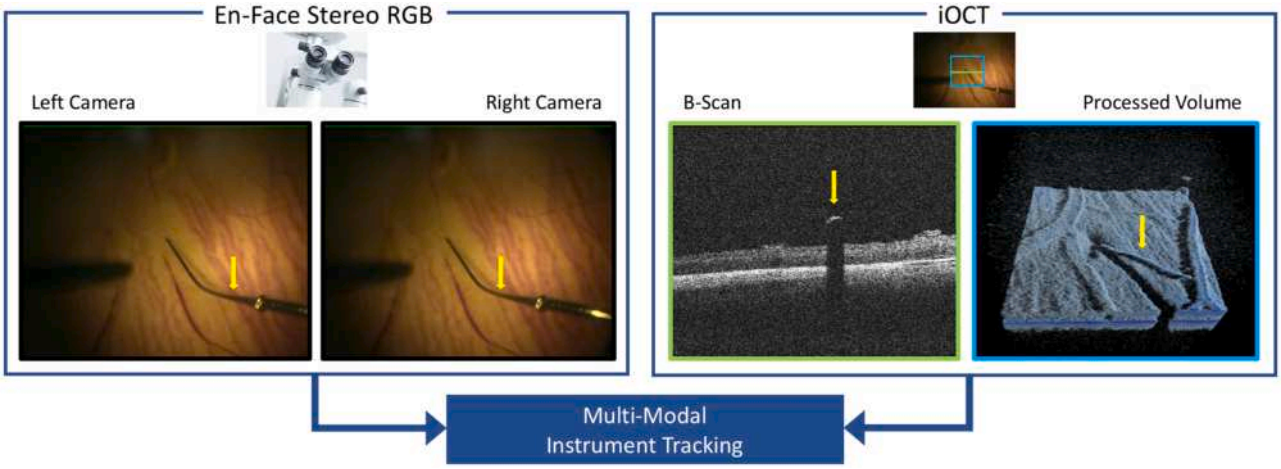

FIGURE 44.17 **Modality-specific instrument tracking approaches.** These tracking approaches are developed and combined into a robust, real-time multimodal instrument tracking approach. The yellow arrow indicates the tracked instrument.

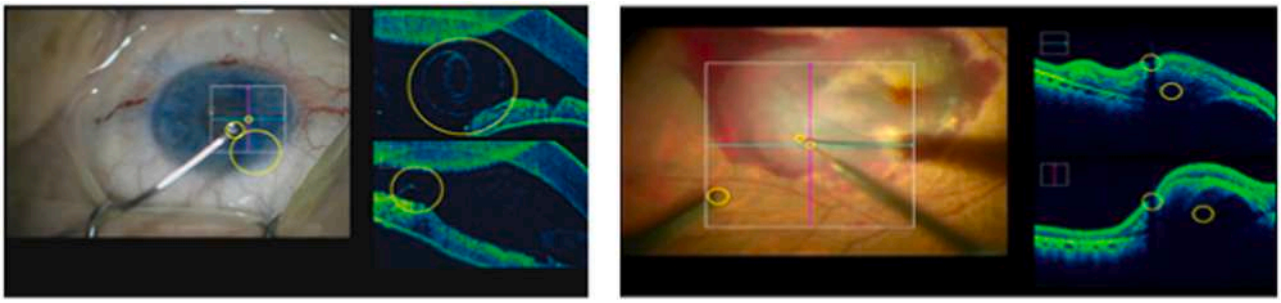

FIGURE 44.18 **One frame taken from Lumera 700 with integrated iOCT-Rescan 700 (Carl Zeiss AG).** Ophthalmic operation in posterior segment on a patient with subretinal hemorrhage; the surgeon is precisely injecting rtPA in subretinal domain. Surgeons see this side-by-side view of the optical image and OCT image intraoperatively. Yellow circles show the areas that need the surgeons attention. (Left) One frame taken from Lumera 700 with integrated iOCT-Rescan 700 (Carl Zeiss AG)—Ophthalmic operation in the anterior segment; the surgeon is performing Descemet Membrane Endothelial Keratoplasty (DMEK) operation. Surgeons see this side-by-side view of the optical image and OCT image intraoperatively. Yellow circles show areas that need surgeons attention (right).

44.4.6 Image and scenario synthesis

The development and integration of advanced modalities such as iOCT into modern operating rooms has motivated novel procedures directed at improving the outcome of ophthalmic surgeries. Although computer-assisted algorithms could further advance such interventions, the limited availability and accessibility of such systems constrains the generation of dedicated data sets. Therefore a suggested solution is novel framework combining a virtual setup and deep learning algorithms to generate synthetic data (e.g., iOCT data) in a simulated environment. Such virtual setup for iOCT data generation reproduces the geometry of retinal layers extracted from real data and allows the integration of virtual microsurgical instrument models. The scene rendering approach extracts information from the environment and considers iOCT typical imaging artifacts to generate cross-sectional label maps, which in turn are used to synthesize iOCT B-scans via a generative adversarial network [162]. Synthetic data are used for development purposes with limited availability of real data.

44.4.7 Auditory augmentation

In data augmentation and perception, the visual modality is currently dominant. However, conveying all the available information in an operational environment through the same modality may risk overstimulation and a high cognitive load, leading to inattentional blindness (see Fig. 44.18). In modern surgical rooms, there are many visual displays. Sometimes, their number is even higher than that of surgeons and physicians in the room. Following all these monitors during a surgical procedure can be very difficult.

Augmenting the cognitive field with additional perceptual modalities, such as audio, can sometimes offer a solution to this problem. Audio as a modality plays a substantial role in our perception and provides us with focused or complementary information in an intuitive fashion. Auditory display, and specifically sonification, aims at exploiting the potential of the human auditory system to expand and improve perception. This modality has been less exploited in augmented reality and robotic applications.

Sonification is the transformation of perceptualized data into nonspeech audio. The temporal and spatial advantages of the audio modality suggest sonification as an alternative or complement to visualization systems. The siren alarm of ambulances and parking guidance systems are the most known examples of sonification, providing us with the urgency and distance function intuitively. The omnidirectional nature of sound relieves the surgeon from steadily looking at the monitors and switching between monitors and patients.

The works in Refs. [163,164] suggest solutions for using sonification for surgical data augmentation and precise navigation. Sonification methods proposed for robotic vitreoretinal surgery give the surgeon aural feedback about the status of the operation. These studies investigate different digital audio effects on a music track to indicate the current anatomical area where the moving surgical tool is. Data regarding the corresponding area can be acquired from several sources, including optical coherence tomography.

44.5 State-of-the-art robotic systems

As described in Section 44.1, in retinal microsurgery the requirements for fine motor control are high, exceeding the fundamental physiological capability of many individuals. In order to enhance the capabilities of surgeons, a variety of robotic concepts have been explored that span the spectrum between conventional surgery and full robotic autonomy. As we move along that spectrum, major approaches include completely handheld systems that are completely ungrounded and maintain much of the essence of conventional surgery, cooperative-control systems in which the surgeon's hand and the robot are both in direct contact with the surgical instrument, and teleoperation systems in which the surgeon-side human-input device is distinct from the patient-side surgical robotic manipulator. As technology continues to advance, all robotic systems have the potential to be partially automated, and all but handheld devices have the potential to be fully automated, although automation has not typically been the primary motivation for the development of robotic retinal-surgery platforms. Table 44.6 provides an overview of 29 distinct robotic retinal-surgery platforms that have been described to date. An overview of the majority of these systems is assembled in Fig. 44.19. The fundamental working principles behind these systems, and associated parameters, are explained in the following.

44.5.1 Common mechatronic concepts

In this section, we begin with an introduction to some of the actuation and mechanism design concepts that are common across multiple robotic retinal-surgery platforms.

44.5.1.1 Electric-motor actuation: impedance-type versus admittance-type

The electric motor is by far the most commonly used actuator in the design of surgical robots. However, even within electric motor-based systems, varying the inertial and frictional properties—typically through the use of transmissions, such as gearing—can lead to drastically different robot dynamics, to the point of completely changing the input-output causality of the system.

At one extreme, impedance-type robots use direct-drive motors with no (or little) gearing or capstan-like cable transmissions, which results in joints with low friction and low inertia that are easily backdrivable when powered off. The pose of impedance-type robots must be actively controlled, and gravity compensation is typically employed to prevent the robot from sagging under its own weight. It can be assumed that all external loads will disturb the robot from its desired pose to some degree, although the feedback control mitigates these disturbances. From one perspective, impedance-type robots have inherent safety characteristics, in that their maximum force capability is fairly low, which limits the risk of harm to humans in direct contact. In the event of a power-loss system failure, these systems can be removed rapidly from the scene because they can be simply backdriven by hand, however, they may not "fail safe" in the sense that they may not remain in their last commanded position in the event of a power-loss system failure.

At the other extreme, admittance-type robots have a significant amount of gearing, reflected inertia, and nonlinear friction, making the joints nonbackdrivable to a substantial degree, even when powered off. An admittance-type robot will hold its pose whenever it is not actively commanded to move, and requires a control system to move (whereas an impedance-type robot requires a control system to hold its pose).

An admittance-type robot exhibits high precision, and it can be assumed that, when interacting with soft tissue, environmental disturbances have a negligible effect on the pose of the robot. From one perspective, admittance-type robots are "fail safe" in the sense that, in the event of a power-loss system failure, they remain in their last commanded position. A quick-release mechanism may need to be added if one wants to remove the instrument relatively quickly from the patient's eye in an emergency situation. Admittance-type robots may have a very high maximum force capability, which represents an inherent safety risk when in direct contact with humans.

Impedance-type and admittance-type robots can be viewed as two ends of a continuous spectrum, without definitive boundaries. For the purposes of this chapter, if a robot is difficult or impossible to move by a human when it is powered off then it will be considered an admittance-type robot; otherwise, it will be considered an impedance-type robot.

44.5.1.2 Piezoelectric actuation

Piezoelectric actuators exhibit a strain (i.e., they stretch) when a voltage is applied. These actuators are capable of extremely precise motions, typically measured in nanometers. In addition, motions can be commanded at high bandwidth. However, standard piezoelectric actuators are typically not capable of large motions.

TABLE 44.6 Overview of systems for robotic retinal surgery.

Group	Config.	Actuation	RCM	Refs.	Comments
Automatical Center of Lille	TO	AT	CT	[165,166]	RCM w/ distal insertion
Beihang Univ.	TO	AT	LI	[167]	RCM w/ proximal insertion
Carnegie Mellon Univ.	HH	PZ	—	[168,169]	6-DoF parallel
Chinese Academy of Sciences	TO	AT	LI	[170]	RCM w/ distal serial
Columbia/Vanderbilt Univ.	TO	AT	—	[133,171]	Parallel w/ distal continuum
ETH Zurich	TO	MA	—	[172,173]	Microrobot
ETH Zurich	TO	MA	—	[174,175]	Continuum
Imperial College London	TO	AT	—	[131]	Continuum
Johns Hopkins Univ.	CC	AT	LI	[176,177]	RCM w/ distal insertion
Johns Hopkins Univ.	TO	AT	LI	[128,178]	RCM w/ distal continuum
Johns Hopkins Univ.	HH	PZ	—	[53,58]	1-DoF prismatic
King's College/Moorfields	CC	AT	LI	[179]	RCM w/ distal insertion
KU Leuven	CC	IT	LI	[180,181]	RCM w/ proximal insertion
KU Leuven	TO	IT	LI	[182]	RCM w/ proximal insertion
Max Planck Institute	TO	MA	—	[183]	Microrobots
McGill Univ.	TO	IT	—	[184,185]	Parallel macro-micro
NASA-JPL/MicroDexterity	TO	IT	—	[20,186]	Serial, cable-driven
Northwestern Univ.	TO	AT	—	[187,188]	Parallel
Tianjin Univ.	TO	AT	—	[138]	Serial w/ distal continuum
TU Eindhoven/Preceyes	TO	AT	LI	[189,190]	RCM w/ distal insertion
TU Munich	TO	PZ	—	[191,192]	Hybrid parallel-serial
UCLA	TO	AT	CT	[132,193]	RCM w/ distal insertion
Univ. of Tokyo	TO	AT	CT	[194,195]	RCM w/ distal insertion
Univ. of Tokyo	TO	AT	—	[61,196]	Parallel w/ distal rotation
Univ. of Utah	TO	PZ	—	[52,197]	Serial
Univ. of Utah	TO	MA	—	[198,199]	Microrobot
Univ. of Western Australia	TO	AT	CT	[200]	RCM w/ distal PZ insertion
Vanderbilt Univ.	HH	AT	—	[201]	1-DoF prismatic
Vanderbilt Univ.	CC	AT	—	[201]	Serial w/ 1-DoF prismatic

AT, Admittance-type electric motor; *CC*, cooperatively controlled; *CT*, circular track; *HH*, handheld; *IT*, impedance-type electric motor; *LI*, linkage-based; *MA*, magnetic; *PZ*, piezoelectric actuators; *TO*, teleoperation.

Piezoelectric stick-slip actuators utilize a piezoelectric element that stretches when a voltage is applied (e.g., by 1 μm), with a distal element that is moved by the piezoelectric element through static friction. When the piezoelectric element is rapidly retracted, the inertia of the distal element causes slipping relative to the piezoelectric element, resulting in a net displacement of the distal element. The result is an actuator that is similar in behavior to a stepper motor with extremely small steps, but with a stochastic step size. By taking multiple successive steps, large net motions are possible. Piezoelectric stick-slip actuators behave much like admittance-type actuators during normal operation, in that they are very precise and they maintain their position when not commanded to move. However, they can be easily backdriven when powered off by overcoming the static friction.

Other piezoelectric motors use various forms of "inchworm" strategies in which multiple piezoelectric actuators are successively stretched and relaxed in a sequence that results in a net stepping behavior. From a high-level control perspective, these piezoelectric

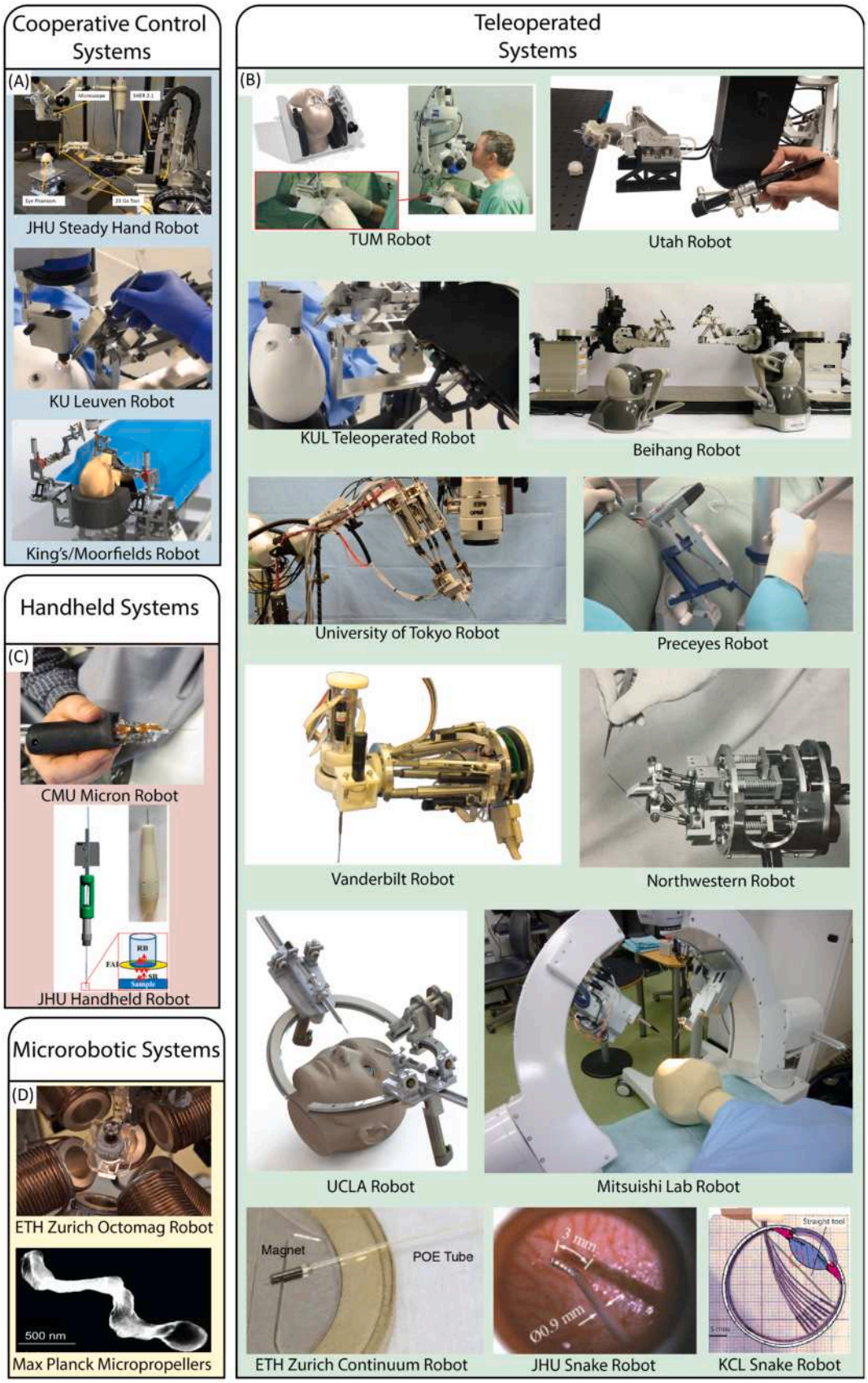

FIGURE 44.19 Representative examples of robotic retinal-surgery platforms from the categories of (A) cooperatively controlled robots, (B) teleoperated systems, (C) handheld systems, and (D) microrobotic systems.

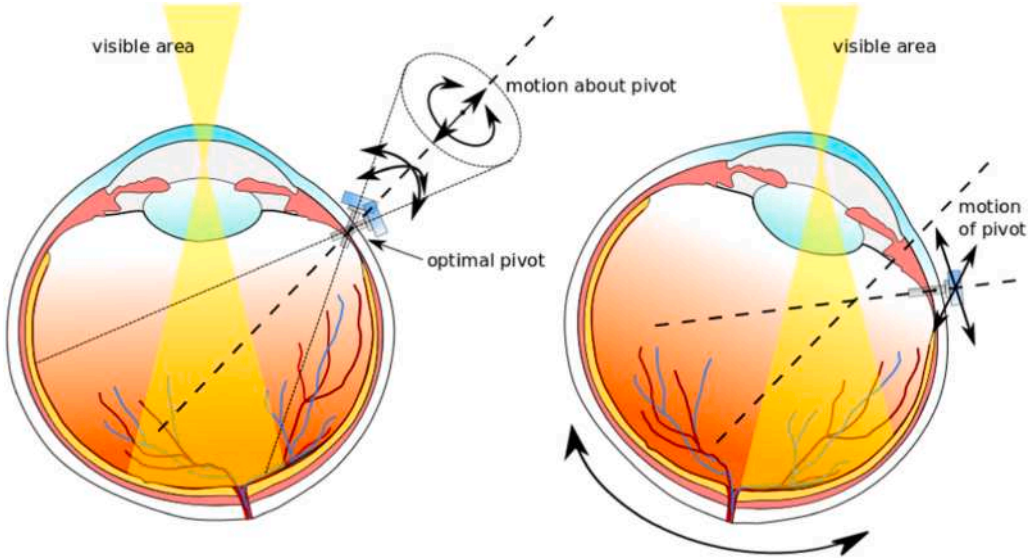

FIGURE 44.20 Instrument motion DoF divided into (left) 4 DoF that do not alter the location of an optimal pivot point located central in the pars plana; (right) 2 DoF that alter the orientation of the eye in its orbit by displacing the pars plana.

motors behave much like piezoelectric stick-slip actuators. However, piezoelectric motors are able to generate larger forces and resist higher loads before being backdriven. Another example of piezoelectric motor is the ultrasonic motor (SQL-RV-1.8 SQUIGGLE motor, New Scale Technologies, NY, USA) used in the Micron handheld robotic instrument [202], which uses a ring of piezoelectric elements to rotate a threaded rod, thus producing linear actuation with a range of motion that is limited only by the length of the threaded rod.

44.5.1.3 Remote-center-of-motion mechanisms

When the surgical instrument passes through a scleral trocar, it must be constrained to move with 4 DoFs in order to respect the constraint of the trocar; this includes 3-DoF rotation about the center of the trocar, and 1-DoF translation parallel to the shaft of the instrument (Fig. 44.20). Some retinal robots implement this kinematic constraint in software. Other robots use a dedicated remote-center-of-motion (RCM) mechanism to mechanically implement the kinematic constraint. RCM mechanisms provide an addition layer of safety, in that no system failure could cause the robot to violate the kinematic constraint of the trocar and potentially harm the sclera.

There are two basic RCM designs that have dominated the design of retinal robots (see Table 44.6). The most common is a linkage mechanism (e.g., double parallelogram) preceded proximally by a rotary joint, with axes that intersect at a point (which is the location of the RCM). The second most common is a circular track preceded proximally by a rotary joint, with axes that intersect at a point. Both of these base mechanisms are typically succeeded distally by a rotary joint to rotate the instrument about its shaft and a prismatic joint to translate the instrument along its shaft (i.e., to insert/withdraw the instrument), which completes the 4-DoF mechanism. However, recent innovations in linkage-based RCM mechanisms have eliminated the distal prismatic joint, simplifying the portion of the robot that is closest to the eye and microscope. The instrument-translation DoF is in this case enabled by a more complex proximal mechanism [167]. Optimal design of this RCM mechanism is discussed in Ref. [203].

In order to rotate the eye in its orbit to image the complete retina (Fig. 44.20), RCM mechanisms must be preceded proximally by additional DoFs to move the location of the RCM point. This is typically accomplished by a simple 3-DoF Cartesian stage, which need not have the precision of the RCM, since its only function is eye rotation, and it is not directly involved in the control of the instrument with respect to the retina. It must be noted that the inherent safety motivating the use of an RCM mechanism is somewhat reduced by the addition of this proximal positioning system, as its motion can easily violate the trocar constraint and should be conducted with sufficient care.

Although linkage-based RCM mechanisms have traditionally been designed using conventional joints, it has been shown that origami-based techniques can also be used in the design and fabrication of RCM mechanisms [204].

44.5.2 Handheld systems

The first class of retinal robotic systems that we consider are handheld devices in which mechatronic components intervene between the surgeon's hand and the tip of the instrument. Of all the systems that we consider, handheld systems are the closest to existing clinical practice and workflow, with the surgeon retaining a great deal of direct control over the instrument, including the ability to rapidly remove the instrument from the eye. Because handheld devices are mechanically ungrounded, they are able to affect, but not fully control, the steady-state pose of the instrument. In this regard, handheld systems are only robotic systems in the broadest sense,

and might be better described as "mechatronic" systems. They are best suited to compensating for small motions, particularly over time scales that are too fast for the surgeon to react. Unlike teleoperated systems, which can enhance accuracy by filtering error out of commands sent to the manipulator, handheld systems can reduce error only by means of active compensation.

The handheld-system concept that has received the most attention is the Micron system from Carnegie Mellon University [161,168,169,205–207]. The Micron uses a 6-DoF Stewart-platform (a.k.a. hexapod) parallel mechanism driven by piezoelectric motors. The motion of the handle is tracked (e.g., optically [208] or electro-magnetically [209,210]) using an external system. The control system tries to extract the intentional motion of the operator and to cancel out all unintentional motion, including the tremor of the operator's hand.

Researchers at Johns Hopkins University have created a class of "SMART" (sensorized micromanipulation aided robotic-surgery tools) instruments that incorporate 1-DoF motion control into a handheld instrument. SMART instruments incorporate a common-path OCT fiber into the instrument to measure the distance between the instrument and the retina, and use a piezoelectric motor to move the instrument's end-effector prismatically. This active DoF, which is directed normal to the retina during operation, is automatically controlled using real-time feedback from the OCT in an attempt to maintain a fixed distance between the instrument's end-effector and the retina, in spite of surgeon tremor. To date, the group has developed a microforceps [58] and a microinjector [53] based on this concept.

A similar design concept was shown in Ref. [201], in which they also demonstrated something that is likely true of many handheld systems: a handheld system can be attached to a robotic manipulator to serve as a cooperative-control or teleoperation system.

44.5.3 Cooperative-control systems

The defining feature of cooperative control, sometimes referred to as "hands-on" cooperative control or "comanipulation," is that both the surgeon's hand and the robot cooperatively hold the surgical instrument. The resulting instrument motion is defined by input commands from both the surgeon and the robot. To a lesser extent, the external environment will also affect instrument motion (mainly through bending of the thin instrument shaft). Cooperative-control systems retain much of the manipulation experience of a traditional surgery for the surgeon. Cooperative-control systems can also be used in a teleoperation configuration with only minor modifications, but the reverse is not true in general.

The earliest example of a cooperative-control system for robotic retinal surgery is the steady-hand eye robot (SHER) [98,176,177] developed at the Johns Hopkins University. The SHER comprises a 3-DoF Cartesian robot, followed distally by a linkage-based RCM mechanism, followed distally by a passive rotation joint for rotation about the instrument shaft. Because the robot does not include a dedicated prismatic actuator for instrument insertion/withdrawal, in general the RCM point at the trocar is implemented virtually, involving all DoF of the robot. However, the RCM mechanism was designed so that the mechanical RCM will correspond to the trocar (and virtual RCM) when the instrument's end-effector is interacting with the macula; in that location, very little movement of the Cartesian robot is required. The SHER is an admittance-type robot. A force sensor integrated into the instrument handle measures the force applied by the user. This force is used as an input to control the velocity of the robot (i.e., admittance control), which in the simplest case is a linear relationship that creates the effect of virtual damping. The small forces conveyed by human hand tremor can be attenuated through filtering, leading to the "steady hand" designation.

A similar admittance-type paradigm is currently being pursued at King's College London and Moorfields Eye Hospital [179]. The system comprises a 7-DoF positioning robot (a 6-DoF Stewart platform followed distally by a rotational actuator), followed distally by a linkage-based RCM mechanism, followed distally by a prismatic actuator for instrument insertion/withdrawal.

The system from KU Leuven [11,180,181] is the only cooperative-control platform that follows the impedance paradigm: the robot is impedance-type, and the controller generates a retarding force that is proportional to the velocity of the device (i.e., impedance control), creating the effect of virtual damping. This system does not require embedding a force sensor in the operator's handle. Using the impedance controller, it is also possible to mitigate unintentional and risky motions through the application of force to the surgeon-manipulated instrument. The KU Leuven system comprises a 3-DoF Cartesian robot, followed distally by a linkage-based RCM mechanism, followed distally by a passive joint for rotation about the instrument shaft. The RCM mechanism is also responsible for instrument insertion/withdrawal.

Similar to handheld systems, cooperatively controlled systems can also be made to respond to external steering commands from a distance, hence they can be readily turned into teleoperation systems [128,178,182] as was done, for example, by Gijbels et al. who experimentally compared the performance of their system in both comanipulation and teleoperated operation modes [182].

44.5.4 Teleoperated systems

Teleoperated systems comprise two distinct robotic subsystems connected via a communication channel: a patient-side manipulator that mechanically manipulates the surgical instrument, and a surgeon-side human-input device that is directly manipulated by the surgeon. The human-input device typically takes the form of a haptic interface, but other types of input devices (e.g., joysticks, 3D mice) have been used as well. Because there is not a direct physical connection between the two robotic subsystems, teleoperation systems provide more opportunities to substantially change the surgical experience of the surgeon, including position and force scaling, as well as other ergonomic improvements such as moving the surgeon away from the operating microscope to a surgeon console. In the following, we focus on the design of the patient-side manipulator, since human-input devices are easily exchanged. This Johns Hopkins system is undergoing continual improvement [211–213].

The first teleoperated retinal-surgery robot was the stereotaxical microtelemanipulator for ocular surgery (SMOS), created by researchers at the Automatical Center of Lille [165,166]. The SMOS comprised a 3-DoF Cartesian robot, followed distally by a circular-track RCM mechanism, followed distally by a prismatic actuator for instrument insertion/withdrawal, followed distally by a joint for rotation about the instrument shaft. In the years that followed, three different groups developed systems with very similar designs. The first was a group at the University of Western Australia [200]. Although the majority of their robot is driven by electric motors, the distal insertion/withdrawl stage uses a piezoelectric motor. The second was a group at the University of Tokyo [194]; it should be noted that this system was an evolution from an earlier prototype with a different circular-track RCM design [195]. The third was a group at UCLA, with the Intraocular Robotic Interventional and Surgical System (IRISS) [132,193]. IRISS had two key innovations over SMOS. The first was a tool-changer design that enabled two different instruments to be changed (automatically) in a given hand. The second innovation was the use of two circular-track RCM mechanisms, separated by the same distance as the left- and right-hand scleral trocars, mounted to a single base positioning unit, which enables a single robot to be used for bimanual manipulation (i.e., one robot "body" with two "arms"). All of the systems described above are admittance-type robots.

Although linkage-based RCM mechanisms have dominated the designs of platforms based on cooperative control, they have received relatively little attention in the context of teleoperation. The system that is the most mature, and has received the most attention, is the PRECEYES Surgical System developed by a collaboration between TU Eindhoven and AMC Amsterdam and commercialized by PRECEYES [189,190]. The patient-side manipulator is an admittance-type robot, comprising a 3-DoF Cartesian robot, followed distally by the RCM mechanism, followed distally by a prismatic actuator for instrument insertion/withdrawal, followed distally by a joint for rotation about the instrument shaft. The robot is equipped with a quick-release instrument holder such that the instrument can be swiftly removed in case of an emergency. A further noteworthy feature is that the 3-DoF proximal positioning stage is integrated in the patients headrest such that there is more knee space for the operator who sits closely to the patient and manipulates a bed-mounted human-input device. Recently a group from Beihang University [167] developed a system that is similar to the PRECEYES system, but they removed the most distal translation stage used for instrument insertion/withdrawl and modified the more-proximal RCM mechanism to provide that DoF, similar to the system from KU Leuven (see Section 44.5.3).

Four groups have developed solutions based on parallel robots, all of which implement the RCM in software. The first such system was developed at McGill University [184,185]. It was based upon two 3-DoF Cartesian robots that contacted a flexible element at two distinct locations; controlling the positions of the two 3-DoF robots enabled control of the tip of the flexible element through elastic beam bending. Each of the six actuators was designed as a two-stage, macro-micro actuator, with a high-precision piezoelectric element mounted on an impedance-type linear electric motor. The three "parallel" systems that followed were all based upon a 6-DoF Stewart platform, and all were of the admittance type, including systems from Northwestern University [187,188], the University of Tokyo [61,196], and Columbia University [56,133,171] (later pursed at Vanderbilt University [214]). The system from the University of Tokyo is similar to the system at Northwestern University, but also included an additional distal rotation DoF for rotation of the instrument about its shaft axis. The system from Columbia, the Intro-Ocular Dexterity Robot (IODR), is similar to the Northwestern system, but with a major innovation: it includes a distal 2-DoF continuum device to add dexterity inside of the eye (i.e., distal to the RCM implemented at the scleral trocar).

In the years that followed, other snake-like continuum devices have been developed that enable the instrument's end-effector to approach and manipulate the retina from different orientations. The system from Johns Hopkins University [128,135,136,178,215] is quite similar to the continuum device of the IODR, but is deployed from the SHER platform (see Section 44.5.3). The system from Imperial College London uses nested superelastic tubes, to be deployed from a unit located on the microscope [131]. It is also possible to implement continuum robots in which the continuum robot itself is a passive compliant structure with a magnetic distal tip, in which the compliant structure is bent using forces and torques on the magnetic tip controlled by an applied magnetic field [174,175] (see further discussion of this ETH Zurich system in Section 44.5.5).

Two systems have been developed based on piezoelectric stick-slip actuators. Both systems implement the RCM in software, and both systems exhibit compact designs motivated by the goal of mounting the patient-side manipulator on the patient's head. The first was the system from TU Munich [191,192], called iRAM!S (robot-assisted microscopic manipulation for vitreoretinal ophthalmologic surgery). iRAM!S uses "hybrid parallel-serial" kinematics comprising a serial chain of simple parallel mechanisms, leading to a compact design reminiscent of RCM mechanisms. The second is the system from the University of Utah [52], which uses a conventional 6-DoF serial-chain kinematic structure (3-DoF Cartesian robot followed distally by a 3-DoF spherical wrist) with the goal of eliminating uncontrolled and unsensed DoFs in the kinematic chain.

Finally, one system that stands out as being quite distinct from any other concept discussed above is the system developed as a collaboration between NASA-JPL and MicroDexterity [20,186]. In that system, the patient-side manipulator is a cable-driven impedance-type robot with serial-chain kinematics.

44.5.5 Untethered "microrobots"

A more exotic robotic approach has been pursued at ETH Zurich, where researchers have been developing untethered magnetic devices that can navigate from the sclera to the retina, driven wirelessly by applied magnetic fields, to deliver potent drugs [57,172,216,217]. Although the tiny untethered devices are referred to as "microrobots" for lack of a better term, the robotic intelligence in the system lies entirely in the external magnetic control system. From the perspective of control, magnetic actuation shares many properties of other impedance-type robots, assuming the vitreous has been removed and replaced with a liquid solution. With magnetic microrobots, force control at the retina can be accomplished in an open-loop fashion, giving magnetic microrobots

an inherent safety when compared to traditional robots. However, the forces that can be generated are also quite small, which complicates or even prohibits performing certain surgical procedures.

An alternate concept has been explored for use with an intact vitreous in which the microrobot takes the form of a miniature screw driven by magnetic torque [198,199]. The same field-generation and localization systems can be applied with this concept as well, but the nonholonomic motion of screws through soft tissue requires more sophisticated motion planning and control. Recently, researchers pushed the miniaturization envelope even further, and presented the navigation of micropropelling swimmers inside an intact porcine vitreous humor, with their results evaluated with OCT measurements [183]. The fact that the vitreous humor would not need to be removed is an appealing property warranting further investigation.

44.5.6 Clinical use cases

The first-in-human experiment was conducted in 2017 with the teleoperated PRECEYES system (Section 44.5.4). The experiment consisted of initiating a membrane-peeling procedure on six patients during a human trial at Oxford university [218]. The robot was used successfully to lift up a flap of the ERM or the ILM away from the macula surface using a beveled needle or pick. Subsequently, a subretinal injection was conducted successfully in three patients [41]. In the framework of the EurEyeCase project, the PRECEYES system has been used in another human trial at the Rotterdam Eye hospital. Here, for the first time a virtual fixture was implemented based on real-time acquired distance measurements from an OCT fiber [122]. This experiment demonstrated the feasibility of in vivo use of OCT-integrated instruments.

Contemporaneously, the cooperative-control system from KU Leuven (Section 44.5.3) was used for the first-in-human demonstration of robot-assisted vein cannulation [37]. In total, four patients with RVO were treated. A mean total infusion time of 355±204 seconds (range 120–600 seconds) was reached [219], demonstrating the safety and feasibility of robot-assisted cannulation and injection of the thrombolytic agent ocriplasmin (Oxurion, former Thrombogenics) to dissolve clots obstructing retinal veins.

In 2021 the PRECEYES system was employed for a first randomized clinical trial at the Rotterdam Eye Hospital comparing manual versus robotic membrane peeling involving respectively 5 (manual) and 10 (robotic) patients [38]. In these experiments, more steps were conducted robotically than in the peeling study at Oxford [41], namely: (1) staining of the ILM, (2) removal of dye, (3) creating an ILM flap, (4) completing of peeling, (5) light-pipe holding, and (6) fluid-air exchange. No clinical adverse events or complications were reported. Although the surgical time was longer in the robot-assisted group (mean 56 minutes, SD=12 minutes vs 24 minutes, SD=5 minutes) [38], the duration of robot-assisted surgeries decreased from 72 to 46 minutes, suggesting that further improvements in execution time are possible and shows a faster learning curve comparing to traditional manual surgery.

Finally, the system from PRECEYES has also been used for the first robot-assisted subretinal injection [40]. In a randomized controlled surgical trial, surgeons at Oxford injected TPA (tissue plasminogen activator) subretinally both in a manual (six patients) and in a robot-assisted (six patients) group. The authors noted that "this procedure closely follows the method of subretinal vector or cell suspension delivery and can thus be used as a model for future robot-assisted retinal gene or cell therapy." Safety and feasibility of robotic subretinal TPA delivery was demonstrated through these experiments, and also a similar surgical outcome was reported. Noteworthy is that these last experiments took place under local anesthesia only, which is more friendly to the typical age groups that are targeted as they tend to show poor toleration against general anesthesia [40].

44.5.7 General considerations regarding safety and usability

Regardless of the surgical robot used, there is still a risk of human error, which may lead to iatrogenic trauma and blindness. For example, excessive tool pivoting around the entry incision may lead to astigmatism, wound leak, or hypotony. Accidental motions of the tool may still puncture the retina or cause bleeding, or even touch the intraocular lens and cause a cataract [220]. All of these risks are indeed present, since the previously described robotic systems do not demonstrate "intelligence," they merely replicate or scale-down the motions of the commanding surgeon. Thus robots can improve surgical dexterity but not necessarily surgical performance. Functionalization of the tools with force or pressure sensors, as well as ophthalmic image processing, can improve the perception of the surgeon and enable him/her to link with artificial intelligence algorithms toward further improving the success rate of interventions.

A typical step in retinal surgery is a rotation of the eye in its orbit to visualize different regions of the retina. This is accomplished by applying forces at the scleral trocars with the instrument shafts. When done bimanually, surgeons have force feedback to ensure that their hands are working together to accomplish the rotation, without putting undue stress on the sclera. When using more than one robotic manipulator in retinal surgery, whether in a cooperative or teleoperated paradigm, the control system must ensure that the robots work in a coordinated fashion. This kinematically constrained problem is solved in Ref. [171].

Further, all teleoperation systems—and especially systems using curved and shape- changing instruments or untethered agents, which are very distinct from current manual techniques—require re-training of the surgical personnel to get accustomed to this remote-manipulation paradigm [221], which may disrupt surgical workflow. Many of the surgeon-side human-input devices have been designed to make this transition as intuitive as possible, and are based on either recreating the kinematic constraints of handheld and cooperative-control systems (i.e., with the surgeon's hand on the instrument handle outside of the eye) or on creating kinematics that effectively place the surgeon's hand at the end-effector of the instrument inside the eye (with the kinematic constraint of the trocar explicitly implemented in the interface). However, recent work suggests that placing the surgeon's hand at

the end-effector of the instrument, but not explicitly presenting the kinematic constraints of the trocar to the user, may lead to improved performance, likely due to the improved ergonomics that it affords [222].

Retinal robots, no matter how precise, must contend with motion of the sedated patient due to breathing and other factors. A variety of approaches have been pursued to reduce undesirable relative motion between the surgical instrument and the patient's retina. One approach is to noninvasively immobilize the patient's head with respect to the stretcher [223,224]. The robot can also be pressed against the patient's face to simultaneously immobilize the patient's head and couple the robot to the remaining head movement [192]. An alternative strategy is to actively move the patient's head to counter unintended motions [225]. Patient head motion is not inherently a problem if the robot is mounted directly to the patient's head, either via a mask/helmet-like device [197] or by mounting to the patient's upper jaw [133]. Finally, forming a mechanical connection between the robot and the eye itself, either via suction [224] or attachment to the scleral trocar [218], can provide an additional mitigation against undesired movement.

Finally, it is notable how many recent works on retinal-surgery robots have described algorithmic improvements focused primarily on safety as opposed to function [125,226–231].

44.6 Closed-loop feedback and guidance

Benefiting from feedback from sensorized instruments (Section 44.3), it becomes possible to establish high-bandwidth feedback schemes that update in real time with the changing anatomy. This section describes different feedback and guidance schemes, including haptic feedback and other force-servoing schemes. Through sensor fusion, it becomes possible to implement multirate estimation schemes that mix information and measurements, derived from preoperative or intraoperative imaging, with local sensor measurements. Feedback and guidance schemes share commonalities across hardware configurations, but in the following the discussion is organized by category, describing feedback schemes tailored for hand-held systems (Section 44.6.1), cooperative-control systems (Section 44.6.2), and finally teleoperation systems (Section 44.6.3).

44.6.1 Closed-loop control for handheld systems

The hand-held system Micron from Carnegie Mellon University (Section 44.5.2) tracks its own motion using a custom optical tracking system [208], performs filtering to determine the undesired component of motion [168], and deflects its own tip using high-bandwidth actuators in order to counteract the undesired movement of the tip [169]. Control of Micron is based on internal-model control, which provides a frequency-domain design technique that can handle underdamped dynamics, is robust under conditions of model error, and addresses time delay [232]. Due to the active nature of error compensation, performance is limited by time delay [168]. As a result, control implementation with Micron has frequently incorporated feedforward tremor suppression based on Kalman state estimation [233]. Besides the image-guided applications described in (Section 44.7), in order to provide tremor compensation when image guidance is not used, the system incorporates a high-shelf filter with negative gain as a tremor-canceling filter, providing what may be thought of as relative motion scaling below 2 Hz, with full suppression above 2 Hz [168]. Previously, notch filtering of the neurogenic component of physiological tremor was implemented [206,234], but over time experimentation made clear that achievement of significant accuracy enhancement for surgical tasks requires error suppression at frequencies considerably lower than had been foreseen, even to frequencies that overlap with voluntary movement. The controller can also be programmed to limit velocity, which may help to avoid tissue damage [235].

Micron has been used also in combination with force-sensing tools to enhance safety in tissue manipulation. Gonenc et al. [50] integrated a 2-DoF force-sensing hook tool with an earlier-generation 3-DoF Micron prototype for superior performance in membrane peeling operations. By mapping the force information into auditory signals in real time, the forces could be kept below a safety threshold throughout the operation. Furthermore, Gonenc et al. mounted a force-sensing microneedle tool on Micron, enabling an assistive feedback mechanism for cannulating retinal veins more easily [113]. The implemented feedback mechanism informs the operator upon vessel puncture and prevents overshoot based on the time derivative of sensed tool tip forces. In Ref. [111], a compact, lightweight, force-sensing microforceps module was integrated with Micron and the existing tremor cancellation software was extended to inject microvibrations on the tool tip trajectory when necessary to assist membrane delamination. Experiments on bandages and raw chicken eggs have revealed that controlled microvibrations provide ease in delaminating membranes. Automatic force-limiting control has also been demonstrated with the 6-DoF Micron system for membrane peeling using a parallel force/position control system [236].

An alternate handheld system developed for retinal surgery and highlighted in Section 44.5.2 is SMART from Johns Hopkins University [58]. SMART is a microsurgical forceps that can actively stabilize tool tip motion along the tool axis by using a fiberoptic OCT to measure the distance between tool tip and target tissue. The OCT signals are sent via feedback control to a piezoelectric motor that provides active tremor compensation during grasping and peeling functions. This closed-loop positioning function can be particularly useful for 1-DOF motion stabilization when a target tissue and an environment is delicate, and undesired collision needs to be avoided.

44.6.2 Closed-loop control for cooperative-control systems

Cooperative control is a shared control scheme where both the operator and the robot hold the surgical instrument (see Section 44.5.3). The force exerted by the operator guides the robot to comply with his/her movements. These robotic systems can be augmented with

virtual fixtures [237], and can be fitted with smart instruments possessing various sensing modalities. By way of example, smart instruments with force sensing capability may prove essential for safe interaction between the robot and the patient. The Johns Hopkins University team have developed a family of force-sensing instruments [14,96,98,99] with fiber-optic sensors integrated into the distal portion of the instrument that is typically located inside the eye. Auditory [238] and haptic [26] force-feedback mechanisms have demonstrated the potential value of regulating the tool-to-tissue forces. Initially, the Johns Hopkins University team have employed cooperative-control methods that modulate the robot behavior based on operator input and/or tool tip forces [26,239]. Later on, they extended these methods to take into consideration the interaction forces between tool shaft and sclera.

44.6.2.1 Robot control algorithms based on tool-tip force information

The earliest application of microforce sensing in cooperative robot control was proposed by Kumar et al. [239]. Balicki et al. [26] implemented this control scheme on the SHER as one of the available behaviors for assisting retinal surgery. Force scaling cooperative control maps, or amplifies, the human-imperceptible forces sensed at the tool tip (F_t) to handle interaction forces (F_h) by modulating robot velocity $\dot{x}=\alpha(F_h+\gamma F_t)$. Scaling factors of α=1, and γ=500 were chosen to map the 0–10 mN manipulation forces at the tool tip to input forces of 0–05 N at the handle. Furthermore, a force limiting behavior was developed to increase maneuverability when low tip forces are present [26]. The method incorporates standard linear cooperative control with an additional velocity constraint that is inversely proportional to the tip force:

$$\dot{x} = \begin{cases} V_{\lim}(F_t), & -F_h < V_{\lim}(F_t) \text{ and } F_t < 0 \\ V_{\lim}(F_t), & -F_h < V_{\lim}(F_t) \text{ and } F_t < 0 \\ \propto F_h, & \text{otherwise} \end{cases}$$

where $V_{\lim}(F_t)$ is a velocity limiting function described graphically in Fig. 44.21. This force limiting behavior effectively dampens the manipulation velocities.

44.6.2.2 Robot control algorithms based on sclera force information

An underappreciated limitation of current robotic systems is the suboptimal user perception of the forces present at the point that the tool passes through the sclera. With multifunction force sensing tools (Section 44.3.1.2), He et al. measures the tool-tissue forces at both the tip and the interface with the sclera. A variable admittance control method was introduced [102] to take advantage of this knowledge. The control law is: $\dot{x}ss=\alpha(Ash\ Fsh+\gamma Ass\ Fss)$ where $\dot{x}ss$ is the desired velocity of where the robot/tool contact the sclerotomy in the sclera, *Fsh* and *Fss* are the handle input force and sclera contact force resolved in the sclera frame, respectively, γ denotes the constant scalar as the force scaling factor, α denotes the constant scalar as the admittance gain, and *Ash* and *Ass* are the diagonal admittance matrices associated with the handle input force and sclera contact force in the sclera frame, respectively. A virtual RCM can be realized by setting *Ash=diag* (0, 0, 1, 1, 1, 1) and *Ass=I*. The admittance matrix *Ash* removes the transverse force components that can lead to undesired lateral motion, and preserves the 4-DoF motion that is allowed by the RCM constraints. In addition, the sclera force feedback is to servo the sclera contact force toward zero. This strengthens the virtual RCM with robustness against eye motion attributed to other instrument and/or patient movement. When the surgeon is performing RVC, the tool tip is close (or in contact) to the retina, and an RCM is desired to minimize the eye motion and the target tissue. When the surgeon needs to reposition the eye to adjust view, the tool is kept away from the retina to avoid collision. Therefore the measured insertion depth of the tool can be used to adjust the robot admittance to provide the appropriate robot behavior. We can define *Ash=diag* (1−β, 1−β, 1, 1, 1, 1) and *Ass=diag* (1+β, 1+β, 1, 1, 1, 1), where β ∈ [0, 1] could vary linearly along with the tool insertion depth as shown in Fig. 44.22 or nonlinearly [240]. When the insertion depth is smaller than the given lower bound *llb*, β=0 and *Ash=Ass=I*, we have the force-scaling control mode that provides the freedom to reposition the eye with scaled sclera force feedback. When the insertion depth is larger than the given upper bound *lub*, β=1 and it switches to virtual RCM with doubled gain for minimizing the transverse forces at the sclerotomy.

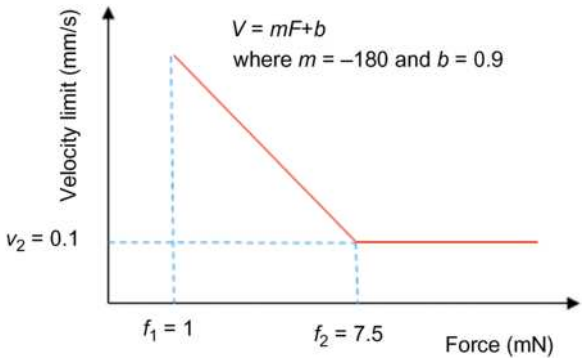

FIGURE 44.21 **Velocity limiting function.** Constraint parameters m and *b* were chosen empirically. Forces lower than f_1=1 mN do not limit the velocity. Velocity limit was set at v_2=0.1 mm/s for forces above f_2=7.5 mN [26].

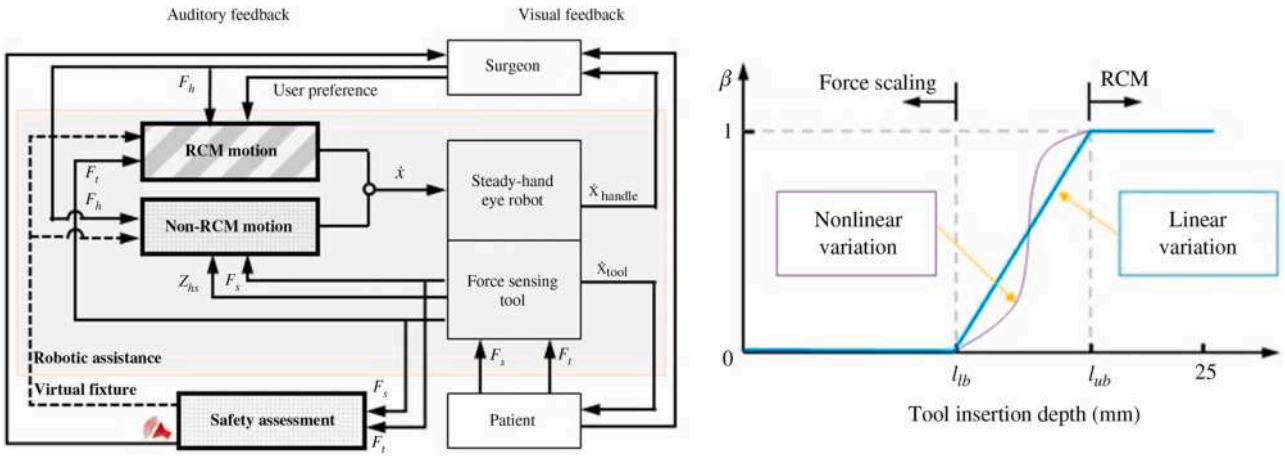

FIGURE 44.22 JHU SHER variable admittance control. Left: robot variable admittance control framework based on sclera force/position input. Right: Admittance variation (linear or nonlinear) along the insertion depth.

An adaptive control strategy similar to the one presented in Fig. 44.22 used real-time sclera force information to keep the tool-sclera contact force in a safe range while actively monitoring the insertion depth [241–243]. In Ref. [242], He et al. applied the adaptive control to robot-assisted bilateral vein cannulation with forceps and a cannula and proved that it is possible to maintain the tool-tip and sclera forces for both tools within predefined ranges, even when the eyeball was subjected to rotational disturbances.

In a recent work, Ahrononvich et al. [201] introduced a micromanipulator for robot-assisted OCT-aided extraocular subretinal injections that can serve as a handheld tool or attached to a serial robot arm for cooperative manipulation. The robotic system was capable of using distance-aware variable admittance gains based on B-Mode OCT feedback to significantly improve the user performance in regulating a needle tip to a target surface. This technology could enable a less traumatic and more accurate approach to drug delivery and support the development of future gene therapies to prevent blindness.

44.6.3 Closed-loop control for teleoperated systems

Most of the results in closed-loop control of cooperative-control systems can be applied to teleoperated systems with only minor modifications. However, in contrast to handheld systems or cooperative-control systems, teleoperation systems additionally offer the possibility to completely decouple the operator at the master side from the surgical robotic slave. Thanks to this decoupling it becomes possible to tackle physiological tremor in a number of different manners. First, it is possible to inject physical damping in the master robot's controller, effectively removing the high-frequency motion of the operator's hand. Second, it is possible to filter the signal that is sent, for example, as a reference trajectory for the slave robot to follow, in such a manner that all high-frequency components are filtered out. In a scaled teleoperation scenario, a constant scale factor is used to scale the master command to a scaled reference signal for the slave robot. In this third scenario, the amplitude of the physiological tremor would simply be transmitted in a down-scaled fashion to the slave robot. It goes without saying that a combination of above three methods may be implemented as well.

Teleoperation schemes also offer a number of options to implement virtual walls. One may choose to install a virtual wall at the master side that renders resistive forces upon entry into the forbidden zone. The operator will be slowed down. The slave robot that follows the master's motion will equally slow down as soon as the master enters the wall. Alternative one may choose to decouple the slave's motion from the master's motion with an intermediate "proxy," and effectively halt slave motion upon entry in the forbidden zone. For example, in Ref. [244] Jingjing et al. propose to compute a homo-centric sphere with radius below that of a spherical-shaped eye as boundary between a safe and a dangerous zone. In a scaled teleoperation scenario, this decoupling could correspond to "zeroing" the scale factor between master and slave. In principle, decoupling allows installing stiffer virtual walls at the slave side. In such case, penetration can be kept minimal and potentially lower than in the case of a cooperatively controlled systems where the penetration will be lower-bounded by the stiffness of the robot and its controller. In practice, the difference in stiffness may not always be significant [182], especially given the fact that operators are trained individuals that naturally operate in a responsible fashion and typically work at low speeds.

Whereas most practical teleoperation schemes are "unilateral," which means that all control signals travel down from master to slave with only visual feedback traveling back upwards to the operator, one may equally consider "bilateral" control [245,246]. By reflecting back position errors or forces measured at the slave to the master, the operator could be in principle be made aware more rapidly of the interactions that are taking place at the slave side. Balicki et al. have implemented both uni- and bilateral controllers [247]. Bilateral controllers can be made responsive to any kind of position or force tracking error [245,246]. For the former, it suffices to compute, for example, from the robot encoders of master and slave, the tracking error. For the latter, one needs to measure the interaction forces of the eye that one wants to feedback. While quite some force-sensing instruments have been developed in the past (as depicted in Fig. 44.12), most of the governing forces stay well below human thresholds [10].

"Force scaling" would thus need to be applied if one wants to render the forces to a perceivable level. While bilateral controllers tend to enhance the operator's awareness offering a more transparent way of operation in reality this may lead to stability issues [245,246]. Balicki further proposes cooperative teleoperation behavior. In this hybrid control scheme, a robot designed for cooperative control can be jointly controlled by mixing inputs from an operator handling the robot and from a second operator who provides inputs at a master console [248]. While this approach may combine the benefits from both worlds, it does require attendance of two experts who would need training to accustom to this new way of operation.

Note that while ample works in the literature describe contributions to set up visual, auditory, or haptic feedback, so far hardly any work analyzed the usability and the benefit of one feedback type versus another. This was also a finding of Griffin et al. who conducted a systematic review of the role of haptic feedback in robotic retinal surgery to conclude that even in a broader sense proper studies on human factors and ergonomics in robotic retinal surgery are missing [249].

44.7 Image-guided robotic surgery

44.7.1 Image-guidance based on video

The earliest work in this area was that of Dewan et al. [250], who described active constraints based on stereo vision to limit the motion of the Johns Hopkins University Steady-Hand Robot to follow a surface or a contour using admittance control. This work was done without a microscope, performing stereo disparity-based 3D reconstruction to constrain the robot for open-sky manipulation. Disparity-based techniques were used by Richa et al. [151] to warn the surgeon of proximity to the retina; this was tested quantitatively in a water-filled eye phantom and qualitatively in rabbit eyes in vivo, although the proximity threshold was set to 2 mm, which is very large for retinal procedures.

Becker et al. used a similar disparity-based stereo technique to develop active constraints for Micron, demonstrating accuracy enhancement in station-keeping, contour-following, a repeated move-and-hold task, and membrane peeling [161]. Implementation of active constraints with handheld systems such as Micron is fundamentally different from setting up admittance-based virtual fixtures with a grounded robot arm, however. Because Micron is not mechanically grounded, it cannot apply force to resist the motion of the human operator. Therefore active constraints must be implemented as position-based virtual fixtures [161], in which a corrective displacement of the instrument tip is automatically applied in order to constrain the tip motion to the fixture. In such an approach, the null position of the tip manipulator of the handheld system is taken as the user input to the system, and the reference position is adjusted in order to implement the fixture. Just as an admittance-type robot enables implementation of "hard" (unyielding) fixtures by setting the admittance to zero in a given direction, or "soft" (yielding) fixtures by setting the admittance to a reduced but nonzero value, likewise with position-based virtual fixtures a hard fixture can be implemented by prohibiting all motion in a given direction, whereas a soft fixture can be implemented by providing scaled motion in a given direction within the vicinity of a given location, subject to the range of motion of the manipulator.

Becker et al. [6] also used this approach to develop a virtual fixture for vessel cannulation, scaling motion by a factor of 0.5 perpendicular to the target vessel while allowing unscaled motion parallel to the target vessel. This work was demonstrated ex vivo in an open-sky porcine retina.

In a similar porcine retina model ex vivo, Becker et al. [251] implemented a hard fixture for semiautomated scanning for patterned laser retinal photocoagulation. This work performed visual servoing using the aiming beam of the treatment laser. To accommodate the limited range of motion of the 3-DoF Micron prototype at that time [168], the operator provided the gross motion from point to point. Whenever a yet-untreated target was detected within reach of the manipulator, the control system servoed the tip to the target, fired the laser, and returned the tip to its null position. Yang et al. [202] subsequently updated this work to demonstrate fully automated scanning, using a newer Micron prototype with much greater range of motion [169]. This updated work featured a hybrid visual servoing scheme, in which motion in the retinal plane was controlled via visual servoing using the microscope cameras, while motion perpendicular to the retina was handheld by closed-loop control using the optical tracker that accompanies Micron [208]—essentially, the visual compliance approach of Castan˜o and Hutchinson [252]. Direct comparison with the semiautomated approach showed that accuracy was similar at rates below one target per second, but that at higher rates the performance of the semiautomated approach dropped off due to the difficulty of the human operator in moving accurately between targets [253]. Also following a hybrid servoing approach similar to Refs. [202,253], Yu et al. [214] presented a technique for hybrid visual servoing using microscope cameras for guidance in the plane of the retina and a separate miniature B-mode OCT probe for guidance along the axis of the instrument.

Open-sky implementation allows good performance with stereo disparity-based reconstruction of the retinal surface. However, when it comes to operating in the intact eyeball, this approach is highly problematic due to the complex and nonlinear optics of the eye [207]. Recently, Probst et al. [254] presented a semidense deep matching approach that involves convolutional neural networks for tool landmark detection and 3D anatomical reconstruction; however, to date the work has been demonstrated only open-sky.

Methods that specifically model the ocular optics have been developed [172,216], but these have still yielded error on the order of hundreds of microns. To address this problem for Micron, Yang et al. [207] exploited the manipulation capability of the instrument in order to implement a structured-light approach. Before starting an intervention, this approach involves generating one or two circular scans with the laser aiming beam that are detected by the microscope cameras as ellipses. The size, aspect ratio, and orientation of the ellipses allow the retinal surface to be reconstructed. This approach to reconstruction was used by Yang et al. [207] to demonstrate automated patterned laser photocoagulation with a handheld instrument in intact porcine eyes ex vivo.

Zhou et al. [255] developed a similar approach that utilizes the elliptical shape of the project light beam itself rather than a traced path. Such approaches can be generalized by building aiming beams into other instruments besides those for laser treatment; Mukherjee et al. [256] took such an approach in preliminary experiments toward vessel cannulation. Such aiming beams also have potential to be used for proximity sensing to the surface, and intraoperative updates of retinal surface reconstruction [257].

The eyeball moves during surgery, caused sometimes by the patient, and sometimes caused by the surgeon either intentionally in order to change the view of the retina or unintentionally as a result of intraocular manipulation. In order to keep anatomical active constraints registered to the patient, it is important to accurately track the motion of the retina. There are many algorithms for segmentation of fundus images, but such algorithms are generally designed for offline use, and do not provide robust tracking in the presence of illumination changes or avoidance of mistaking intraocular instruments for vessels. To address this need, Braun et al. [258] developed a retinal tracking algorithm for intraoperative use with active constraints that uses an exploratory algorithm for rapid vessel tracing [259], with an occupancy grid for mapping and iterative closest point (ICP) for localization in the presence of instrument occlusions and varying illumination. More recently, this work was augmented by incorporating loop-closure detection [260].

Vision has also been used recently as the basis for fully autonomous manipulation, such as the system of Kim et al. [261], in which a deep neural network operating with monocular video input learned to imitate expert trajectories toward preselected target points. The work was demonstrated in simulation and in an artificial eye phantom. Furthermore, Koyama et al. [262] proposed a coordinated control algorithm for two robotic manipulators aiming shadow-based autonomous retinal positioning and recently [263] added autonomous orbital manipulation that could allow the surgeon performing vitreoretinal tasks in a wider workspace without moving the patient.

In addition to the above developments using video from cameras mounted within the operating microscope, the past few years have also seen growth in the use of microendoscopy in eye surgery [264]. Zhou et al. [265] have described deep-learning methods for reconstruction of the fundus using a robotically manipulated endoscope. Such microendoscopes may see increased use in the coming years in retinal robotic surgery.

44.7.2 Image-guidance based on optical coherence tomography

OCT represents an alternative imaging means that provides far higher resolution than microscope cameras, albeit at a much higher cost. Systems for iOCT are available commercially from numerous microscope manufacturers [266]. Efforts have begun to exploit this new means of imaging. Zhou et al. [267] described two methods to segment an intraocular surgical needle: one using morphological features of the needle as detected in the OCT images, and the other using a fully convolutional network. The methods were demonstrated in porcine eyes ex vivo. However, these methods require volumetric data sets, and do not work in real time. To address this shortcoming, Weiss et al. [160] presented a technique that uses five parallel iOCT B-scans to track the needle, detecting the elliptical section of the needle in each scan. The same group has also presented a similar technique, using a larger number of B-scans (128 along x, and the same number along y), to perform marker-free robot hand-eye calibration, which they have demonstrated in intact porcine eyes ex vivo [268]. Tracking of the needle after it enters tissue remains an open research problem [160], which the group has begun to address by registering the needle to a computer-aided design (CAD) model before the tip enters the retina, and then predicting the tip position and orientation after subretinal entry using the known input commands [21] (Fig. 44.23). More recently, Zhou et al. [158] have demonstrated a technique using microscope-integrated OCT that first crops the

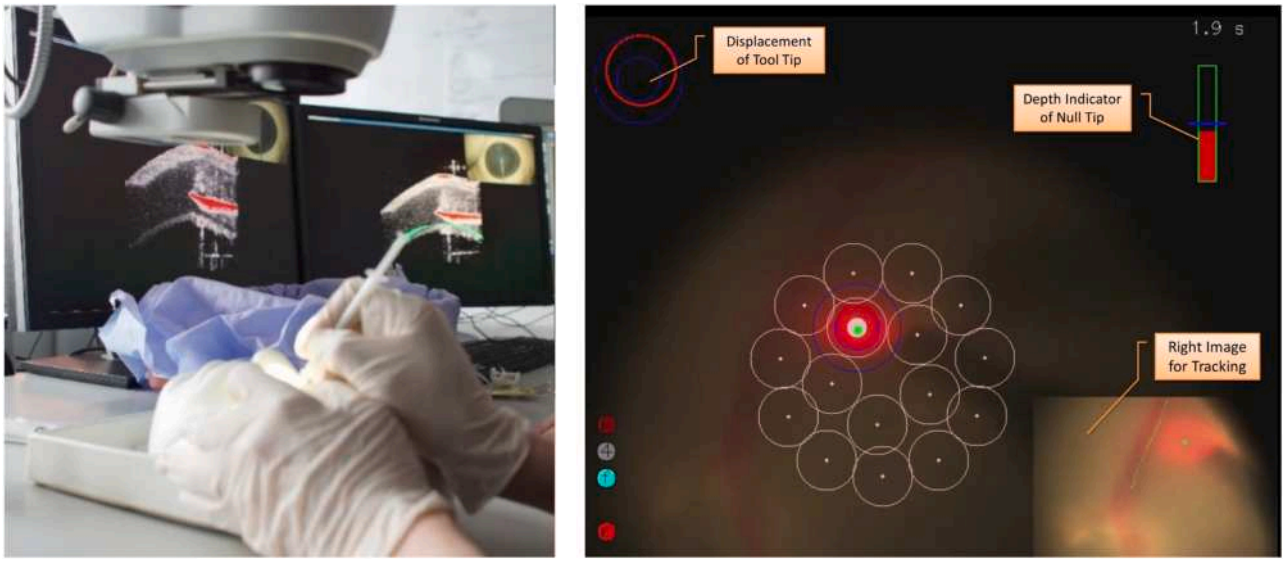

FIGURE 44.23 **Examples of research in image-guided robotic retinal surgery.** Systems are shown during preclinical testing. Left: intraoperative tracking of needles for iOCT-based servoing during retinal and subretinal injections [21]. Right: hybrid visual servoing for patterned laser photocoagulation using the Micron hand-held robotic system, performed during vitrectomy surgery in a porcine eye ex vivo [207].

region of interest to the vicinity of the needle, and then applies a convolutional neural network to OCT B-scans for localization. This technique has predicted the depth of the needle within 8.5 μm in porcine eyes ex vivo. Gerber et al. [269] have demonstrated fully automated vessel cannulation in a silicone phantom in 30 trials using microscope-integrated OCT guidance with the IRISS robot. Giudice et al. [270] also have used microscope-integrated OCT to demonstrate automated vessel cannulation with a continuum robot in an open-sky setup with an agar phantom.

OCT information can be acquired not only through the pupil, but also through intraocular surgical instruments. The laboratory of J. U. Kang at Johns Hopkins University has developed common-path swept-source OCT (CP-SSOCT) with a fiber-optic probe that is fabricated to fit within a 26 G needle [53]. The system provides an OCT A-scan with resolution of 1.8 μm over a range of 3686.4 μm from the tip of the probe. Automated scanning of an OCT probe to acquire 3D retinal imagery using this technology was demonstrated using Micron [65,119] (Fig. 44.23). Whereas Cornelissen et al. used subsequent A-scans from different needle poses, to estimate the entire retina, under the assumption of a spherical eye model based upon which virtual safety bounds could then be drafted [271]. Yang et al. obtained stabilized OCT images of A-mode and M-mode scans in air and live rabbit eyes. Jungo et al. [230] have recently demonstrated a technique based on Mahalonobis distance to indicate when readings from such instrument-integrated OCT fibers are corrupted and should therefore not be relied upon.

The Kang group has also demonstrated a wide range of capabilities using SMART handheld instruments combining their OCT technology with 1-DoF axial actuation (see Section 44.5.2). The technology can perform functions such as servoing to a selected stand-off distance from the surface [60], or actively compensating hand tremor along the axial dimension of the instrument [272]. They have also combined the technology with a motorized microforceps for epiretinal membranectomy, and have demonstrated improved accuracy and reduced task completion time in an artificial task involving picking up 125 μm optical fibers from a soft polymer surface [273]. They have used the depth servoing capability to perform subretinal injections with enhanced accuracy in a porcine retina ex vivo in an open-sky experiment [53]. Compared to freehand injection, where depth varied over a range of 200 μm, the rms error of OCT-guided injection in gelatin and ex vivo bovine eyes stayed below 7.48 and 10.95 μm, respectively [53]. The group has also developed the capability to calculate lateral displacement from the value of cross-correlation coefficient based on the speckle model, and used this to demonstrate real-time estimation of scanning speed in freehand retinal scanning in order to reduce distortion due to motion artifacts [274].

44.8 Conclusion and future work

Robotic microsurgery is still in its infancy but has already begun to change the perspective of retinal surgery. Robotic retinal surgery has been successfully carried out in a limited number of patients, using a few surgical systems such as the PRECEYES Surgical System [38,40,275,276] or the system by KU Leuven [37]. Performing new treatments such as retinal vein cannulation becomes now technically feasible due to improved stability and tremor cancellation functionality. New developments such as among others augmented reality, haptic guidance, micrometer-scale distance sensing will further impact the efficiency and reliability of these interventions. Recent contributions have led to the arrival of instruments featuring superior dexterity. These futuristic devices could initiate clinical efforts to design radically new surgical techniques. Innovations in material science, drug development, retinal chips, and gene and cell therapy are expected to create a whole new set of engineering challenges. Together with advances in imaging, robotics has become among the most promising trends in advancing the field of retinal microsurgery. As a result, an increasing number of academic institutions embark on research projects to investigate ever more powerful systems. This section identifies the main challenges ahead, striving to outline the direction of the next decade of research in retinal surgery.

44.8.1 Practical challenges ahead

There are several challenges in the road ahead. Existing robotic systems are still very expensive and should be first adopted and accepted by surgeons, clinical staff including operating room (OR) technicians and patients to become sufficiently useful in the OR. At that point, the OR culture will need to change. Dedicated training programs, like the one proposed by He et al. [277], would need to be developed and robotic surgery should be included in the surgical curriculum. Further, robotic systems need to be developed so that currently demanding interventions are achieved, as, for example, retinal vein cannulation or highly challenging such as subretinal delivery of novel therapeutics. Technical feasibility alone is not sufficient, as the safety and effectiveness of supplied substances and drugs must be validated as well. An important challenge for robot developers is hence to establish of a solid collaboration with the pharmaceutical industry. The adoption of robotic systems in commonplace procedures such as epiretinal membrane peeling, which despite its dexterity requirement is routinely and successfully performed in the western world, does not support the high cost of introducing a robot into the OR. The added value is too restricted for these scenarios. Therefore we anticipate that the way forward for retinal surgical robotics will depend on a combination of the following three key characteristics: (1) system optimization including enhancing the usability, reduction of cost, and miniaturization in order to reduce the space occupation in the OR; (2) the capability to deliver targeted drugs and substances ultra-minimally invasively, opening the path to new treatment methods; and (3) automation to enable the parallel execution of a plurality of surgical procedures operated by a surgery supervisor.

44.8.2 System optimization

In the case of developing robotic technology for microsurgery, more effort is needed in studying human factors to design more effective human–robot interfaces that are intuitive enough to perform complicated maneuvers inside the eye. Little attention has been paid so far to coordinate the control of multiple instruments at once. In manual interventions, surgeons regularly reposition the eye to optimize the view angle; after obtaining a good view they conduct then ultra-precise manipulations. While this concerns very different gestures, surgeons are used to quickly switching between them. Virtual fixtures that coordinate and constrain the relative motion between instruments, such as proposed by Balicki [248] and more recently by He [242,243], could be further explored to this end. Increased surgical time and cost remain serious concerns for robotic surgery. Several strategies can be followed to limit these concerns, such as for example making sure that robotic surgeons possess equal control over what happens with and within the eye. Another essential feature is the possibility to quickly exchange tools such as developed by Nambi et al. [52]. Further optimization of space would be needed as well. Especially in the case where the surgeon remains close to the patient, space occupancy of the robotic device is crucial as it should not affect the surgeon's already poor ergonomic conditions negatively. Multidisciplinary teams should work together to understand how to build optimal compact and low-cost systems. Clinicians have traditionally worked together with biomedical engineers to design systems for specific applications, but have not been successful in translating these systems to the clinic. Most commonly, academic research occurs in isolation of the constraints that a real OR poses. For example, academic teams have designed robots that are challenging to integrate into existing clinical procedures, therefore limiting their adoption. It is time to pay greater attention to devise streamlined robot design approaches that consider more profoundly the constraints of the OR, staff position, and assistant/surgeon position, together with ergonomics, microscope constraints, and the challenges of the actual application at hand. The robotic retinal surgery community can therefore leverage the extensive work conducted by Padoy et al. on OR reconstruction and tracking [278,279].

44.8.3 Novel therapy delivery methods

Depth perception and control is difficult in retinal surgery in general but is especially problematic for subretinal injections where in the absence of visual feedback a precision in the order of 25 μm is needed to ensure critical layers such as the retinal pigment epithelium are not damaged irreparably [21]. The development of OCT has opened up new perspectives in this context, offering the capacity to image disease on the micrometer level and at early disease states. This spurs the development of novel tools and delivery systems that allow interventions in early stages before major complications arise. As new drugs, new prostheses, and cell and gene therapy are being developed, we expect a growth in the development of new miniature delivery instruments and microinjectors that, for example, under iOCT guidance, deliver these therapeutic substances with extreme precision, targeting specific retinal layers [21,53]. In this context, microrobotics have made their appearance. Being the smallest representative of surgical and interventional devices, they offer tremendous opportunities to push miniaturization to the extreme. Ultimately they could enable interaction with few and even individual cells. Microrobots are one of the newest research areas in surgical robotics. Retinal surgery has been one of the major drivers for this technology. Microrobots have been proposed for intraocular drug delivery and retinal vein cannulation, and their mobility has been evaluated in animal models in vivo. The evaluated microrobots are propelled by electromagnetic fields (see Section 44.5.5). Electromagnetic-based actuation is preferred in small-scale actuation due to the favorable scaling of electromagnetic forces and torques with respect to device volume. Even though the minuscule size of the steerable magnetic devices makes the application of forces challenging currently, it can be expected that as the engineering capacity at the microscale levels matures, microdevices will become valuable tools of future retinal surgical operating rooms, primarily as means to precisely deliver novel therapeutics, and subsequently as mechanisms to enable ever more precise interventions.

44.8.4 Toward autonomous interventions

We expect a progressive adoption of automated features, similar to other fields in robotic surgery [280], which could ultimately lead to full autonomous execution of parts of the surgery. A long-term effort would enable a surgeon to supervise a set of robots that perform routine procedure steps autonomously and only call on his/her expertise during critical patient-specific steps. The surgeon would then guide the robot through the more complex tasks. Reaching this goal will require the analysis of data generated from a large number of interventions. Significant research on the topic, primarily on understanding the surgical phases of cataract surgery, has been conducted by Janin et al. [281], among others. Coupled with realistic retinal simulators, such as those developed by Cotin et al. [282], we expect that robots will be able to undertake certain aspects of surgery, such as port placement and vitrectomy, in the near future. Autonomous docking of the surgical instrument with the trocar has already been realized [283]. Visual servoing frameworks such as the ones developed by Riviere et al. [207] would enable automated cauterization of leaky vessels in diabetic retinopathy, therefore speeding up potentially length interventions. Finally, the upcoming field of surgical data science [284] is expected to play an increasingly important role in robotic retinal surgery.

Acknowledgments

Emmanuel B. Vander Poorten's contribution to this publication was supported by EurEyeCase via the EU Framework Programme for Research and Innovation-Horizon 2020 (No. 645331) and STABLEYES an internal KU Leuven C3-fund (3E160419).

Cameron Riviere's contribution to this publication was supported by the US National Institutes of Health (grant nos. R01EB000526, R01EB024564, and R43EY026304).

Jake J. Abbott's contribution to this publication was supported by the National Eye Institute of the National Institutes of Health under award number R21EY027528.

Christos Bergeles' contribution to this publication was supported by an ERC Starting Grant (714562). Further, this report is independent research funded by the National Institute for Health Research (Invention for Innovation, i4i; II-LB-0716–20002).

M. Ali Nasseris contribution to this publication was supported by Ophthalmology Department of Klinikum rechts der Isar, TUM; State of Bavaria; and Carl Zeiss Meditec AG.

Jin U. Kang's contribution to this publication was supported by an NIH grant R01 EY021540 and Coulter Translational Fund.

Koorosh Faridpooya's contribution was supported by the Foundation Rotterdam Eye Hospital and grants from the Foundation Coolsingel and by EurEyeCase via the EU Framework Programme for Research and Innovation-Horizon 2020 (No. 645331).

Iulian Iordachita's contribution to this publication was supported by US National Institutes of Health (grant numbers 1R01EB023943 and 1R01EB025883).

The views expressed in this publication are those of the authors and not necessarily those of the National Institutes of Health, the NHS, the National Institute for Health Research, or the Department of Health.

References

[1] The Editors of Encyclopaedia Brittanica. 2018. Retina. https://www.britannica.com/science/retina.

[2] Singh KD, Logan NS, Gilmartin B. Three-dimensional modeling of the human eye based on magnetic resonance imaging. Investig Ophthalmol Vis Sci 2006;47(6):2272–9.

[3] Almony A, Nudleman E, Shah GK, Blinder KJ, Eliott DB, Mittra RA, et al. Techniques, rationale, and outcomes of internal limiting membrane peeling. Retina 2012;32(5):877–91.

[4] Charles S, Calzada J. Vitreous microsurgery. Lippincott Williams & Wilkins.; 2010.

[5] Wilkins JR, Puliafito CA, Hee MR, Duker JS, Reichel E, Coker JG, et al. Characterization of epiretinal membranes using optical coherence tomography. Ophthalmology 1996;103(12):2142–51.

[6] Becker BC, Voros S, Lobes Jr LA, Handa JT, Hager GD, Riviere CN. Retinal vessel cannulation with an image-guided handheld robot. In: Proceedings of the annual international conference of the IEEE engineering in medicine and biology society. 2010b. p. 5420–3.

[7] Leng T, Miller JM, Bilbao KV, Palanker DV, Huie P, Blumenkranz MS. The chick chorioallantoic membrane as a model tissue for surgical retinal research and simulation. Retina 2004;24(3):427–34.

[8] Kafieh R, Rabbani H, Hajizadeh F, Abramoff MD, Sonka M, et al. Thickness mapping of eleven retinal layers segmented using the diffusion maps method in normal eyes. J Ophthalmol 2015. 2015.

[9] Jagtap AD, Riviere CN. Applied force during vitreoretinal microsurgery with handheld instruments. Proc Annu Int Conf IEEE Eng Med Biol Soc 2004;4:2771–4.

[10] Gupta PK, Jensen PS, de Juan E. Surgical forces and tactile perception during retinal microsurgery. In: International conference on medical image computing and computer-assisted intervention. Springer; 1999. p. 1218–25.

[11] Gijbels A, Willekens K, Esteveny L, Stalmans P, Reynaerts D, Vander Poorten EB. Towards a clinically applicable robotic assistance system for retinal vein cannulation. In: IEEE international conference on biomedical robotics and biomechatronics. 2016. p. 284–91.

[12] Sun Z, Balicki M, Kang J, Handa J, Taylor R, Iordachita I. Development and preliminary data of novel integrated optical micro-force sensing tools for retinal microsurgery. IEEE Int Conf Robot Autom 2009:1897–902.

[13] Ergeneman O, Pokki J, Počepcová V, Hall H, Abbott JJ, Nelson BJ. Characterization of puncture forces for retinal vein cannulation. J Med Devices 2011;5(4):044504.

[14] Iordachita I, Sun Z, Balicki M, Kang JU, Phee SJ, Handa J, et al. A sub-millimetric, 0.25 mN resolution fully integrated fiber-optic force-sensing tool for retinal microsurgery. Int J Computer Assist Radiology Surg 2009;4(4):383–90.

[15] Sunshine S, Balicki M, He X, Olds K, Kang J, Gehlbach P, et al. A force-sensing microsurgical instrument that detects forces below human tactile sensation. Retina 2013;33:200–6.

[16] Bergeles C, Sugathapala M, Yang G-Z. Retinal surgery with flexible robots: Biomechanical advantages. In: International symposium on medical robotics. 2018. p. 1–6.

[17] Singh K, Dion C, Costantino S, Wajszilber M, Lesk MR, Ozaki T. In vivo measurement of the retinal movements using Fourier domain low coherence interferometry. In: Conference on lasers and electro-optics, page CMR4. Optical Society of America; 2009.

[18] Ourak M, Smits J, Esteveny L, Borghesan G, Gijbels A, Schoevaerdts L, et al. Combined OCT distance and FBG force sensing cannulation needle for retinal vein cannulation: in vivo animal validation. Int J Computer Assist Radiology Surg 2019;14:301–9.

[19] Ang WT, Riviere CN, Khosla PK. An active hand-held instrument for enhanced microsurgical accuracy. In: International conference on medical image computing and computer-assisted intervention. Springer; 2000. p. 878–86.

[20] Charles S, Das H, Ohm T, Boswell C, Rodriguez G, Steele R, et al. Dexterity-enhanced telerobotic microsurgery. In: IEEE international conference on advanced robotics. 1997. p. 5–10.

[21] Zhou M, Huang K, Eslami A, Roodaki H, Zapp D, Maier M, et al. Precision needle tip localization using optical coherence tomography images for subretinal injection. IEEE Int Conf Robot Autom 2018:4033–40.

[22] Riviere CN, Jensen PS. A study of instrument motion in retinal microsurgery. In: Proceedings of the annual international conference of the IEEE engineering in medicine and biology society, vol. 1. 2000. p. 59–60.
[23] Singh SPN, Riviere CN. Physiological tremor amplitude during retinal microsurgery. In: Proceedings of the IEEE northeast bioengineering conference. 2002. p. 171–2.
[24] Peral-Gutierrez F, Liao AL, Riviere CN. Static and dynamic accuracy of vitreoretinal surgeons. In: Proceedings of the annual international conference of the IEEE engineering in medicine and biology society, vol. 1. 2004. p. 2734–7.
[25] Hubschman J, Son J, Allen B, Schwartz S, Bourges J. Evaluation of the motion of surgical instruments during intraocular surgery. Eye 2011;25(7):947.
[26] Balicki M, Uneri A, Iordachita I, Handa J, Gehlbach P, Taylor R. Micro-force sensing in robot assisted membrane peeling for vitreoretinal surgery. In: International conference on medical image computing and computer-assisted intervention. Springer; 2010. p. 303–310.
[27] Charles S. Dexterity enhancement for surgery. Computer integrated surgery: technology and clinical applications, 1996. p. 467–71.
[28] Harwell RC, Ferguson RL. Physiologic tremor and microsurgery. Microsurgery 1983;4(3):187–92.
[29] Patkin M. Ergonomics applied to the practice of microsurgery. Australian N ZealJ Surg 1977;47(3):320–9.
[30] Wells TS, Yang S, MacLachlan RA, Handa JT, Gehlbach P, Riviere C. Comparison of baseline tremor under various microsurgical conditions. In: IEEE international conference on systems, man, and cybernetics. 2013. p. 1482–7.
[31] McCannel CA, Olson EJ, Donaldson MJ, Bakri SJ, Pulido JS, Donna M. Snoring is associated with unexpected patient head movement during monitored anesthesia care vitreoretinal surgery. Retina 2012;32(7):1324–7.
[32] Mehta S, Hubbard III GB. Avoiding neck strain in vitreoretinal surgery: an ergonomic approach to indirect ophthalmoscopy and laser photocoagulation. Retina 2013;33(2):439–41.
[33] Feltgen N, Junker B, Agostini H, Hansen LL. Retinal endovascular lysis in ischemic central retinal vein occlusion: one-year results of a pilot study. Ophthalmology 2007;114(4):716–23.
[34] Koch P. Advanced vitreoretinal surgery. Acta Ophthalmol 2017;95(S259).
[35] Yiu G, Marra KV, Wagley S, Krishnan S, Sandhu H, Kovacs K, et al. Surgical outcomes after epiretinal membrane peeling combined with cataract surgery. Br J Ophthalmol 2013;97(9):1197–201.
[36] Alamdar A, Patel N, Urias M, Ebrahimi A, Gehlbach P, Iordachita I. Force and velocity based puncture detection in robot assisted retinal vein cannulation: In-vivo study. IEEE Trans Biomed Eng 2021;69(3):1123–32.
[37] Gijbels A, Smits J, Schoevaerdts L, Willekens K, Vander Poorten EB, Stalmans P, et al. In-human robot-assisted retinal vein cannulation, a world first. Ann Biomed Eng 2018:1–10.
[38] Faridpooya K, van Romunde SH, Manning SS, van Meurs JC, Naus GJ, Beelen MJ, et al. Randomized controlled trial on robot-assisted vs manual surgery for pucker peeling. Clin Exp Ophthalmol 2022;50(9):1057–64.
[39] Maberley DA, Beelen M, Smit J, Meenink T, Naus G, Wagner C, et al. A comparison of robotic and manual surgery for internal limiting membrane peeling. Graefe's Archive Clin Exp Ophthalmol 2020;258:773–8.
[40] Cehajic-Kapetanovic J, Xue K, Edwards TL, Meenink TC, Beelen MJ, Naus GJ, et al. First-in-human robot-assisted subretinal drug delivery under local anesthesia. Am J Ophthalmol 2022;237:104–13.
[41] Edwards TL, Xue K, Meenink T, Beelen M, Naus G, Simunovic MP, et al. A first-in-man trial assessing robotic surgery inside the human eye to perform a subretinal injection. Investig Ophthalmol Vis Sci 2018;59:5936.
[42] Ladha R, Meenink T, Smit J, de Smet MD. Advantages of robotic assistance over a manual approach in simulated subretinal injections and its relevance for gene therapy. Gene Ther 2023;30:264270.
[43] Mitchell P, Smith W, Chey T, Wang JJ, Chang A. Prevalence and associations of epiretinal membranes: the Blue Mountains Eye Study, Australia. Ophthalmology 1997;104(6):1033–40.
[44] Appiah AP, Hirose T, Kado M. A review of 324 cases of idiopathic premacular gliosis. Am J Ophthalmol 1988;106(5):533–5.
[45] Charles S. Techniques and tools for dissection of epiretinal membranes. Graefe's Archive Clin Exp Ophthalmol 2003;241(5):347–52.
[46] Rogers S, McIntosh R, Cheung N, Lim L, Wang J, Mitchell P, et al. The prevalence of retinal vein occlusion: pooled data from population studies from the United States, Europe, Asia, and Australia. Ophthalmology 2010;117(2):313–9.
[47] McIntosh RL, Rogers SL, Lim L, Cheung N, Wang JJ, Mitchell P, et al. Natural history of central retinal vein occlusion: an evidence- based systematic review. Ophthalmology 2010;117(6):1113–23.
[48] Stout JT, Francis PJ. Surgical approaches to gene and stem cell therapy for retinal disease. Hum Gene Ther 2011;22(5):531–5.
[49] Peng Y, Tang L, Zhou Y. Subretinal injection: A review on the novel route of therapeutic delivery for vitreoretinal diseases. Ophthalmic Res 2017;58(4):217–26.
[50] Gonenc B, Balicki MA, Handa J, Gehlbach P, Riviere CN, Taylor RH, et al. Preliminary evaluation of a micro-force sensing handheld robot for vitreoretinal surgery. In: IEEE/RSJ international conference on intelligent robots and systems. 2012. p. 4125–30.
[51] Gupta A, Gonenc B, Balicki M, Olds K, Handa J, Gehlbach P, et al. Human eye phantom for developing computer and robot-assisted epiretinal membrane peeling. In: Proceedings of the annual international conference of the IEEE engineering in medicine and biology society. 2014. p. 6864–7.
[52] Nambi M, Bernstein PS, Abbott JJ. A compact telemanipulated retinal-surgery system that uses commercially available instruments with a quick-change adapter. J Med Robot Res 2016;1(2):1630001.
[53] Kang J, Cheon G. Demonstration of subretinal injection using common-path swept source OCT guided microinjector. Appl Sci 2018;8(8):1287.
[54] He X, Balicki M, Gehlbach P, Handa J, Taylor R, Iordachita I. A novel dual force sensing instrument with cooperative robotic assistant for vitreoretinal surgery. IEEE Int Conf Robot Autom 2013:213–8.
[55] Kummer MP, Abbott JJ, Dinser S, Nelson BJ. Artificial vitreous humor for in vitro experiments. In: Proceedings of the annual international conference of the IEEE engineering in medicine and biology society. 2007. p. 6406–9.

[56] Wei W, Popplewell C, Chang S, Fine HF, Simaan N. Enabling technology for microvascular stenting in ophthalmic surgery. J Med Devices 2010;4(1):014503.
[57] Bergeles C, Kummer MP, Kratochvil BE, Framme C, Nelson BJ. Steerable intravitreal inserts for drug delivery: in vitro and ex vivo mobility experiments. In: International conference on medical image computing and computer-assisted intervention. Springer; 2011. p. 33–40.
[58] Song C, Park DY, Gehlbach PL, Park SJ, Kang JU. Fiber-optic OCT sensor guided smart micro-forceps for microsurgery. Biomed Opt Express 2013;4(7):1045–50.
[59] Fleming I, Balicki M, Koo J, Iordachita I, Mitchell B, Handa J, et al. Cooperative robot assistant for retinal microsurgery. In: International conference on medical image computing and computer-assisted intervention. Springer; 2008. p. 543–50.
[60] Cheon GW, Huang Y, Cha J, Gehlbach PL, Kang JU. Accurate real-time depth control for CP-SSOCT distal sensor based handheld microsurgery tools. Biomed Opt Express 2015;6(5):1942–53.
[61] Ueta T, Nakano T, Ida Y, Sugita N, Mitsuishi M, Tamaki Y. Comparison of robot-assisted and manual retinal vessel microcannulation in an animal model. Br J Ophthalmol 2011;95(5):731–4.
[62] van Overdam KA, Kilic E, Verdijk RM, Manning S. Intra-ocular diathermy forceps. Acta Ophthalmol 2018;96(4):420–2.
[63] de Smet MD, Meenink TCM, Janssens T, Vanheukelom V, Naus GJL, Beelen MJ, et al. Robotic assisted cannulation of occluded retinal veins. PLoS ONE 2016;11(9):e0162037.
[64] Willekens K, Gijbels A, Schoevaerdts L, Esteveny L, Janssens T, Jonckx B, et al. Robot-assisted retinal vein cannulation in an in vivo porcine retinal vein occlusion model. Acta Ophthalmol 2017;95(3):270–5.
[65] Yang S, Balicki M, Wells TS, MacLachlan RA, Liu X, Kang JU, et al. Improvement of optical coherence tomography using active handheld micromanipulator in vitreoretinal surgery. In: Proceedings of the annual international conference of the IEEE engineering in medicine and biology society. 2013. p. 5674–7.
[66] Allf B, De Juan E. In vivo cannulation of retinal vessels. Graefe's Archive Clin Exp Ophthalmol 1987;225(3):221–5.
[67] Posselli NR, Bernstein PS, Abbott JJ. Eye-mounting goggles to bridge the gap between benchtop experiments and in vivo robotic eye surgery. Sci Rep 2023;13:15503.
[68] Peters T, Cleary K. Image-guided interventions: technology and applications. Springer Science & Business Media; 2008.
[69] Fujimoto JG, Pitris C, Boppart SA, Brezinski ME. Optical coherence tomography: an emerging technology for biomedical imaging and optical biopsy. Neoplasia 2000;2(1–2):9–25. ISSN 1476-5586.
[70] Kang J, Huang Y, Zhang K, Ibrahim Z, Cha J, Andrew Lee W, et al. Real-time three-dimensional Fourier-domain optical coherence tomography video image guided microsurgeries. J Biomed Opt 2012;17(8). 081403–1.
[71] Choma MA, Sarunic MV, Yang C, Izatt JA. Sensitivity advantage of swept source and fourier domain optical coherence tomography. Opt Express 2003;11(18):2183–9.
[72] Nassif N, Cense B, Park BH, Yun SH, Chen TC, Bouma BE, et al. In vivo human retinal imaging by ultrahigh-speed spectral domain optical coherence tomography. Opt Lett 2004;29(5):480–2.
[73] Kang JU, Han J-H, Liu X, Zhang K, Song CG, Gehlbach P. Endoscopic functional fourier domain common-path optical coherence tomography for microsurgery. IEEE J Sel Top Quantum Electron 2010;16(4):781–92.
[74] Sharma U, Fried NM, Kang JU. All-fiber common-path optical coherence to- mography: sensitivity optimization and system analysis. IEEE J Sel Top Quantum Electron 2005;11(4):799–805.
[75] Fercher AF, Hitzenberger CK, Kamp G, El-Zaiat SY. Measurement of intraocular distances by backscattering spectral interferometry. Opt Commun 1995;117(1-2):43–8.
[76] Wojtkowski M, Bajraszewski T, Targowski P, Kowalczyk A. Real-time in vivo imaging by high-speed spectral optical coherence tomography. Opt Lett 2003;28(19):1745–7.
[77] Yun S-H, Tearney GJ, de Boer JF, Iftimia N, Bouma BE. High-speed optical frequency-domain imaging. Opt Express 2003;11(22):2953–63.
[78] Zhang K, Kang JU. Real-time 4D signal processing and visualization using graphics processing unit on a regular nonlinear-k Fourier-domain OCT system. Opt Express 2010;18(11):11772–84.
[79] Drexler W, Fujimoto JG. Optical coherence tomography: technology and applications. Springer Science & Business Media; 2008.
[80] Leitgeb R, Hitzenberger C, Fercher AF. Performance of Fourier domain vs. time domain optical coherence tomography. Opt Express 2003;11(8):889–94.
[81] Liu G, Zhang J, Yu L, Xie T, Chen Z. Real-time polarization-sensitive optical coherence tomography data processing with parallel computing. Appl Opt 2009;48(32):6365–70.
[82] Probst J, Hillmann D, Lankenau EM, Winter C, Oelckers S, Koch P, et al. Optical coherence tomography with online visualization of more than seven rendered volumes per second. J Biomed Opt 2010;15(2):026014.
[83] Huang Y, Liu X, Kang JU. Real-time 3D and 4D Fourier domain Doppler optical coherence tomography based on dual graphics processing units. Biomed Opt Express 2012;3(9):2162–74.
[84] Zhang K, Kang JU. Real-time intraoperative 4D full-range FD-OCT based on the dual graphics processing units architecture for microsurgery guidance. Biomed Opt Express 2011;2(4):764–70.
[85] Sa´nchez Brea L, Andrade De Jesus D, Shirazi MF, Pircher M, van Walsum T, Klein S. Review on retrospective procedures to correct retinal motion artefacts in OCT imaging. Appl Sci 2019;9:2700–28.
[86] LaRocca F, Nankivil D, Farsiu S, Izatt JA. Handheld simultaneous scanning laser ophthalmoscopy and optical coherence tomography system. Biomed Opt Express 2013;4(11):2307–21.
[87] Chen Y, Hong Y-J, Makita S, Yasuno Y. Three-dimensional eye motion correction by lissajous scan optical coherence tomography. Biomed Opt Express 2017;8(3):1783–802.

[88] Kim H-J, Song BJ, Choi Y, Kim B-M. Cross-scanning optical coherence tomography angiography for eye motion correction. J Biophotons 2020;13(9). e202000170.
[89] Zuo R, Irsch K, Kang JU. Higher-order regression three-dimensional motion- compensation method for real-time optical coherence tomography volumetric imaging of the cornea. J Biomed Opt 2022;27.
[90] Machemer R. The development of pars plana vitrectomy: a personal account. Graefe's Archive Clin Exp Ophthalmol 1995;233(8):453–68.
[91] Brod RD. Surgery for diseases of the vitreous and retina. J Lanc Gen Hospital 2009;4(1):4–9.
[92] Kasner D. Vitrectomy: a new approach to management of vitreous. Highlights Ophthalmol 1969;11:304.
[93] Berkelman PJ, Whitcomb LL, Taylor RH, Jensen P. (2000). A miniature instrument tip force sensor for robot/human cooperative microsurgical manipulation with enhanced force feedback. In: International conference on medical image computing and computer-assisted intervention. Springer; 2000. p. 897–906.
[94] Berkelman PJ, Whitcomb LL, Taylor RH, Jensen P. A miniature microsurgical instrument tip force sensor for enhanced force feedback during robot-assisted manipulation. IEEE Trans Robot Autom 2003;19(5):917–21.
[95] Fifanski D, Rivera J, Clogenson M, Baur M, Bertholds A, Llosas P, et al. (2017). VivoForce instrument for retinal microsurgery. In: Surgetica. 2017. p. 155–7.
[96] Liu X, Iordachita I, He X, Taylor R, Kang J. Miniature fiber-optic force sensor based on low-coherence Fabry-Perot interferometry for vitreoretinal microsurgery. Biomed Opt Express 2012;3(5):1062–76.
[97] Gijbels A, Reynaerts D, Stalmans P, Vander Poorten E. Design and manufacturing of a 2-DOF force sensing needle for retinal surgery. In: 4th Joint workshop on computer/robot assisted surgery. 2014a. p. 71–4.
[98] He X, Balicki MA, Kang JU, Gehlbach PL, Handa JT, Taylor RH, et al. Force sensing micro-forceps with integrated fiber Bragg grating for vitreoretinal surgery. In: Optical fibers and sensors for medical diagnostics and treatment applications XII, vol. 8218, page 82180W. International Society for Optics and Photonics; 2012a.
[99] He X, Handa J, Gehlbach P, Taylor R, Iordachita I. A submillimetric 3-DOF force sensing instrument with integrated fiber bragg grating for retinal microsurgery. IEEE Trans Biomed Eng 2014;61(2):522–34.
[100] Kuru I, Gonenc B, Balicki M, Handa J, Gehlbach P, Taylor RH, et al. Force sensing micro-forceps for robot assisted retinal surgery. In: Proceedings of the annual international conference of the IEEE engineering in medicine and biology society. 2012. p. 1401–4.
[101] Smits J, Ourak M, Gijbels A, Esteveny L, Borghesan G, Schoevaerdts L, et al. Development and experimental validation of a combined fbg force and oct distance sensing needle for robot-assisted retinal vein cannulation. IEEE Int Conf Robot Autom 2018:129–34.
[102] He X, Balicki M, Gehlbach P, Handa J, Taylor R, Iordachita I. A multi-function force sensing instrument for variable admittance robot control in retinal microsurgery. IEEE Int Conf Robot Autom 2014:1411–8.
[103] Horise Y, He X, Gehlbach P, Taylor R, Iordachita I. FBG-based sensorized light pipe for robotic intraocular illumination facilitates bimanual retinal microsurgery. In: Proceedings of the annual international conference of the IEEE engineering in medicine and biology society. 2015. p. 13–6.
[104] Balicki M, Han J-H, Iordachita I, Gehlbach P, Handa J, Taylor R, et al. Single fiber optical coherence tomography microsurgical instruments for computer and robot-assisted retinal surgery. In: International conference on medical image computing and computer-assisted intervention. 2009. p. 108–5.
[105] Han J-H, Balicki M, Zhang K, Liu X, Handa J, Taylor R, et al. Commonpath Fourier-domain optical coherence tomography with a fiber optic probe integrated into a surgical needle. In: Conference on lasers and electro-optics, page CMCC2. Optical Society of America; 2009.
[106] Schoevaerdts L, Esteveny L, Borghesan G, Ourak M, Gijbels A, Smits J, et al. Innovative bio-impedance sensor towards puncture detection in eye surgery for retinal vein occlusion treatment. IEEE Int Conf Robot Autom 2018:5343–8.
[107] Ergeneman O, Dogangil G, Kummer MP, Abbott JJ, Nazeeruddin MK, Nelson BJ. A magnetically controlled wireless optical oxygen sensor for intraocular measurements. IEEE Sens J 2008;8(1):29–37.
[108] Xu B, Ko SY. Novel force sensing module for a concentric tube-based vitreoretinal surgical robot. Sens Actuators A 2020;316:112395.
[109] Zhang T, Chen B, Zuo S. A novel 3-DOF force sensing microneedle with integrated fiber bragg grating for microsurgery. IEEE Trans Ind Electron 2022;69(1):940–9.
[110] Zhang H, Yi H, Fan Z, Pang L, Bai M, Wang C, et al. An Fbg-based 3-DOF force sensor with simplified structure for retinal microsurgery. IEEE Sens J 2022;22(15):14911–20.
[111] Gonenc B, Gehlbach P, Handa J, Taylor RH, Iordachita I. Motorized force-sensing micro-forceps with tremor cancelling and controlled micro-vibrations for easier membrane peeling. In: IEEE RAS/EMBS international conference on biomedical robotics and biomechatronics. 2014a. p. 244–51.
[112] Gijbels A, Vander Poorten EB, Stalmans P, Reynaerts D. Development and experimental validation of a force sensing needle for robotically assisted retinal vein cannulations. IEEE Int Conf Robot Autom 2015:2270–6.
[113] Gonenc B, Taylor RH, Iordachita I, Gehlbach P, Handa J. (2014b). Force-sensing microneedle for assisted retinal vein cannulation. In: IEEE sensors conference. 2014b. p. 698–701.
[114] Bourla DH, Hubschman JP, Culjat M, Tsirbas A, Gupta A, Schwartz SD. Feasibility study of intraocular robotic surgery with the da vinci surgical system. Retina 2008;28(1):154–8.
[115] Urias MG, Patel N, Ebrahimi A, Iordachita I, Gehlbach PL. Robotic retinal surgery impacts on scleral forces: in vivo study. Transl Vis Sci Technol 2020;9(10):2.
[116] Tao YK, Ehlers JP, Toth CA, Izatt JA. Intraoperative spectral domain optical coherence tomography for vitreoretinal surgery. Opt Lett 2010;35(20):3315–7.
[117] Krug M, Lankenaou E., WO. Patent Application WO2017167850A1 (pct application non-entry in european phase). OCT system. 2017.
[118] Liu X, Li X, Kim D-H, Ilev I, Kang JU. Fiber-optic Fourier-domain commonpath OCT. Chin Opt Lett 2008;6(12):899–901.

[119] Yang S, Balicki M, MacLachlan RA, Liu X, Kang JU, Taylor RH, et al. Optical coherence tomography scanning with a handheld vitreoretinal micromanipulator. In: Proceedings of the annual international conference of the IEEE engineering in medicine and biology society. 2012. p. 948–51.
[120] Borghesan G, Ourak M, Lankenau E, Hu¨ttmann G, Schulz-Hildebrant H, Willekens K, et al. Single scan OCT-based retina detection for robot-assisted retinal vein cannulation. J Med Robot Res 2018;3(02):1840005.
[121] Vander Poorten E, Esteveny L, Gijbels A, Rosa B, Schoevaerdts L, Willekens K, et al. Use case for European robotics in ophthalmologic micro-surgery. In: Proceedings of the 5th joint workshop on new technologies for computer/robot assisted surgery. 2015. p. 10–12.
[122] Cereda MG, Parrulli S, Douven YGM, Faridpooya K, van Romunde S, Hüttmann G, et al. Clinical evaluation of an instrument-integrated OCT-based distance sensor for robotic vitreoretinal surgery. Ophthalmology Science 2021;1(4):100085.
[123] Saito H, Mitsubayashi K, Togawa T. Detection of needle puncture to blood vessel by using electric conductivity of blood for automatic blood sampling. Sens Actuators A 2006;125(2):446–50.
[124] Schoevaerdts L, Esteveny L, Gijbels A, Smits J, Reynaerts D, Vander Poorten E. Design and evaluation of a new bioelectrical impedance sensor for micro-surgery: application to retinal vein cannulation. Int J Computer Assist Radiol Surg 2019;14(2):311–20.
[125] Schoevaerdts L, Esteveny L, Borghesan G, Ourak M, Reynaerts D, Vander Poorten E. Automatic air bubble detection based on bio-impedance for safe drug delivery in retinal veins. In: Proceedings of the Hamlyn symposium on medical robotics. 2018b. p. 7–8.
[126] Schoevaerdts L, Borghesan G, Ourak M, Reynaerts D, Vander Poorten E. Electrical bio-impedance proximity sensing for vitreo-retinal micro-surgery. IEEE Robot Autom Lett 2019;4(4):4086–93.
[127] Cao K, Pinon R, Schachar I, Jayasundera T, Awtar S. Automatic instrument tracking endo-illuminator for intra-ocular surgeries. J Med Devices 2014;8(3):030932.
[128] He X, Van Geirt V, Gehlbach P, Taylor R, Iordachita I. IRIS: integrated robotic intraocular snake. IEEE Int Conf Robot Autom 2015:1764–9.
[129] Hubschman JP, Bourges JL, Choi W, Mozayan A, Tsirbas A, Kim CJ, et al. The microhand: a new concept of micro-forceps for ocular robotic surgery. Eye 2010;24(2):364.
[130] Ikuta K, Kato T, Nagata S. Optimum designed micro active forceps with built-in fiberscope for retinal microsurgery. In: Medical image computing and computer assisted intervention, LNCS 1496. 1998. p.411–20.
[131] Lin F-Y, Bergeles C, Yang G-Z. Biometry-based concentric tubes robot for vitreoretinal surgery. In: Proceedings of the annual international conference of the IEEE engineering in medicine and biology society. 2015. p. 5280–4.
[132] Rahimy E, Wilson J, Tsao T, Schwartz S, Hubschman J. Robot-assisted intraocular surgery: development of the IRISS and feasibility studies in an animal model. Eye 2013;27(8):972.
[133] Wei W, Goldman R, Simaan N, Fine H, Chang S. Design and theoretical evaluation of micro-surgical manipulators for orbital manipulation and intraocular dexterity. IEEE Int Conf Robot Autom 2007:3389–95.
[134] Ikuta K, Kato T, Nagata S. Micro active forceps with optical fiber scope for intraocular microsurgery. In: The ninth annual international workshop on micro electro mechanical systems, 1996, MEMS'96, Proceedings. An investigation of micro structures, sensors, actuators, machines and systems. IEEE; 1996. p. 456–61.
[135] Jinno M, Iordachita I. Improved integrated robotic intraocular snake: analyses of the kinematics and drive mechanism of the dexterous distal unit. J Med Robot Res 2021;6(1–2):2140001.
[136] Jinno M, Iordachita I. Microgripper using flexible wire hinge for robotic intraocular snake. IEEE Int Conf Robot Autom 2022:6218–24.
[137] Spaide RF. Macular hole repair with minimal vitrectomy. Retina 2002;22(2):183–6.
[138] Zhang T, Ping Z, Zuo S. Miniature continuum manipulator with three degrees-of- freedom force sensing for retinal microsurgery. J Mechanisms Robot 2021;13(4):041002.
[139] Zhang H, Wang C, Bai M, Yi H, Yang J, Zhu Y, et al. A micro-3-degree- of-freedom force sensor for intraocular dexterous surgical robots. Adv Intell Syst 2023:2200413.
[140] Richa R, Linhares R, Comunello E, Von Wangenheim A, Schnitzler J-Y, Wassmer B, et al. Fundus image mosaicking for information augmentation in computer-assisted slit-lamp imaging. IEEE Trans Med Imaging 2014;33(6):1304–12.
[141] Komninos C, Pissas T, Flores B, Bloch E, Vercauteren T, Ourselin S, et al. Intra-operative oct (ioct) image quality enhancement: a super-resolution approach using high quality ioct 3d scans. International workshop on ophthalmic medical image analysis. Springer; 2021. p. 21–31.
[142] Komninos C, Pissas T, Mekki L, Flores B, Bloch E, Vercauteren T, et al. Surgical biomicroscopy-guided intra-operative optical coherence tomography (ioct) image super-resolution. Int J Computer Assist Radiology Surg 2022;17(5):877–83.
[143] Bandara AMRR, Giragama PWGRMPB. A retinal image enhancement technique for blood vessel segmentation algorithm. In: IEEE international conference on industrial and information systems. 2017. p. 1–5.
[144] Goldbaum M. Stare-structured analysis of the retina. 2013. https://cecas.clemson.edu/~ahoover/stare/.
[145] Hoover A, Kouznetsova V, Goldbaum M. Locating blood vessels in retinal images by piecewise threshold probing of a matched filter response. IEEE Trans Med Imaging 2000;19(3):203–10.
[146] Staal J, Abra`moff MD, Niemeijer M, Viergever MA, Van Ginneken B. Ridge- based vessel segmentation in color images of the retina. IEEE Trans Med Imaging 2004;23(4):501–9.
[147] Tan B, Wong A, Bizheva K. Enhancement of morphological and vascular features in oct images using a modified bayesian residual transform. Biomed Opt Express 2018;9(5):2394–406.
[148] Pezzementi Z, Voros S, Hager GD. Articulated object tracking by rendering consistent appearance parts. IEEE Int Conf Robot Autom 2009:3940–7.
[149] Sznitman R, Richa R, Taylor RH, Jedynak B, Hager GD. Unified detection and tracking of instruments during retinal microsurgery. IEEE Trans Pattern Anal Mach Intell 2014;35(5):1263–73.
[150] Burschka D, Corso JJ, Dewan M, Lau W, Li M, Lin H, et al. Navigating inner space: 3-d assistance for minimally invasive surgery. Robot Autonom Syst 2005;52:5–26.

[151] Richa R, Balicki M, Sznitman R, Meisner E, Taylor R, Hager G. Vision-based proximity detection in retinal surgery. IEEE Trans Biomed Eng 2012;59(8):2291–301.
[152] Sznitman R, Ali K, Richa R, Taylor RH, Hager GD, Fual P. Data-driven visual tracking in retinal microsurgery. In: MICCAI. 2012. p. 568–75.
[153] Sznitman R, Becker C, Fua PG. Fast part-based classification for instrument detection in minimally invasive surgery. In: MICCAI. 2014a.
[154] Rieke N, Tan DJ, Alsheakhali M, Tombari F, di San Filippo CA, Belagiannis V, et al. Surgical tool tracking and pose estimation in retinal microsurgery. In: MICCAI. 2015. p. 266–73.
[155] Rieke N, Tan DJ, Tombari F, Vizca´ıno JP, di San Filippo CA, Eslami A, et al. Real-time online adaption for robust instrument tracking and pose estimation. In: MICCAI. 2016. p. 422–30.
[156] Kurmann T, Neila PM, Du X, Fua P, Stoyanov D, Wolf S, et al. Simultaneous recognition and pose estimation of instruments in minimally invasive surgery. In: Medical image computing and computer-assisted intervention. 2017.
[157] Laina I, Rieke N, Rupprecht C, Vizca´ıno JP, Eslami A, Tombari F, et al. Concurrent segmentation and localization for tracking of surgical instruments. Med Image Comput Computer-Assisted Intervention 2017:664–72.
[158] Zhou M, Guo X, Grimm M, Lochner E, Jiang Z, Eslami A, et al. Needle detection and localisation for robot-assisted subretinal injection using deep learning. CAAI Trans Intell Technol 2023.
[159] Rieke N, Tombari F, Navab N. Computer vision and machine learning for surgical instrument tracking: focus: random forest-based microsurgical tool tracking. In: Leo M, Farinella GM, editors. *Computer* vision for assistive healthcare, computer vision and pattern recognition. Academic Press; 2018. p. 105–26.
[160] Weiss J, Rieke N, Nasseri MA, Maier M, Eslami A, Navab N. Fast 5DOF needle tracking in iOCT. Int J Computer Assist Radiology Surg 2018;13(6):787–96.
[161] Becker BC, MacLachlan RA, Lobes LA, Hager GD, Riviere CN. Vision-based control of a handheld surgical micromanipulator with virtual fixtures. IEEE Trans Robot 2013;29(3):674–83.
[162] Sommersperger M, Martin-Gomez A, Mach K, Gehlbach PL, Nasseri MA, Iordachita I, et al. Surgical scene generation and adversarial networks for physics-based ioct synthesis. Biomed Opt Express 2022;13(4):2414–30.
[163] Matinfar S, Nasseri MA, Eck U, Kowalsky M, Roodaki H, Navab N, et al. Surgical soundtracks: automatic acoustic augmentation of surgical procedures. Int J Computer Assist Radiol Surg 2018;13(9):1345–55.
[164] Roodaki H, Navab N, Eslami A, Stapleton C, Navab N. Sonifeye: sonification of visual information using physical modeling sound synthesis. IEEE Trans Vis Computer Graph 2017;23(11):2366–71.
[165] Ben Gayed M, Guerrouad A, Diaz C, Lepers B, Vidal P. An advanced control micromanipulator for surgical applications. Syst Sci 1987;13(1–2):123–34.
[166] Guerrouad A, Vidal P. SMOS: stereotaxical microtelemanipulator for ocular surgery. In: Proceedings of the annual international conference of the IEEE engineering in medicine and biology society. 1989. p. 879–80.
[167] He C-Y, Huang L, Yang Y, Liang Q-F, Li Y-K. Research and realization of a master-slave robotic system for retinal vascular bypass surgery. Chin J Mech Eng 2018;31(1):78.
[168] MacLachlan RA, Becker BC, Cuevas Tabare´s J, Podnar GW, Lobes Jr LA, Riviere CN. Micron: an actively stabilized handheld tool for microsurgery. IEEE Trans Robot 2012;28(1):195–212.
[169] Yang S, MacLachlan RA, Riviere CN. Manipulator design and operation for a six-degree-of-freedom handheld tremor-canceling microsurgical instrument. IEEE/ASME Trans Mechatron 2015;20(2):761–72.
[170] Li Z, Fu P, Wei B-T, Wang J, Li A-L, Li M-J, et al. An automatic drug injection device with spatial micro-force perception guided by an microscopic image for robot-assisted ophthalmic surgery. Front Robot AI 2022;9:913930.
[171] Wei W, Goldman RE, Fine HF, Chang S, Simaan N. Performance evaluation for multi-arm manipulation of hollow suspended organs. IEEE Trans Robot 2009;25(1):147–57.
[172] Bergeles C, Kratochvil BE, Nelson BJ. Visually servoing magnetic intraocular microdevices. IEEE Trans Robot 2012;28(4):798–809.
[173] Kummer MP, Abbott JJ, Kratochvil BE, Borer R, Sengul A, Nelson BJ. OctoMag: an electromagnetic system for 5-dof wireless micromanipulation. IEEE Trans Robot 2010;26(6):1006–17.
[174] Charreyron SL, Boehler Q, Dunun AN, Mesot A, Becker M, Nelson BJ. A magnetically navigated microcannula for subretinal injections. IEEE Trans Biomed Eng 2020;68(1):119–29.
[175] Lussi J, Mattmann M, Sevim S, Grigis F, De Marco C, Chautems C, et al. A submillimeter continuous variable stiffness catheter for compliance control. Adv Sci 2021;8:2101290.
[176] He X, Roppenecker D, Gierlach D, Balicki M, Olds K, Gehlbach P, et al. Toward clinically applicable steady-hand eye robot for vitreoretinal surgery. ASME international mechanical engineering congress and exposition. American Society of Mechanical Engineers.; 2012. p. 145–53.
[177] Üneri A, Balicki MA, Handa J, Gehlbach P, Taylor RH, Iordachita I. (2010). New steady-hand eye robot with micro-force sensing for vitreoretinal surgery. In: IEEE RAS/EMBS international conference on biomedical robotics and biomechatronics. 2010. p. 814–9.
[178] Song J, Gonenc B, Gua J, Iordachita I. Intraocular snake integrated with the steady-hand eye robot for assisted retinal microsurgery. IEEE Int Conf Robot Autom 2017:6724–9.
[179] Mablekos-Alexiou A, Ourselin S, Da Cruz L, Bergeles C. Requirements based design and end-to-end dynamic modeling of a robotic tool for vitreoretinal surgery. IEEE Int Conf Robot Autom 2018:135–41.
[180] Caers P, Gijbels A, De Volder M, Gorissen B, Stalmans P, Reynaerts D, et al. Precision experiments on a comanipulated robotic system for use in retinal surgery. In: Proceedings of the SCATh joint workshop on new technologies for computer/robot assisted surgery. 2011. p. 1–7.
[181] Gijbels A, Wouters N, Stalmans P, Van Brussel H, Reynaerts D, Vander Poorten E. Design and realisation of a novel robotic manipulator for retinal surgery. In: IEEE/RSJ international conference on intelligent robots and systems. 2013. p. 3598–603.

[182] Gijbels A, Vander Poorten EB, Gorissen B, Devreker A, Stalmans P, Reynaerts D. Experimental validation of a robotic comanipulation and telemanipulation system for retinal surgery. In: 5th IEEE RAS/EMBS international conference on biomedical robotics and biomechatronics. IEEE; 2014b. p. 144–50.
[183] Wu Z, Troll J, Jeong H-H, Wei Q, Stang M, Ziemssen F, et al. A swarm of slippery micropropellers penetrates the vitreous body of the eye. Sci Adv 2018;4(11):eaat4388.
[184] Hunter IW, Doukoglou TD, Lafontaine SR, Charette PG, Jones LA, Sagar MA, et al. A teleoperated microsurgical robot and associated virtual environment for eye surgery. Presence 1993;2(4):265–80.
[185] Hunter IW, Lafontaine S, Nielsen PMF, Hunter PJ, Hollerbach JM. Manipulation and dynamic mechanical testing of microscopic objects using a tele-micro-robot system. IEEE Int Conf Robot Autom 1990:3–9.
[186] Schenker PS, Das H, Ohm TR. A new robot for high dexterity microsurgery. Computer vision, virtual reality and robotics in medicine. Springer; 1995. p. 115–22.
[187] Grace KW, Colgate JE, Glucksberg MR, Chun JH. A six degree of freedom micromanipulator for ophthalmic surgery. IEEE Int Conf Robot Autom 1993;1:630–5.
[188] Jensen PS, Grace KW, Attariwala R, Colgate JE, Glucksberg MR. Toward robot-assisted vascular microsurgery in the retina. Graefe's Archive Clin Exp Ophthalmol 1997;235(11):696–701.
[189] Meenink HCM, Hendrix R, Naus GJL, Beelen MJ, Nijmeijer H, Steinbuch M, et al. Robot-assisted vitreoretinal surgery. In: Gomes P, editor. Medical robotics: minimally invasive surgery. Woodhead Publishing; 2012. p. 185–209.
[190] Meenink T, Naus G, de Smet M, Beelen M, Steinbuch M. Robot assistance for micrometer precision in vitreoretinal surgery. Investig Ophthalmol Vis Sci 2013;54(15):5808.
[191] Nasseri MA, Eder M, Eberts D, Nair S, Maier M, Zapp D, et al. Kinematics and dynamics analysis of a hybrid parallel-serial micromanipulator designed for biomedical applications. In: IEEE/ASME international conference on advanced intelligent mechatronics. 2013a. p. 293–9.
[192] Nasseri MA, Eder M, Nair S, Dean E, Maier M, Zapp D, et al. The introduction of a new robot for assistance in ophthalmic surgery. In: Proceedings of the annual international conference of the IEEE engineering in medicine and biology society. 2013b. p. 5682–5.
[193] Wilson JT, Gerber MJ, Prince SW, Chen C-W, Schwartz SD, Hubschman J-P, et al. Intraocular robotic interventional surgical system (IRISS): mechanical design, evaluation, and masterslave manipulation. Int J Med Robot Computer Assist Surg 2018;4:e1842.
[194] Ida Y, Sugita N, Ueta T, Tamaki Y, Tanimoto K, Mitsuishi M. Microsurgical robotic system for vitreoretinal surgery. Int J Computer Assist Radiology Surg 2012;7(1):27–34.
[195] Ueta T, Yamaguchi Y, Shirakawa Y, Nakano T, Ideta R, Noda Y, et al. Robot-assisted vitreoretinal surgery: development of a prototype and feasibility studies in an animal model. Ophthalmology 2009;116(8):1538–43.
[196] Nakano T, Sugita N, Ueta T, Tamaki Y, Mitsuishi M. A parallel robot to assist vitreoretinal surgery. Int J Computer Assist Radiol Surg 2009;4(6):517.
[197] Posselli NR, Bernstein PS, Abbott JJ. Head-mounting surgical robots for passive motion compensation. In: Hamlyn symposium of medical robotics. 2022. p. 95–96.
[198] Mahoney AW, Nelson ND, Parsons EM, Abbott JJ. Non-ideal behaviors of magnetically driven screws in soft tissue. In: IEEE/RSJ international conference on robotics and intelligent systems. 2012. p. 3559–64.
[199] Nelson ND, Delacenserie J, Abbott JJ. An empirical study of the role of magnetic, geometric, and tissue properties on the turning radius of magnetically driven screws. IEEE Int Conf Robot Autom 2013:5352–7.
[200] Yu D-Y, Cringle SJ, Constable IJ. Robotic ocular ultramicrosurgery. Austr N ZealJ Ophthalmol 1998;26(Suppl):S6–8.
[201] Ahronovich EZ, Shihora N, Shen J-H, Joos K, Simaan N. Exploring an external approach to subretinal drug delivery via robot assistance and B-mode OCT. IEEE Int Conf Robot Autom 2023:6795–801.
[202] Yang S, Lobes Jr LA, Martel JN, Riviere CN. Handheld-automated microsurgical instrumentation for intraocular laser surgery. Lasers Surg Med 2015;47(8):658–68.
[203] Smits J, Reynaerts D, Vander Poorten E. Synthesis and methodology for optimal design of a parallel remote center of motion mechanism: application to robotic eye surgery. Mechanisms Mach Theory 2020;151:103896.
[204] Suzuki H, Wood RJ. Origami-inspired miniature manipulator for teleoperated micro-surgery. Nat Mach Intell 2020;2:437–46.
[205] Han Y, Routray A, Adeghate JO, MacLachlan RA, Martel JN, Riviere CN. Monocular vision-based retinal membrane peeling with a handheld robot. J Med Devices 2021;15(3).
[206] Riviere CN, Ang WT, Khosla PK. Toward active tremor canceling in handheld microsurgical instruments. IEEE Trans Robot Autom 2003;19(5):793–800.
[207] Yang S, Martel JN, Lobes Jr LA, Riviere CN. Techniques for robot-aided intraocular surgery using monocular vision. Int J Robot Res 2018;37(8):931–52.
[208] MacLachlan RA, Riviere CN. High-speed microscale optical tracking using digital frequency-domain multiplexing. IEEE Trans Instrum Meas 2009;58(6):1991–2001.
[209] MacLachlan RA, Hollis RL, Jaramaz B, Martel JN, Urish KL, Riviere CN. Multirate Kalman filter rejects impulse noise in frequency-domain-multiplexed tracker measurements. In: IEEE sensors conference. 2017. p. 591–3.
[210] MacLachlan RA, Parody N, Mukherjee S, Hollis RL, Riviere CN. Electromagnetic tracker for active handheld robotic systems. In: IEEE sensors conference. 2016. p. 52–54.
[211] Roth R, Wu J, Alamdar A, Taylor RH, Gehlbach P, Iordachita I. (2021). Towards a clinically optimized tilt mechanism for bilateral micromanipulation with steady-hand eye robot. In: International symposium on medical robotics. 2021. p. 1–7.

[212] Wu J, Li G, Urias M, Patel NA, Liu Y-H, Gehlback P, et al. An optimized tilt mechanism for a new steady-hand eye robot. In: IEEE/RSJ international conference on intelligent robots and systems. 2020b. p. 3105–11.
[213] Xiao B, Alamdar A, Song K, Ebrahimi A, Gehlbach P, Taylor RH, et al. Delta robot kinematic calibration for precise robot-assisted retinal surgery. In: International symposium on medical robotics. 2022. p. 1–7.
[214] Yu H, Shen J-H, Joos KM, Simaan N. Calibration and integration of B-mode optical coherence tomography for assistive control in robotic microsurgery. IEEE/ASME Trans Mechatron 2016;21(6):2613–23.
[215] Jinno M, Li G, Patel N, Iordachita I. An integrated high-dexterity cooperative robotic assistant for intraocular micromanipulation. IEEE Int Conf Robot Autom 2021:1198–204.
[216] Bergeles C, Shamaei K, Abbott JJ, Nelson BJ. Single-camera focus-based localizing of intraocular devices. IEEE Trans Biomed Eng 2010;57(8):2064–74.
[217] Ergeneman O, Bergeles C, Kummer MP, Abbott JJ, Nelson BJ. Wireless intraocular microrobots: opportunities and challenges. In: Rosen J, Hannaford B, Satava RM, editors. Surgical robotics: systems applications and visions. Springer; 2011. p. 271–311.
[218] Edwards TL, Xue K, Meenink HCM, Beelen MJ, Naus GJL, Simunovic MP, et al. First-in-human study of the safety and viability of intraocular robotic surgery. Nat Biomed Eng 2018;2:649–56.
[219] Willekens K, Gijbels A, Smits J, Schoevaerdts L, Blanckaert J, Feyen JH, et al. Phase I trial on robot assisted retinal vein cannulation with ocriplasmin infusion for central retinal vein occlusion. Acta Ophthalmol 2021;99(1):90–6.
[220] Elhousseini Z, Lee E, Williamson TH. Incidence of lens touch during pars plana vitrectomy and outcomes from subsequent cataract surgery. Retina 2016;36(4):825–9.
[221] Jacobsen MF, Konge L, Cour M, So¨rensen RB, Park YS, Thomsen ASS. The learning curve of robot-assisted vitreoretinal surgery—a randomized trial in a simulated setting. Acta Ophthalmol 2021;99(8):e1509–16.
[222] Nambi M, Bernstein PS, Abbott JJ. Effect of haptic-interface virtual kinematics on the performance and preference of novice users in telemanipulated retinal surgery. IEEE Robot Autom Lett 2017;2(1):64–71.
[223] Huang K, Zhou M, Lajblich C, Lohmann CP, Knoll A, Ling Y, et al. A flexible head fixation for ophthalmic microsurgery. In: Chinese automation congress. 2017. p. 6707–10.
[224] Nasseri MA, Maier M, Lohmann CP. A targeted drug delivery platform for assisting retinal surgeons for treating age-related macular degeneration (AMD). In: Proc. int. conf. IEEE eng. med. biol. soc. 2017. p. 4333–8.
[225] Natalius H, Lambert P, Tiwari MK, da Cruz L, Bergeles C. Design, static and performance analysis of a parallel robot for head stabilisation in vitreoretinal surgery. Rauter G, Cattin PC, Zam A, Riener R, Carbone G, Pisla D, editors. New trends in medical and service robotics. MESROB 2020. Mechanisms and machine science, vol. 93. Cham: Springer; 2021. p. 169–79.
[226] Birch J, Da Cruz L, Rhode K, Bergeles C. Unsupervised out-of-distribution detection for safer robotically guided retinal microsurgery. Int J Computer Assist Radiology Surg 2023.
[227] Ebrahimi A, Roizenblatt M, Patel N, Gehlbach P, Iordachita I. Auditory feedback effectiveness for enabling safe sclera force in robot-assisted vitreoretinal surgery: a multi-user study. In: IEEE/RSJ international conference on intelligent robots and systems. 2020. p. 32743280.
[228] Ebrahimi A, Urias MG, Patel N, Taylor RH, Gehlbach P, Iordachita I. Adaptive control improves sclera force safety in robot-assisted eye surgery: a clinical study. IEEE Trans Biomed Eng 2021;68(11):3356–65.
[229] He C, Patel N, Shahbazi M, Yang Y, Gehlbach P, Kobilarov M, et al. Toward safe retinal microsurgery: development and evaluation of an RNN-based active interventional control framework. IEEE Trans Biomed Eng 2020;67(4):966–77.
[230] Jungo A, Doorenbos L, Da Col T, Beelen M, Zinkernagel M, Ma´rquez-Neila P, et al. Unsupervised out-of-distribution detection for safer robotically guided retinal microsurgery. Int J Computer Assist Radiology Surg 2023;18:1085–91.
[231] Wu J, He C, Ebrahimi A, Urias M, Patel NA, Liu Y-H, et al. Force-based safe vein cannulation in robot-assisted retinal surgery: a preliminary study. In: International symposium on medical robotics. 2020a. p. 8–14.
[232] Brosilow C, Joseph B. Techniques of model-based control. Prentice-Hall; 2002.
[233] Becker BC, MacLachlan RA, Riviere CN. State estimation and feedforward tremor suppression for a handheld micromanipulator with a Kalman filter. In: IEEE/RSJ international conference on intelligent robots and systems. 2011. p. 5160–5.
[234] Riviere CN, Rader RS, Thakor NV. Adaptive canceling of physiological tremor for improved precision in microsurgery. IEEE Trans Biomed Eng 1998;45(7):839–46.
[235] Mukherjee S, MacLachlan R, Riviere CN. Velocity-limiting control of an active handheld micromanipulator. J Med Devices 2016;10(3):030944-1–2.
[236] Wells TS, Yang S, MacLachlan RA, Lobes Jr. LA, Martel JN, Riviere CN. Hybrid position/force control of an active handheld micromanipulator for membrane peeling. Int J Med Robot Computer Assist Surg 2016;12(1):85–95.
[237] Rosenberg LB. Virtual fixtures: perceptual tools for telerobotic manipulation. In: IEEE virtual reality annual international symposium. 1993. p. 76–82.
[238] Cutler N, Balicki M, Finkelstein M, Wang J, Gehlbach P, McGready J, et al. Auditory force feedback substitution improves surgical precision during simulated ophthalmic surgery. Investig Ophthalmol Vis Sci 2013;54(2):1316–24.
[239] Kumar R, Berkelman P, Gupta P, Barnes A, Jensen PS, Whitcomb LL, et al. Preliminary experiments in cooperative human/robot force control for robot assisted microsurgical manipulation. IEEE Int Conf Robot Autom 2000;1:610–7.
[240] Ebrahimi A, He C, Roizenblatt M, Patel N, Sefati S, Gehlbach P, et al. Real-time sclera force feedback for enabling safe robot-assisted vitreoretinal surgery. In: 2018 40th Annual international conference of the IEEE engineering in medicine and biology society (EMBC). IEEE; 2018. p. 3650–5.
[241] Ebrahimi A, Patel N, He C, Gehlbach P, Kobilarov M, Iordachita I. Adaptive control of sclera force and insertion depth for safe robot-assisted retinal surgery. In: 2019 international conference on robotics and automation (ICRA). IEEE; 2019. p. 9073–9.
[242] He C, Ebrahimi A, Yang E, Urias M, Yang Y, Gehlbach P, et al. Towards bimanual vein cannulation: preliminary study of a bimanual robotic system with a dual force constraint controller. In: 2020 IEEE international conference on robotics and automation (ICRA). IEEE; 2020a. p. 4441–7.

[243] He C, Yang E, Patel N, Ebrahimi A, Shahbazi M, Gehlbach P, et al. Automatic light pipe actuating system for bimanual robot-assisted retinal surgery. IEEE/ASME Trans Mechatron 2020;25(6):2846–57.
[244] Jingjing X, Long H, Lijun S, Yang Y. Design and research of a robotic aided system for retinal vascular bypass surgery. J Med Devices 2014;8(4):044501.
[245] Hashtrudi-Zaad K, Salcudean SE. Analysis of control architectures for teleoperation systems with impedance/admittance master and slave manipulators. Int J Robot Res 2001;20(6):419–45.
[246] Lawrence DA.Designing teleoperator architectures for transparency. In: Proceedings, 1992 IEEE international conference on robotics and automation. IEEE; 1992. p. 1406–11.
[247] Balicki M, Xia T, Jung MY, Deguet A, Vagvolgyi B, Kazanzides P, et al. Prototyping a hybrid cooperative and tele-robotic surgical system for retinal microsurgery. MIDAS J 2011;2011:815.
[248] Balicki MA. Augmentation of human skill in microsurgery. PhD thesis, The Johns Hopkins University; 2014.
[249] Griffin JA, Zhu W, Nam CS. The role of haptic feedback in robotic-assisted retinal microsurgery systems: a systematic review. IEEE Trans Haptics 2017;10(1):94–105.
[250] Dewan M, Marayong P, Okamura AM, Hager GD. Vision-based assistance for ophthalmic micro-surgery. In: International conference on medical image computing and computer- assisted intervention. Springer; 2004. p. 49–57.
[251] Becker BC, MacLachlan RA, Lobes Jr LA, Riviere CN. Semiautomated intraocular laser surgery using handheld instruments. Lasers Surg Med 2010;42(3):264–73.
[252] Castan˜o A, Hutchinson S. Visual compliance: task-directed visual servo control. IEEE Trans Robot Autom 1994;10(3):334–42.
[253] Yang S, MacLachlan RA, Martel JN, Lobes LA, Riviere CN. Comparative evaluation of handheld robot-aided intraocular laser surgery. IEEE Trans Robot 2016;32(1):246–51.
[254] Probst T, Maninis K-K, Chhatkuli A, Ourak M, Vander Poorten E, Van Gool L. Automatic tool landmark detection for stereo vision in robot-assisted retinal surgery. IEEE Robot Autom Lett 2018;3(1):612–9.
[255] Zhou M, Wu J, Ebrahimi A, Patel N, Liu Y, Navab N, et al. Spotlight-based 3D instrument guidance for autonomous task in robot- assisted retinal surgery. IEEE Robototics Autom Lett 2021;6(4):7750–7.
[256] Mukherjee S, Yang S, MacLachlan RA, Lobes LA, Martel JN, Riviere CN. Toward monocular camera-guided retinal vein cannulation with an actively stabilized handheld robot. IEEE Int Conf Robot Autom 2017:2951–6.
[257] Routray A, MacLachlan R, Martel J, Riviere C. Real-time incremental estimation of retinal surface using laser aiming beam. In: 2019 International symposium on medical robotics (ISMR). 2019. p. 1–5.
[258] Braun D, Yang S, Martel JN, Riviere CN, Becker BC. EyeSLAM: real-time simultaneous localization and mapping of retinal vessels during intraocular microsurgery. Int J Med Robot Computer Assist Surg 2018;14(1):e1848.
[259] Can A, Shen H, Turner JN, Tanenbaum HL, Roysam B. Rapid automated tracing and feature extraction from retinal fundus images using direct exploratory algorithms. IEEE Trans Inf Technol Biomed 1999;3(2):125–38.
[260] Mukherjee S, Kaess M, Martel JN, Riviere CN. EyeSAM: graph-based localization and mapping of retinal vasculature during intraocular microsurgery. Int J Computer Assist Radiol Surg 2019;14:819828.
[261] Kim JW, He C, Urias M, Gehlbach P, Hager GD, Iordachita I, et al. Autonomously navigating a surgical tool inside the eye by learning from demonstration. IEEE Int Conf Robot Autom 2020:7351–7.
[262] Koyama Y, Marinho MM, Mitsuishi M, Harada K. Autonomous coordinated control of the light guide for positioning in vitreoretinal surgery. IEEE Trans Med Robot Bionics 2022;4(1):156–71.
[263] Koyama Y, Marinho MM, Harada K. Vitreoretinal surgical robotic system with autonomous orbital manipulation using vector-field inequalities. In: 2023 IEEE international conference on robotics and automation (ICRA). IEEE; 2023. p. 4654–60.
[264] Ajlan RS, Desai AA, Mainster MA. Endoscopic vitreoretinal surgery: principles, applications and new directions. Int J Retina Vitreous 2019;5:15.
[265] Zhou D, Takeyama H, Nakao S, Sonoda K-H, Tadano K. Realtime fundus reconstruction and intraocular mapping using an ophthalmic endoscope. Int J Med Robot Computer Assist Surg 2023;19:e2496.
[266] Carrasco-Zevallos OM, Viehland C, Keller B, Draelos M, Kuo AN, Toth CA, et al. Review of intraoperative optical coherence tomography: technology and applications. Biomed Opt Express 2017;8(3):1607–37.
[267] Zhou M, Roodaki H, Eslami A, Chen G, Huang K, Maier M, et al. Needle segmentation in volumetric optical coherence tomography images for ophthalmic microsurgery. Appl Sci 2017;7(8):748.
[268] Zhou M, Hamad M, Weiss J, Eslami A, Huang K, Maier M, et al. Towards robotic eye surgery: marker-free, online hand-eye calibration using optical coherence tomography images. IEEE Robot Autom Lett 2018;3(4):3944–51.
[269] Gerber MJ, Hubschman J-P, Tsao T-C. Automated retinal vein cannulation on silicone phantoms using optical-coherence-tomography-guided robotic manipulations. IEEE/ASME Trans Mechatron 2021;26(5):2758–69.
[270] Giudice GD, Orekhov AL, Shen J-H, Joos KM, Simaan N. Investigation of micromotion kinematics of continuum robots for volumetric OCT and OCT-guided visual servoing. IEEE/ASME Trans Mechatron 2021;26(5):2604–15.
[271] Cornelissen P, Ourak M, Borghesan G, Reynaerts D, Vander Poorten E. Towards real-time estimation of a spherical eye model based on a single fiber OCT. In: International conference on advanced robotics. 2019. p. 666–72.
[272] Song C, Gehlbach PL, Kang JU. Active tremor cancellation by a smart handheld vitreoretinal microsurgical tool using swept source optical coherence tomography. Opt Express 2012;20(21):23414–21.
[273] Cheon GW, Gonenc B, Taylor RH, Gehlbach PL, Kang JU. Motorized microforceps with active motion guidance based on common-path ssoct for epiretinal membranectomy. IEEE/ASME Trans Mechatron 2017;22(6):2440–8.

[274] Liu X, Huang Y, Kang JU. Distortion-free freehand-scanning OCT implemented with real-time scanning speed variance correction. Opt Express 2012;20(15):16567–83.

[275] de Smet MD, Naus GJL, Faridpooya K, Mura M. Robotic-assisted surgery in ophthalmology. Curr OpOphthalmol 2018;29(3):248–53.

[276] Turgut F, Somfai GM, Heussen FM, Eberle A, de Smet MD, Becker MD. Robot-assisted epiretinal membrane peeling: a prospective assessment of pre-and intra-operative times and of surgeons subjective perceptions. J Clin Med 2023;12(8):2768.

[277] He B, de Smet MD, Sodhi M, Etminan M, Maberley D. A review of robotic surgical training: establishing a curriculum and credentialing process in ophthalmology. Eye 2021;35(12):3192–201.

[278] Padoy N, Blum T, Feussner H, Berger M-O, Navab N. On-line recognition of surgical activity for monitoring in the operating room. AAAI 2008:1718–24.

[279] Twinanda AP, Alkan EO, Gangi A, de Mathelin M, Padoy N. Data-driven spatio-temporal rgbd feature encoding for action recognition in operating rooms. Int J Computer Assist Radiol Surg 2015;10(6):737–47.

[280] Kassahun Y, Yu B, Tibebu AT, Stoyanov D, Giannarou S, Metzen JH, et al. Surgical robotics beyond enhanced dexterity instrumentation: a survey of machine learning techniques and their role in intelligent and autonomous surgical actions. Int J Computer Assist Radiol Surg 2016;11(4):553–68.

[281] Lalys F, Riffaud L, Bouget D, Jannin P. A framework for the recognition of high- level surgical tasks from video images for cataract surgeries. IEEE Trans Biomed Eng 2012;59(4):966–76.

[282] Cotin S, Keppi JJ, Allard J, Bessard R, Courtecuisse H, Gaucher D. Project RESET. REtinal Surgery systEm for Training. Acta Ophthalmol 2015;93(S255). ABS15-0477.

[283] Dehghani S, Sommersperger M, Yang J, Salehi M, Busam B, Huang K, et al. ColibriDoc: an eye-in-hand autonomous trocar docking system. IEEE Int Conf Robot Autom 2022:7717–23.

[284] Maier-Hein L, Vedula SS, Speidel S, Navab N, Kikinis R, Park A, et al. Surgical data science for next-generation interventions. Nat Biomed Eng 2017;1(9):691–6.

[285] Can A, Stewart CV, Roysam B, Tanenbaum HL. A feature-based technique for joint, linear estimation of high-order image-to-mosaic transformations: application to mosaicing the curved human retina. In: Proceedings of the IEEE conference on computer vision and pattern recognition, vol. 2. 2000. p. 585–91.